Optical properties of transition metal dichalcogenide monolayers, heterostructures and alloys

By:

Oleksandr Skrypka

A thesis submitted in partial fulfilment of the requirements for the degree of

Doctor of Philosophy

The University of Sheffield
Faculty of Science
Department of Physics and Astronomy

September 2018

To my family, relatives, friends and my country — Ukraine. . .

Acknowledgements

First of all, I would like to acknowledge my supervisor Prof. Alexander Tartakovskii for his advice and support during my first arrival in Sheffield and especially during the PhD study.

Thank Dr. Evgeny Alexeev and Dr. Tillmann Godde for their help and guidance in the laboratory and processing of the results.

An enormous thanks to my colleagues from the LDSD group, Alessandro Catanzaro and again Dr. Evgeny Alexeev, and also to Dr. Lee Hague and Dr. Freddie Withers who worked in the group of Prof. Konstantin Novoselov (the University of Manchester) for the sample production.

Additionally, I want to thank former colleagues from the 2D Materials subgroup, specifically Dr. Osvaldo Del Pozo-Zamudio, Dr. Stefan Schwarz, Robert Schofield, for giving me additional knowledge and experimental skills.

I am thankful to the staff responsible for cryogenics, Chris Vickers and Phil Mydewer, for their excellent technical support; Laura Oliver for the guidance with documents; Sally Greenhough for organizing events and providing links with other world leading research groups and companies.

Many thanks to the University of Sheffield, ITN Spin-NANO and EPSRC for the financial support.

Thank all my friends and housemates in Sheffield.

Finally, special thanks go to my mother, father, sister and her family as well as relatives and best friends in Ukraine. Without you, I would not achieve what I have now.

Abstract

Recent progress in the fabrication of two-dimensional (2D) materials attracts our attention to the study of such structures. Most of them are typically van-der-Waals-like with weak interlayer and strong intralayer bonding. Nowadays, single-layer semiconducting transition metal dichalcogenides (TMDCs), namely molybdenum and tungsten selenides and sulphides, have the biggest interest in optoelectonics due to the remarkable optical properties: the giant spin-orbit coupling, the inversion symmetry breaking, the large exciton binding energy and large oscillator strength. This thesis discusses the investigations in the samples based on the above compounds using photoluminescence (PL), photoluminescence excitation (PLE) and reflectance contrast (RC) spectroscopies. We observe prominent changes in the PL spectral parameters, such as integrated intensities, linewidths, energy positions of peaks and distances between peak maxima, with the alloy composition in the mono-, bi- and trilayer $Mo_xW_{1-x}S_2$ crystals at room temperature. The bowing parameters from parabolic dependences of the band-edge PL and RC on the Mo concentration are extracted. The modifications of the PL and RC spectral peaks with the number of layers and the indirect-to-direct band-gap crossover are also first demonstrated in those materials. Analysing gate-voltage- and temperature-dependent PL spectra, we make evaluations of exciton-electron and exciton-phonon interactions in the single-layer $MoSe_2$. Additionally, the influence of localization and recharging processes is established. In the $MoSe_2/WSe_2$ heterostructures (HSs), the behaviour of localized interlayer excitonic (IX) complexes is investigated by means of different experimental techniques, specifically polarization-resolved, power-, gate-voltage-, temperature-dependent PL and PLE. The impact of the HfO_2/hBN encapsulation on the structure and polarization of the IX emission is studied for the first time. Finally, the specific

band alignment of the $MoSe_2/WS_2$ HS appears to cause the extraordinary PL signal emitted from the states which are likely originated from the interlayer electron hybridization.

List of publications

1. T. Godde, D. Schmidt, J. Schmutzler, M. Aßmann, J. Debus, F. Withers, E. M. Alexeev, O. Del Pozo-Zamudio, **O. V. Skrypka**, K. S. Novoselov, M. Bayer, A. I. Tartakovskii. Exciton and trion dynamics in atomically thin $MoSe_2$ and WSe_2: effect of localization. *Phys. Rev. B* **94 (16)**, 165301 (2016).
2. E. M. Alexeev, A. Catanzaro, **O. V. Skrypka**, P. K. Nayak, S. Ahn, S. Pak, J. Lee, J. I. Sohn, K. S. Novoselov, H. S. Shin, A. I. Tartakovskii. Imaging of interlayer coupling in van der Waals heterostructures using a bright-field optical microscope. *Nano Lett.* **17 (9)**, 5342–5349 (2017).
3. A. Catanzaro, **O. V. Skrypka**, E. M. Alexeev, R. C. Schofield, V. Zólyomi, V. I. Fal'ko, A. I. Tartakovskii. Optical properties of mono-, bi- and trilayer $Mo_xW_{1-x}S_2$ alloys. *Nano Lett.* (under preparation).

Contents

3 Photoluminescence and optical reflectance contrast measurements of $Mo_xW_{1-x}S_2$ transition metal dichalcogenide alloys 53

4 Optical investigation of temperature- and gate-voltage-dependent excitonic effects in monolayer $MoSe_2$ 83

Chapter 1

Background and motivation

1.1 Introduction. Two-dimensional materials

Two-dimensional (2D) materials have been intensively studied in the last 15 years [1], especially those made from the layered materials with a strong intralayer bonding and weak interlayer van der Waals forces. The interest in this topic increased after the first fabrication of a single atomic layer of graphite, called graphene, on a SiO_2/Si substrate using mechanical exfoliation in 2004 [2]. The discovered technique of the monolayer production and transfer on the target substrate had been necessary for a long time, as the physical properties of graphene were already theoretically described in 1947 [3]. This opportunity to produce the ultrathin 2D films without epitaxy, which is the growth of a single crystal film on top of a crystalline substrate, rapidly became popular after its first realization [4]. Reducing the layer thickness significantly changes the properties of the materials. As observed in the case of graphene, its electronic band structure is characterized by Dirac cones with zero bandgap [5]. The electron transport in graphene is ballistic with high charge carrier mobility of up to 2×10^5 $\mathrm{cm^2{\cdot}V^{-1}{\cdot}s^{-1}}$ (for comparison, it is $\sim 10^3$ $\mathrm{cm^2{\cdot}V^{-1}{\cdot}s^{-1}}$ in traditional electronic devices [6]) opening new possibilities for future electronic applications [7]. The quantum Hall effect has been demonstrated in such 2D crystals even at room temperature, extending the experimental temperature range for this phenomenon

Table 1.1 The classification of the most famous 2D materials. Nowadays, there are three big groups, namely graphene-like, chalcogenides and oxides, constituents of which can be produced with atomic-scale thicknesses. Taken and altered from [9].

Graphene family	*2D chalcogenides*		*2D oxides*	
graphene	transition metal dichalcogenides: MoS_2, WS_2, $MoSe_2$, WSe_2		micas, BSCCO	layered Cu oxides
hBN (‘white graphene’)	semiconducting dichalcogenides: $MoTe_2$, WTe_2, ZrS_2, $ZrSe_2$, ...		transition metal oxides: MoO_3, WO_3	TiO_2, MnO_2, V_2O_5, TaO_3, RuO_2, ...
BCN	metallic dichalcogenides: $NbSe_2$, NbS_2, TaS_2, TiS_2, $NiSe_2$, ...	layered semiconductors: GaS, GaSe, GaTe, InSe, Bi_2Se_3, Bi_2Te_3, ...	perovskite-type: $LaNb_2O_7$, $(Ca,Sr)_2Nb_3O_{10}$, $Bi_4Ti_3O_{12}$, $Ca_2Ta_2TiO_{10}$, ...	
fluorographene				
graphene oxide			hydroxides: $Ni(OH)_2$, $Eu(OH)_2$, ...	
Others: phosphorene, some borides, carbides, nitrides, ...				

by a factor of 10 [8]. Thousands of papers on graphene-related topics are published every year and currently the majority of them are about practical use of this material in electronics and optoelectronics [9].

In addition to the unique properties of the monolayers, the simplicity of the fabrication method has led to the rapid growth of this field [10]. Due to the layered structure of graphite, the single-layer graphene flakes are isolated by means of their adhesion to the sticky Scotch tape. The monolayer crystals are then transferred on arbitrary substrates. More detailed information about this fabrication procedure is given in subsection 2.1.1.

Apart from graphene, various van der Waals materials possess the ability to be thinned down to single atomic layers with a similar technique. Three main classes, such as the graphene family, chalcogenides and oxides, can be particularly highlighted [9]. Some of the materials in these classes are listed in Table 1.1.

Hexagonal boron nitride (hBN) is one of the leaders in the use [11–13] and characterized by the high quality and stability [14]. In combination with a wide bandgap of around 6 eV, hBN serves as an exceptional substrate for other 2D films [14], a defect free tunnelling barrier [15, 16], a gate dielectric [17, 18] and a protective cover [19–21].

Some 2D crystals in Table 1.1 (for instance, metallic dichalcogenides and layered semiconductors GaS, GaSe, InSe and so on [9]) are found to be relatively unstable under ambient conditions including contact with air at room temperature. As a solution, the samples containing those materials are fabricated in an oxygen- and water-free atmosphere and encapsulated for the protection from the damage in the air environment [20, 21].

Semiconducting transition metal dichalcogenides (TMDCs), such as MoS_2, WS_2, $MoSe_2$, WSe_2, etc., form a subgroup of 2D materials with attractive optical properties. They have an optical bandgap in the visible and near-infrared light range. Bulk TMDCs have been known as lubricants and have not attracted interest for optoelectronics for many years [22]. However, the situation has changed with the advent of the mechanical exfoliation method. When the layer thickness in an important family of the semiconducting TMDCs is decreased down to a monolayer, an indirect-to-direct bandgap transition is revealed [23]. These structural modifications dramatically increase the quantum efficiency of the single-layer sheets by several orders of magnitude relative to that of the few-layer or bulk crystals [24–27]. A multitude of interesting optical phenomena and features are observed in the 2D TMDCs, which are reviewed in the next sections and chapters of this thesis.

Having a similar crystal structure to TMDCs, other layered semiconductors, specifically indium and gallium chalcogenides [28–31] and black phosphorus [32], demonstrate different optical properties. They are always direct-gap even in a bulk form and spatial confinement does not essentially influence the optical response except the emission wavelength. The latter can be widely varied from 550 nm to 1.3 μm depending on the sheet dimensionality and material. Single-layer GaSe behaves as a non-linear crystal with strong second-harmonic generation under the nonresonant excitation [33].

Superconductors (for example, FeSe [34] and $NbSe_2$ [35]) and topological insulators (Bi_2Te_3 [36]) are also among the 2D films. Additionally, charge density waves have been detected in monolayer niobium selenide [35].

The quantum confinement in atomically thin sheets opens new opportunities for using well-known materials in novel electronic and optoelectronic applications. Physical parameters of these isolated mono- and few-layer sheets are often unique and inaccessible in other material systems. The fabrication of such structures can be compatible with a wide range of substrates and suitable for the production of flexible optoelectronic devices [37]. The formation of 2D alloys [38] and stacking the 2D crystals on top of each other (known as van der Waals heterostructures) [9, 39] provide a possibility to combine and manipulate the existing properties of the constituent materials as well as form novel characteristics. On the other hand, the research area of the ultrathin films and structures is quite new and requires detailed investigations and fundamental understanding. For this reason, our experimental work is concerned with the study of fundamental optical properties of the above structures, namely the single- and few-layer TMDCs, their alloys and heterostructures. A description of the main results on this topic, applied sample fabrication methods and optical spectroscopy techniques is outlined in this thesis.

1.2 Two-dimensional transition metal dichalcogenides

Among 2D materials, the TMDCs with atomic-scale thicknesses have many distinctive optical properties which are promising for optoelectronics [40]. The chemical formula of the TMDCs is MX_2 where M is a transitional metal element from group IV–X of the periodic table and X is one of the chalcogens (S, Se or Te). Over 40 different compounds behaving as semimetals, semiconductors and superconductors exist and some of them are not layered [41]. We measure the samples based on the semiconducting layered group-VI TMDCs, such as MoS_2, $MoSe_2$, WS_2 and WSe_2. Therefore, the information presented here focuses on these compounds. Their typical

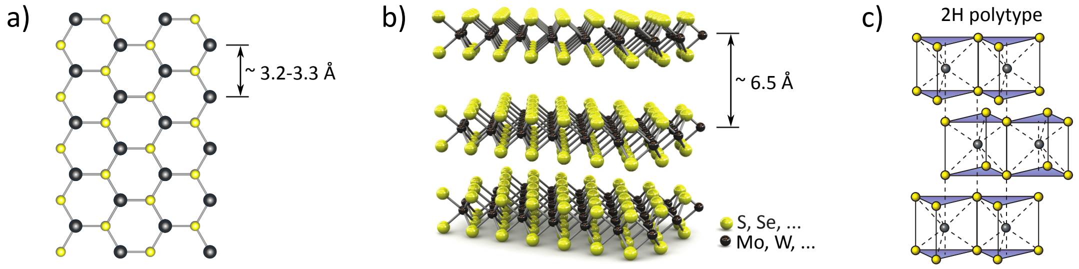

Fig. 1.1 The schematic representation of the typical layered structure of a TMDC material. (a) A single layer viewed from top. Metal and chalcogen atoms are black and yellow, respectively. The lattice constant is about 3.2–3.3 Å. (b) A three-dimensional perspective of the TMDCs. The interlayer spacing is approximately 6.5 Å. (c) The $2H$ structural polytype: hexagonal symmetry, two layers in the stacking order, trigonal prismatic coordination. Inversion symmetry is obtained in the few-layer sheets but not conserved in the monolayers. Figures (b) and (c) are reproduced from [48] and [40].

hexagonal crystal structure is shown in Fig. 1.1. Each metal atom is surrounded and strongly (covalently) bonded to six neighboring chalcogen atoms. A single layer is defined as a plane of metal atoms sandwiched between two planes of chalcogen atoms (Fig. 1.1b). Vertical stacking of those X-M-X layers coupled by weak van der Waals forces form the bulk crystal. The interlayer distance is $\sim$ 6.5 Å [40, 42] and the lattice constant $\sim$ 3.2–3.3 Å [43, 44]. The bulk TMDCs exhibit a variety of structural polymorphs [40, 41, 45], whereas the monolayers are found in two polytypes [41, 46] depending on the metal coordination in the X-M-X slabs: trigonal prismatic $2H$ ($1H$ for a single layer) with D_{3h} point group, honeycomb motif or octahedral $1T$ with D_{3d} point group, centered-honeycomb motif. Although the latter polytype is observed in chemically exfoliated films which are in a metastable metallic phase [47], the 2D TMDCs are mainly the $2H$ polymorphs in a thermodynamically stable semiconducting phase [46] (Fig. 1.1c).

The electronic structure of the TMDCs shows remarkable changes when the material is thinned down towards a single monolayer. Various research groups experimentally [23, 24] and theoretically [44, 49–52] establish the indirect-to-direct bandgap transition. As an example, calculated band structures of MoS_2 of different thicknesses using density functional theory, which is a computational quantum mechanical modelling method operating with functionals of the electron density, are demonstrated in Fig. 1.2 (first reported in [24]). An indirect bandgap, which equals

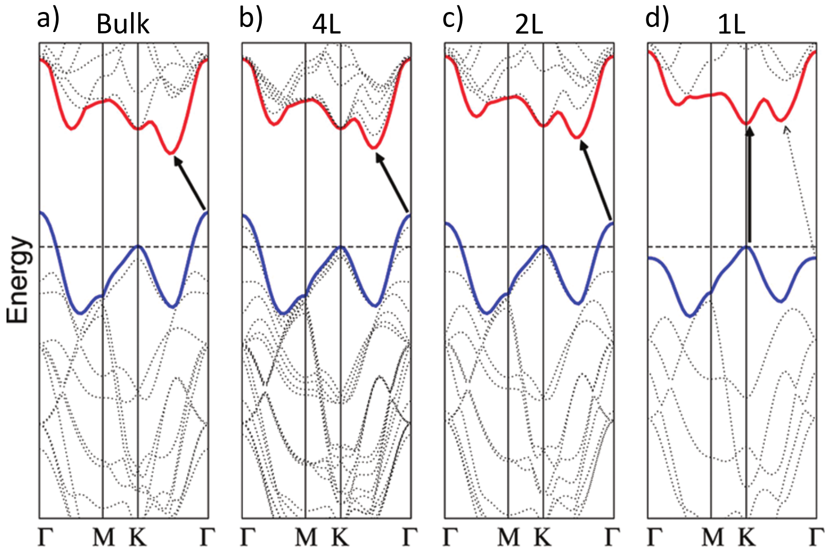

Fig. 1.2 Calculated electronic band structures of the (a) bulk, (b) quadrilayer, (c) bilayer and (d) monolayer MoS_2. Conduction- and valence-band edges are denoted with red and blue solid lines, respectively. Black solid arrows indicate the lowest energy transitions. $1L$, $2L$, $4L$ and *Bulk* refer to the film thicknesses, i. e. 1, 2, 4 atomic layers and bulk. Taken from [24].

1.3 eV for the bulk crystal, is between the Γ point in the valence band of the Brillouin zone and halfway across the Γ–K direction in the conduction band [24, 50, 53]. The influence of interlayer interactions and quantum confinement causes all modifications illustrated in Fig. 1.2. The states of both conduction and valence bands near the K point predominantly consist of the localized d orbitals of the transition metal atoms [52, 54–56], which are little affected by neighbouring atomic layers. A part of that is also presented in the states at the Γ point but they are significantly mixed with the p orbitals of the chalcogen atoms. This configuration has the strong interlayer coupling effect [24] which influences the indirect transition with the number of layers: an energy shift of the bands at the Γ point and negligible changes at the K point. The appearance of the direct bandgap near the K point reflects on the physical properties of the single-layer TMDCs. Especially, the photoluminescence (PL) intensity is drastically enhanced [23].

The partially filled metal d orbitals, especially d_{z^2}, d_{xy}, and $d_{x^2-y^2}$, are dominant components of the Bloch states of the monolayer TMDCs near the band edges [52–56]. The prismatic coordination divides those d orbitals into three subbands: $A_1'\{d_{z^2}\}$,

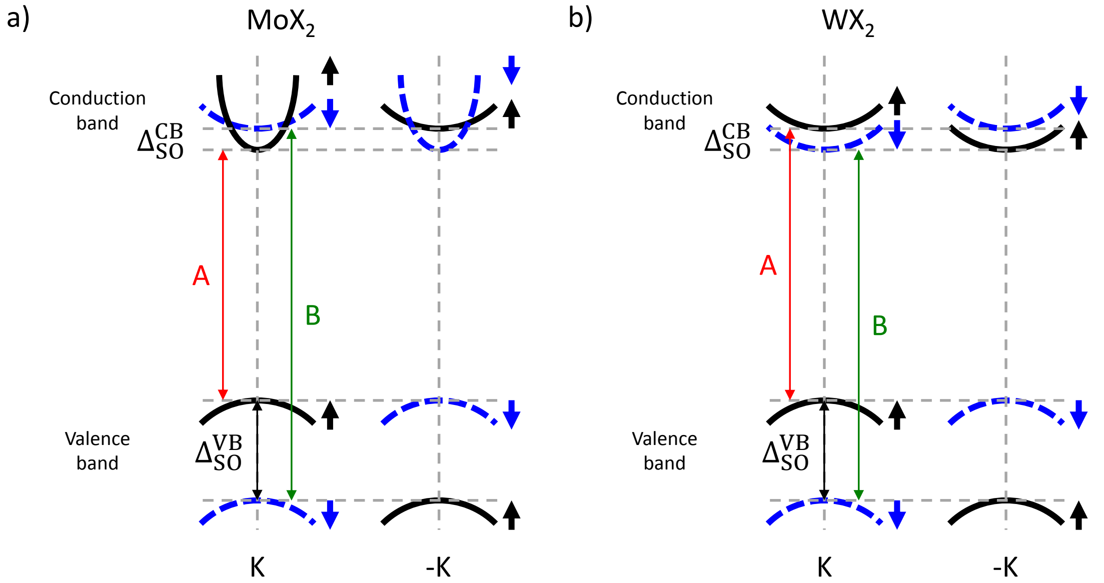

Fig. 1.3 Spin-orbit coupling at the $\pm K$ points of the Brillouin zone for the (a) molybdenum- and (b) tungsten-containing monolayers, MoX_2 and WX_2. Spin-up (black) and spin-down (blue) branches of the spin-split bands are depicted for electron states. Δ_{SO}^{CB} and Δ_{SO}^{VB} are the conduction- and valence-band spin splittings. Red and green arrows denote the states involved in optically bright A and B transitions, respectively (exciton binding energies are neglected for simplicity).

$E'\{d_{xy}, d_{x^2-y^2}\}$ and $E''\{d_{xz}, d_{yz}\}$. The reflection symmetry by the x-y plane leaves E'' decoupled and permits hybridization only between A'_1 and E', opening of the band gap at the K point [56–58]. The direct-gap structure reduces the symmetry at the band edges to the C_{3h} point group. The localization of the K-point conduction- and valence-band states in the heavy-metal atom plane originates another important phenomenon. Fig. 1.3 outlines the spin-orbit coupling (SOC) for the atomically thin tungsten and molybdenum dichalcogenides labelled as MoX_2 and WX_2. Such giant spin splitting (several hundreds of meV [54]) occurs with the the states mostly composed of metal atom d_{xy} and $d_{x^2-y^2}$ orbitals, bearing a magnetic quantum number $m = \pm 2$ [59, 60], in the valence band edges in the vicinity of the K point. Apart from the single layers, the spin-split valence bands are also observed in the few-layer and bulk materials [50, 61] owing to the combined interlayer interaction and SOC effect [50]. The electron states in the conduction-band minima of the TMDC atomic-scale sheets predominately contain spin degenerate d_{z^2} orbitals with zero magnetic quantum number [59, 60]. Nonetheless, the conduction-band spin splitting exists, has a finite small value (from several to several tens of meV [50, 52, 62–66]) and arises from the presence of the small fraction of other metal and chalcogen orbitals in those mixed d_{z^2} states [67]. Furthermore, the spin-split conduction bands are crossed in the MoX_2 (Fig. 1.3a) because of the specific spin dependence of the electron effective masses at the K point [57, 68]. This band crossing is absent in the WX_2 (Fig. 1.3b), resulting in the difference in the optical properties which will be discussed below.

In the bulk TMDCs, a combination of time-reversal ($E^{\uparrow}(k) = E^{\downarrow}(-k)$) and inversion ($E^{\uparrow}(k) = E^{\uparrow}(-k)$) symmetries forms Kramers degeneracy of energy bands in reciprocal space ($E^{\uparrow}(k) = E^{\downarrow}(k)$) [54, 69–72]. However, the 2D hexagonal lattice of the monolayers as clearly visible in Fig. 1.1a possesses spatial inversion asymmetry. The mentioned substantial valence-band spin splitting and broken inversion symmetry permit to introduce two different kinds of band edges of the Brillouin zone, K and $-K$ points (valleys), with opposite electron spins as shown in Fig. 1.3. This additional internal quantum degree of freedom (the so-called valley pseudospin with the valley index $\tau = \pm 1$ [58, 60]) leads to both the valley-contrasting Berry curvature and orbital magnetic moment, which manifest themselves in the valley Hall effect [58]. Inversion asymmetry also allows circular dichroism in different regions of the Brillouin zone, determining valley-dependent optical selection rules for interband transitions near high symmetry points (the K and $-K$ points): the right (σ^+) and left (σ^-) circularly polarized light can excite only the transition at K and $-K$, respectively [58–60, 73]. The following arguments confirm that fact: the valence-band orbital Bloch functions in the valleys are invariants, whereas the conduction-band states transform as states with angular momentum components of ±1 in accordance with the E_1'/E_2' irreducible representations of the C_{3h} point group [74]. The absorption of σ^+ (σ^-) photons causes the formation of the electron-hole pairs with the electron and hole valley indexes and spins $\tau_e = -\tau_h = +1$, $s_e = -s_h = +1/2$ ($\tau_e = -\tau_h = -1$, $s_e = -s_h = -1/2$) [75]. It is possible to reach the circular polarization degree of the PL of up to 100 % for the resonant excitation [73, 76, 77]. Moreover, a coherent superposition of the K and $-K$ valley states (known as the valley coherence) can be created, allowing to generate linearly polarized emission under the linearly polarized exciting light [78–80].

Similarly to other semiconductors, free electrons couple with free holes in the TMDCs so that Coulomb-bound pairs called excitons are formed. The strong SOC which yields the giant valence-band spin splitting influences the exciton properties. Two types of optical transitions, usually referred to as A and B, occur between the conduction and valence bands [23, 24] (indicated in Fig. 1.3 with no exciton binding energies depicted). Due to the reduced dimensionality, the nonlocal and reduced dielectric screening, increased effective masses of electrons and holes, strong enhancement of the Coulomb interactions and giant bandgap renormalization are features of the 2D TMDCs [74, 81–87] and provide excitons with extraordinarily large binding energies of hundreds of meV [50, 81–84] (for comparison, they are several meV in conventional III–V-based 2D semiconductor quantum wells [88, 89]). Having the small Bohr radii of ~ 0.5 nm in real space and large optical oscillator strength, excitons are still well described by the traditional Wannier-Mott model [84, 90–93]. A classical Wannier-Mott exciton has a radius larger than the lattice constant, hydrogen-like structure with Rydberg energy levels and is delocalized, i. e. not bound to atoms [90]. However, the excited excitonic states in the TMDC monolayers are characterized by a significant deviation from the hydrogenic Rydberg series owing to the reduced dielectric screening (so-called antiscreening effect) [83–85].

Along with the electron-hole pairs, other complex excitonic species are often observed in the single-layer TMDCs. In the doped materials, a neutral exciton can interact with an extra particle (electron or hole), forming a three-particle state — a charged exciton (or trion) [94]. The charge of the trions in the ‘naturally doped’ 2D TMDCs is mostly negative [48, 95, 96]. The binding energy of charged excitons is typically about 10 % of the exciton binding energy and equals a few tens of meV [74, 97]. In addition to those three-particle complexes, bound exciton-exciton pairs (or biexcitons) have been also detected (mainly in the monolayer WS_2) [98–101].

The neutral excitons are optically bright and contain charge carriers with parallel spins. Nevertheless, electron-hole pairs with anti-parallel spins can bind into optically dark excitons whose presence in the TMDC atomic films is predicted [57, 75, 87].

While the formation of the such quasiparticles and their impact on many-body interactions still require further investigation, the contribution of dark excitons to the optical properties of the atomic-layer TMDCs is established [102, 103]. As can be seen in Fig. 1.3, the lowest excitonic state in the 2D WX_2 compounds is dark in contrast to the MoX_2 monolayers. This results in the opposite behaviour of PL in the above structures with temperature growth: the emission intensity increases (decreases) in the WX_2 (MoX_2).

Carrier concentration, localization and thermalization effects influence many-body interactions including the formation, behaviour and lifetimes of neutral and charged excitons in the isolated single layers of the TMDCs. Through elastic Coulomb scattering, Pauli blocking and screening of the Coulomb interaction [104], the prominent modifications of the excitonic states and their PL occur with electron injection: broadening of the spectral peaks [99, 104], decrease in the exciton binding energy [91], blueshift (redshift) of the exciton (trion) transition energy [78, 98, 99, 105] and shrinkage of the band gap [104, 106]. Disorder potentials are formed by different types of defects, impurities and strain from the substrate in the 2D TMDC materials [107]. This may cause the presence of weakly localized excitons with slightly less energies than those of delocalized states, leading to inhomogeneous signal peak widening [107, 108]. Strong spatial localization refers to excitons in deep potential traps which serve as single photon emitters in some monolayers, such as WSe_2 [109–111]. In this case, the emission energy is much redshifted (tens of meV below the trion transition). Finally, the temperature-related phenomena are concerned with exciton-phonon interactions. Acoustic phonons dominate in those processes at low temperatures up to 50 K [108], while the exciton scattering with optical phonons exists at elevated temperatures. It is worth noting that both disorder and temperature suppress screening of the Coulomb interaction [106]. More information about the above-mentioned effects is given in subsection 4.1. Our complex study of the PL signal of the monolayer $MoSe_2$ under the charge injection and thermalization is first conducted and presented in chapter 4.

Nowadays, several fabrication methods exist to produce the ultrathin TMDC crystals: the aforementioned micromechanical cleaving or exfoliation [2, 23, 24], chemical vapour deposition [112–115], physical vapor phase growth [116, 117], liquid exfoliation with ion intercalation between atomic layers in a liquid environment [47, 118, 119] and special two-step thermolysis crystallization [120]. The micromechanical cleavage is used for our sample production and described in detail in chapter 2.

1.3 Transition metal dichalcogenide heterostructures and alloys

As discussed previously, one of the most prominent features of the TMDCs and all van der Waals materials is the weak interlayer bonding. This property enables creation of layered structures by vertical stacking of the 2D films on top of each other. Reviewed by Geim *et al.* [9], the principle of such heterostructure (HS) building is similar to a Lego construction where each atomic layer plays a role of the Lego block. Van der Waals forces between the sheets are sufficiently strong to keep the stacks together.

A combination of different crystals also means combination of properties and formation of new artificial materials. Van der Waals heterostructures are promising for a wide range of applications in electronics and optoelectronics: graphene-based field effect transistors with thin insulating hBN barriers [121], tunnelling diodes with negative differential conductance [122], ultrathin photovoltaic devices [123] and photodetectors [124], light-emitting diodes [125].

The HSs consisting of two group-VI TMDC monolayers mostly make a staggered (type-II) heterojunction in which the conduction band minimum (CBM) and the valence band maximum (VBM) are located in different layers [126, 127]. The schematic diagram with the calculated CBM and VBM is depicted in Fig. 1.4. Owing to a variety of band gaps and hence band offsets, the hybrid bilayers are good candidates for band gap engineering which reveals new energetic landscapes for optoelectronic applications and energy conversion.

After the ultrafast charge transfer [128, 129] in the type-II heterojunction, exci-

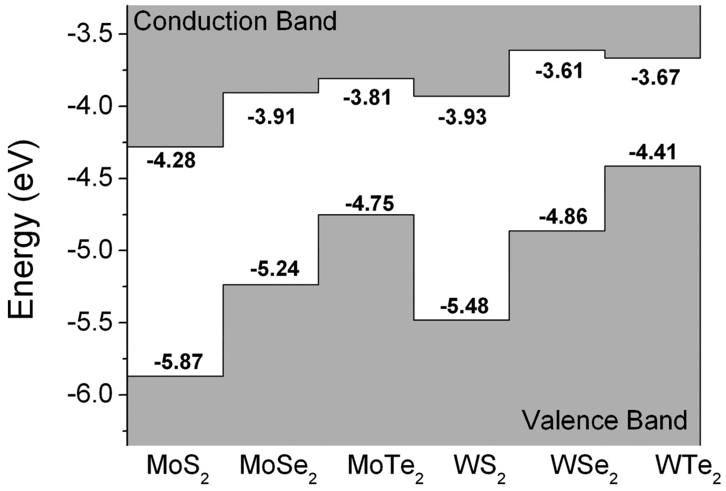

Fig. 1.4 The band alignment for the 2D group-VI TMDCs. The values of the band edges are calculated using the generalized gradient approximation of Perdew-Burke-Ernzerhof exchange-correlation functional [131]. Taken and altered from [126].

tons can only stay at van der Waals heterointerfaces. The observation of these interlayer excitons is determined and controlled by the crystal lattice alignment of the heterobilayer constituents [130]. On the whole, optical (in particular, excitonic) properties in such systems are very intriguing and still need to be explored due to the novelty of the research field. Our measurements in the $MoSe_2/WSe_2$ and $MoSe_2/WS_2$ HSs are described in chapter 5 including a detailed review of the current achievements in this area of study, presented in section 5.1.

For more precise tuning of the band gap and therefore better engineering of the performance of 2D material-based devices, the single-layer TMDC-containing alloys can be used. Alloying different materials allows to change the electronic structure and the lattice parameters [132]. For instance, the quasiparticle band gap values of the monolayer $Mo_xW_{1-x}S_2$ are decreased from 2.38 eV ($x = 0$) to 2.17 eV ($x = 1$) as well as the A exciton binding energies are varied from 420 meV to 310 meV with the increasing Mo concentration [133]. The 2D TMDC alloys will serve in devices based on semiconducting HSs where precise control of the band gap and band offsets will be required. In this thesis, we for the first time investigate the properties of a few-layer $Mo_xW_{1-x}S_2$ alloys as outlined in chapter 3.

Nowadays, the majority of the TMDC-based vertically stacked layered structures are built from the exfoliated materials using the common flake transfer techniques [134] discussed in section 2.1. Some other successful fabrication attempts are concerned with the chemical vapour deposition growth [135, 136]. Currently, scalable methods remain challenging.

References

[1] E. Gibney. The super materials that could trump graphene. *Nature* **522**, 274–276 (2015).

[2] K. S. Novoselov, A. K. Geim, S. V. Morozov, D. Jiang, Y. Zhang, S. V. Dubonos, I. V. Grigorieva, A. A. Firsov. Electric field effect in atomically thin carbon films. *Science* **306 (5696)**, 666–669 (2004).

[3] P. R. Wallace. The band theory of graphite. *Phys. Rev.* **71 (9)**, 622 (1947).

[4] A. K. Geim, K. S. Novoselov. The rise of graphene. *Nat. Mater.* **6**, 183–191 (2007).

[5] D. C. Elias, R. V. Gorbachev, A. S. Mayorov, S. V. Morozov, A. A. Zhukov, P. Blake, L. A. Ponomarenko, I. V. Grigorieva, K. S. Novoselov, F. Guinea, A. K. Geim. Dirac cones reshaped by interaction effects in suspended graphene. *Nat. Phys.* **7**, 701–704 (2011).

[6] C. Canali, C. Jacoboni, F. Nava, G. Ottaviani, A. Alberigi-Quaranta. Electron drift velocity in silicon. *Phys. Rev. B* **12 (6)**, 2265 (1975).

[7] K. I. Bolotin, K. J. Sikes, Z. Jiang, M. Klima, G. Fudenberg, J. Hone, P. Kim, H. L. Stormer. Ultrahigh electron mobility in suspended graphene. *Solid State Commun.* **146 (9-10)**, 351–355 (2008).

[8] K. S. Novoselov, Z. Jiang, Y. Zhang, S. V. Morozov, H. L. Stormer, U. Zeitler, J. C. Maan, G. S. Boebinger, P. Kim, A. K. Geim. Room-temperature quantum Hall effect in graphene. *Science* **315 (5817)**, 1379 (2007).

[9] A. K. Geim, I. V. Grigorieva. Van der Waals heterostructures. *Nature* **499**, 419–425 (2013).

[10] M. Yi, Z. Shen. A review on mechanical exfoliation for the scalable production of graphene. *J. Mater. Chem. A* **3 (22)**, 11700–11715 (2015).

[11] K. Watanabe, T. Taniguchi, H. Kanda. Direct-bandgap properties and evidence for ultraviolet lasing of hexagonal boron nitride single crystal. *Nat. Mater.* **3**, 404–409 (2004).

[12] L. Song, L. Ci, H. Lu, P. B. Sorokin, C. Jin, J. Ni, A. G. Kvashnin, D. G. Kvashnin, J. Lou, B. I. Yakobson, P. M. Ajayan. Large scale growth and characterization of atomic hexagonal boron nitride layers. *Nano Lett.* **10 (8)**, 3209–3215 (2010).

[13] B. Arnaud, S. Lebègue, P. Rabiller, M. Alouani. Huge excitonic effects in layered hexagonal boron nitride. *Phys. Rev. Lett.* **96 (2)**, 026402 (2006).

[14] C. R. Dean, A. F. Young, I. Meric, C. Lee, L. Wang, S. Sorgenfrei, K. Watanabe, T. Taniguchi, P. Kim, K. L. Shepard, J. Hone. Boron nitride substrates for high-quality graphene electronics. *Nat. Nanotechnol.* **5**, 722–726 (2010).

[15] G.-H. Lee, Y.-J. Yu, C. Lee, C. Dean, K. L. Shepard, P. Kim, J. Hone. Electron tunneling through atomically flat and ultrathin hexagonal boron nitride. *Appl. Phys. Lett.* **99 (24)**, 243114 (2011).

[16] L. Britnell, R. V. Gorbachev, R. Jalil, B. D. Belle, F. Schedin, M. I. Katsnelson, L. Eaves, S. V. Morozov, A. S. Mayorov, N. M. R. Peres, A. H. Castro Neto, J. Leist, A. K. Geim, L. A. Ponomarenko, K. S. Novoselov. Electron tunneling through ultrathin boron nitride crystalline barriers. *Nano Lett.* **12 (3)**, 1707–1710 (2012).

[17] L. A. Ponomarenko, A. K. Geim, A. A. Zhukov, R. Jalil, S. V. Morozov, K. S. Novoselov, I. V. Grigorieva, E. H. Hill, V. V. Cheianov, V. I. Fal'ko,

K. Watanabe, T. Taniguchi, R. V. Gorbachev. Tunable metal–insulator transition in double-layer graphene heterostructures. *Nat. Phys.* **7**, 958–961 (2011).

[18] I. Meric, C. Dean, A. Young, J. Hone, P. Kim, K. L. Shepard. Graphene field-effect transistors based on boron nitride gate dielectrics. *2010 Int. Electron Devices Meet.* **10**, 556–559 (2010).

[19] A. S. Mayorov, R. V. Gorbachev, S. V. Morozov, L. Britnell, R. Jalil, L. A. Ponomarenko, P. Blake, K. S. Novoselov, K. Watanabe, T. Taniguchi, A. K. Geim. Micrometer-scale ballistic transport in encapsulated graphene at room temperature. *Nano Lett.* **11 (6)**, 2396–2399 (2011).

[20] Y. Cao, A. Mishchenko, G. L. Yu, E. Khestanova, A. P. Rooney, E. Prestat, A. V. Kretinin, P. Blake, M. B. Shalom, C. Woods, J. Chapman, G. Balakrishnan, I. V. Grigorieva, K. S. Novoselov, B. A. Piot, M. Potemski, K. Watanabe, T. Taniguchi, S. J. Haigh, A. K. Geim, R. V. Gorbachev. Quality heterostructures from two-dimensional crystals unstable in air by their assembly in inert atmosphere. *Nano Lett.* **15 (8)**, 4914–4921 (2015).

[21] J.-S. Kim, Y. Liu, W. Zhu, S. Kim, D. Wu, L. Tao, A. Dodabalapur, K. Lai, D. Akinwande. Toward air-stable multilayer phosphorene thin-films and transistors. *Sci. Rep.* **5**, 8989 (2015).

[22] A. I. Brudnyi, A. F. Karmadonov. Structure of molybdenum disulphide lubricant film. *Wear* **33 (2)**, 243–249 (1975).

[23] K. F. Mak, C. Lee, J. Hone, J. Shan, T. F. Heinz. Atomically thin MoS_2: a new direct-gap semiconductor. *Phys. Rev. Lett.* **105 (13)**, 136805 (2010).

[24] A. Splendiani, L. Sun, Y. Zhang, T. Li, J. Kim, C.-Y. Chim, G. Galli, F. Wang. Emerging photoluminescence in monolayer MoS_2. *Nano Lett.* **10 (4)**, 1271–1275 (2010).

[25] P. Tonndorf, R. Schmidt, P. Böttger, X. Zhang, J. Börner, A. Liebig, M. Albrecht, C. Kloc, O. Gordan, D. R. T. Zahn, S. Michaelis de Vasconcellos,

R. Bratschitsch. Photoluminescence emission and Raman response of monolayer MoS_2, $MoSe_2$, and WSe_2. *Opt. Express* **21 (4)**, 4908–4916 (2013).

[26] H. R. Gutiérrez, N. Perea-López, A. L. Elías, A. Berkdemir, B. Wang, R. Lv, F. López-Urías, V. H. Crespi, H. Terrones, M. Terrones. Extraordinary room-temperature photoluminescence in triangular WS_2 monolayers. *Nano Lett.* **13 (8)**, 3447–3454 (2013).

[27] T. Yan, X. Qiao, X. Liu, P. Tan, X. Zhang. Photoluminescence properties and exciton dynamics in monolayer WSe_2. *Appl. Phys. Lett.* **105 (10)**, 101901 (2014).

[28] G. W. Mudd, S. A. Svatek, T. Ren, A. Patanè, O. Makarovsky, L. Eaves, P. H. Beton, Z. D. Kovalyuk, G. V. Lashkarev, Z. R. Kudrynskyi, A. I. Dmitriev. Tuning the bandgap of exfoliated InSe nanosheets by quantum confinement. *Adv. Mater.* **25 (40)**, 5714–5718 (2013).

[29] R. D. Rodriguez, S. Müller, E. Sheremet, D. R. T. Zahn, A. Villabona, S. A. Lopez-Rivera, P. Tonndorf, S. Michaelis de Vasconcellos, R. Bratschitsch. Selective Raman modes and strong photoluminescence of gallium selenide flakes on sp^2 carbon. *J. Vac. Sci. Technol., B* **32 (4)**, 04E106 (2014).

[30] O. Del Pozo-Zamudio, S. Schwarz, M. Sich, I. A. Akimov, M. Bayer, R. C. Schofield, E. A. Chekhovich, B. J. Robinson, N. D. Kay, O. V. Kolosov, A. I. Dmitriev, G. V. Lashkarev, D. N. Borisenko, N. N. Kolesnikov, A. I. Tartakovskii. Photoluminescence of two-dimensional GaTe and GaSe films. *2D Mater.* **2 (3)**, 035010 (2015).

[31] I. M. Catalano, M. Ferrara, P. Tantalo. Luminescence and photocurrent of gallium sulphide. *Phys. Status Solidi A* **20 (2)**, K135–K138 (1973).

[32] H. Liu, A. T. Neal, Z. Zhu, Z. Luo, X. Xu, D. Tománek, P. D. Ye. Phosphorene: an unexplored 2D semiconductor with a high hole mobility. *ACS Nano* **8 (4)**, 4033–4041 (2014).

[33] X. Zhou, J. Cheng, Y. Zhou, T. Cao, H. Hong, Z. Liao, S. Wu, H. Peng, K. Liu, D. Yu. Strong second-harmonic generation in atomic layered GaSe. *J. Am. Chem. Soc.* **137 (25)**, 7994–7997 (2015).

[34] D. Liu, W. Zhang, D. Mou, J. He, Y.-B. Ou, Q. Y. Wang, Z. Li, L. Wang, L. Zhao, S. He, Y. Peng, X. Liu, Chaoyu Chen, L. Yu, G. Liu, X. Dong, J. Zhang, Chuangtian Chen, Z. Xu, J. Hu, X. Chen, X. Ma, Q. Xue, X. J. Zhou. Electronic origin of high-temperature superconductivity in single-layer FeSe superconductor. *Nat. Commun.* **3**, 931 (2012).

[35] X. Xi, L. Zhao, Z. Wang, H. Berger, L. Forró, J. Shan, K. F. Mak. Strongly enhanced charge-density-wave order in monolayer $NbSe_2$. *Nat. Nanotechnol.* **10**, 765–769 (2015).

[36] D. Teweldebrhan, V. Goyal, A. A. Balandin. Exfoliation and characterization of bismuth telluride atomic quintuples and quasi-two-dimensional crystals. *Nano Lett.* **10 (4)**, 1209–1218 (2010).

[37] S.-K. Lee, H. Y. Jang, S. Jang, E. Choi, B. H. Hong, J. Lee, S. Park, J.-H. Ahn. All graphene-based thin film transistors on flexible plastic substrates. *Nano Lett.* **12 (7)**, 3472–3476 (2012).

[38] L. M. Xie. Two-dimensional transition metal dichalcogenide alloys: preparation, characterization and applications. *Nanoscale* **7 (44)**, 18392–18401 (2015).

[39] H. Fang, C. Battaglia, C. Carraro, S. Nemsak, B. Ozdol, J. S. Kang, H. A. Bechtel, S. B. Desai, F. Kronast, A. A. Unal, G. Conti, C. Conlon, G. K. Palsson, M. C. Martin, A. M. Minor, C. S. Fadley, E. Yablonovitch, R. Maboudian, A. Javey. Strong interlayer coupling in van der Waals heterostructures built from single-layer chalcogenides. *Proc. Natl. Acad. Sci. U.S.A.* **111 (17)**, 6198–6202 (2014).

[40] Q. H. Wang, K. Kalantar-Zadeh, A. Kis, J. N. Coleman, M. S. Strano. Electronics and optoelectronics of two-dimensional transition metal dichalcogenides. *Nat. Nanotechnol.* **7**, 699–712 (2012).

[41] M. Chhowalla, H. S. Shin, G. Eda, L.-J. Li, K. P. Loh, H. Zhang. The chemistry of two-dimensional layered transition metal dichalcogenide nanosheets. *Nat. Chem.* **5**, 263–275 (2013).

[42] R. F. Frindt. Single crystals of $\mathrm{MoS_2}$ several molecular layers thick. *J. Appl. Phys.* **37 (4)**, 1928 (1966).

[43] Y. Ding, Y. Wang, J. Ni, L. Shi, S. Shi, W. Tang. First principles study of structural, vibrational and electronic properties of graphene-like MX_2 (M = Mo, Nb, W, Ta; X = S, Se, Te) monolayers. *Physica B* **406 (11)**, 2254–2260 (2011).

[44] A. Kumar, P. K. Ahluwalia. Electronic structure of transition metal dichalcogenides monolayers $1H$-MX_2 (M = Mo, W; X = S, Se, Te) from *ab-initio* theory: new direct band gap semiconductors. *Eur. Phys. J. B* **85**, 186 (2012).

[45] N. V. Podberezskaya, S. A. Magarill, N. V. Pervukhina, S. V. Borisov. Crystal chemistry of dichalcogenides MX_2. *J. Struct. Chem.* **42 (4)**, 654–681 (2001).

[46] D. Jariwala, V. K. Sangwan, L. J. Lauhon, T. J. Marks, M. C. Hersam. Emerging device applications for semiconducting two-dimensional transition metal dichalcogenides. *ACS Nano* **8 (2)**, 1102–1120 (2014).

[47] G. Eda, H. Yamaguchi, D. Voiry, T. Fujita, M. Chen, M. Chhowalla. Photoluminescence from chemically exfoliated $\mathrm{MoS_2}$. *Nano Lett.* **11 (12)**, 5111–5116 (2011).

[48] B. Radisavljevic, A. Radenovic, J. Brivio, V. Giacometti, A. Kis. Single-layer $\mathrm{MoS_2}$ transistors. *Nat. Nanotechnol.* **6**, 147–150 (2011).

[49] A. Kuc, N. Zibouche, T. Heine. Influence of quantum confinement on the electronic structure of the transition metal sulfide $T\mathrm{S_2}$. *Phys. Rev. B* **83 (24)**, 245213 (2011).

[50] T. Cheiwchanchamnangij, W. R. L. Lambrecht. Quasiparticle band structure calculation of monolayer, bilayer, and bulk $\mathrm{MoS_2}$. *Phys. Rev. B* **85 (20)**, 205302 (2012).

[51] W. S. Yun, S. W. Han, S. C. Hong, I. G. Kim, J. D. Lee. Thickness and strain effects on electronic structures of transition metal dichalcogenides: $2H$-MX_2 semiconductors ($M =$ Mo, W; $X =$ S, Se, Te). *Phys. Rev. B* **85 (3)**, 033305 (2012).

[52] E. S. Kadantsev, P. Hawrylak. Electronic structure of a single $\mathrm{MoS_2}$ monolayer. *Solid State Commun.* **152 (10)**, 909–913 (2012).

[53] S. Lebègue, O. Eriksson. Electronic structure of two-dimensional crystals from *ab initio* theory. *Phys. Rev. B* **79 (11)**, 115409 (2009).

[54] Z. Y. Zhu, Y. C. Cheng, U. Schwingenschlögl. Giant spin-orbit-induced spin splitting in two-dimensional transition-metal dichalcogenide semiconductors. *Phys. Rev. B* **84 (15)**, 153402 (2011).

[55] R. A. Bromley, R. B. Murray, A. D. Yoffe. The band structures of some transition metal dichalcogenides. III. Group VIA: trigonal prism materials. *J. Phys. C: Solid State Phys.* **5 (7)**, 759 (1972).

[56] L. F. Mattheiss. Band structures of transition-metal-dichalcogenide layer compounds. *Phys. Rev. B* **8 (8)**, 3719 (1973).

[57] G.-B. Liu, W.-Y. Shan, Y. Yao, W. Yao, D. Xiao. Three-band tight-binding model for monolayers of group-VIB transition metal dichalcogenides. *Phys. Rev. B* **88 (8)**, 085433 (2013).

[58] D. Xiao, G.-B. Liu, W. Feng, X. Xu, W. Yao. Coupled spin and valley physics in monolayers of $\mathrm{MoS_2}$ and other group-VI dichalcogenides. *Phys. Rev. Lett.* **108 (19)**, 196802 (2012).

[59] T. Cao, G. Wang, W. Han, H. Ye, C. Zhu, J. Shi, Q. Niu, P. Tan, E. Wang, B. Liu, J. Feng. Valley-selective circular dichroism of monolayer molybdenum disulphide. *Nat. Commun.* **3**, 887 (2012).

[60] X. Xu, W. Yao, D. Xiao, T. F. Heinz. Spin and pseudospins in layered transition metal dichalcogenides. *Nat. Phys.* **10**, 343–350 (2014).

[61] R. Coehoorn, C. Haas, R. A. de Groot. Electronic structure of $MoSe_2$, MoS_2 and WSe_2. II. The nature of the optical band gaps. *Phys. Rev. B* **35 (12)**, 6203 (1987).

[62] H. Zeng, B. Zhu, K. Liu, J. Fan, X. Cui, Q. M. Zhang. Low-frequency Raman modes and electronic excitations in atomically thin MoS_2 films. *Phys. Rev. B* **86 (24)**, 241301(R) (2012).

[63] H. Zeng, G.-B. Liu, J. Dai, Y. Yan, B. Zhu, R. He, L. Xie, S. Xu, X. Chen, W. Yao, X. Cui. Optical signature of symmetry variations and spin-valley coupling in atomically thin tungsten dichalcogenides. *Sci. Rep.* **3**, 1608 (2013).

[64] K. Kośmider, J. Fernández-Rossier. Electronic properties of the MoS_2-WS_2 heterojunction. *Phys. Rev. B* **87 (7)**, 075451 (2013).

[65] Y. Song, H. Dery. Transport theory of monolayer transition-metal dichalcogenides through symmetry. *Phys. Rev. Lett.* **111 (2)**, 026601 (2013).

[66] A. Kormányos, V. Zólyomi, N. D. Drummond, P. Rakyta, G. Burkard, V. I. Fal'ko. Monolayer MoS_2: trigonal warping, the Γ valley, and spin-orbit coupling effects. *Phys. Rev. B* **88 (4)**, 045416 (2013).

[67] W. Feng, Y. Yao, W. Zhu, J. Zhou, W. Yao, D. Xiao. Intrinsic spin Hall effect in monolayers of group-VI dichalcogenides: a first-principles study. *Phys. Rev. B* **86 (16)**, 165108 (2012).

[68] A. Kormányos, V. Zólyomi, N. D. Drummond, G. Burkard. Spin-orbit coupling, quantum dots, and qubits in monolayer transition metal dichalcogenides. *Phys. Rev. X* **4 (1)**, 011034 (2014).

[69] C. Kittel. *Quantum theory of solids* (John Wiley & Sons, Inc., New York, USA, 1963), 1st edn. ISBN: 9780471490258.

[70] J. M. Ziman. *Principles of the theory of solids* (Cambridge University Press, Cambridge, UK, 1972), 2nd edn. ISBN: 9780521083829.

[71] S. LaShell, B. A. McDougall, E. Jensen. Spin splitting of an Au(111) surface state band observed with angle resolved photoelectron spectroscopy. *Phys. Rev. Lett.* **77 (16)**, 3419 (1996).

[72] Y. M. Koroteev, G. Bihlmayer, J. E. Gayone, E. V. Chulkov, S. Blügel, P. M. Echenique, P. Hofmann. Strong spin-orbit splitting on Bi surfaces. *Phys. Rev. Lett.* **93 (4)**, 046403 (2004).

[73] K. F. Mak, K. He, J. Shan, T. F. Heinz. Control of valley polarization in monolayer MoS_2 by optical helicity. *Nat. Nanotechnol.* **7**, 494–498 (2012).

[74] G. Wang, A. Chernikov, M. M. Glazov, T. F. Heinz, X. Marie, T. Amand, B. Urbaszek. *Colloquium*: excitons in atomically thin transition metal dichalcogenides. *Rev. Mod. Phys.* **90 (2)**, 021001 (2018).

[75] M. M. Glazov, T. Amand, X. Marie, D. Lagarde, L. Bouet, B. Urbaszek. Exciton fine structure and spin decoherence in monolayers of transition metal dichalcogenides. *Phys. Rev. B* **89 (20)**, 201302(R) (2014).

[76] G. Sallen, L. Bouet, X. Marie, G. Wang, C. R. Zhu, W. P. Han, Y. Lu, P. H. Tan, T. Amand, B. L. Liu, B. Urbaszek. Robust optical emission polarization in MoS_2 monolayers through selective valley excitation. *Phys. Rev. B* **86 (8)**, 081301(R) (2012).

[77] G. Kioseoglou, A. T. Hanbicki, M. Currie, A. L. Friedman, B. T. Jonker. Optical polarization and intervalley scattering in single layers of MoS_2 and $MoSe_2$. *Sci. Rep.* **6**, 25041 (2016).

[78] A. M. Jones, H. Yu, N. J. Ghimire, S. Wu, G. Aivazian, J. S. Ross, B. Zhao, J. Yan, D. G. Mandrus, D. Xiao, W. Yao, X. Xu. Optical generation of excitonic valley coherence in monolayer WSe_2. *Nat. Nanotechnol.* **8**, 634–638 (2013).

[79] G. Wang, L. Bouet, D. Lagarde, M. Vidal, A. Balocchi, T. Amand, X. Marie, B. Urbaszek. Valley dynamics probed through charged and neutral exciton emission in monolayer WSe_2. *Phys. Rev. B* **90 (7)**, 075413 (2014).

[80] R. Schmidt, A. Arora, G. Plechinger, P. Nagler, A. Granados del Águila, M. V. Ballottin, P. C. M. Christianen, S. Michaelis de Vasconcellos, C. Schüller, T. Korn, R. Bratschitsch. Magnetic-field-induced rotation of polarized light emission from monolayer WS_2. *Phys. Rev. Lett.* **117 (7)**, 077402 (2016).

[81] A. Ramasubramaniam. Large excitonic effects in monolayers of molybdenum and tungsten dichalcogenides. *Phys. Rev. B* **86 (11)**, 115409 (2012).

[82] H. P. Komsa, A. V. Krasheninnikov. Effects of confinement and environment on the electronic structure and exciton binding energy of MoS_2 from first principles. *Phys. Rev. B* **86 (24)**, 241201(R) (2012).

[83] K. He, N. Kumar, L. Zhao, Z. Wang, K. F. Mak, H. Zhao, J. Shan. Tightly bound excitons in monolayer WSe_2. *Phys. Rev. Lett.* **113 (2)**, 026803 (2014).

[84] A. Chernikov, T. C. Berkelbach, H. M. Hill, A. Rigosi, Y. Li, O. B. Aslan, D. R. Reichman, M. S. Hybertsen, T. F. Heinz. Exciton binding energy and nonhydrogenic Rydberg series in monolayer WS_2. *Phys. Rev. Lett.* **113 (7)**, 076802 (2014).

[85] T. Stroucken, S. W. Koch. Optically bright *p*-excitons indicating strong Coulomb coupling in transition-metal dichalcogenides. *J. Phys. Condens. Matter* **27 (34)**, 345003 (2015).

[86] M. M. Ugeda, A. J. Bradley, S.-F. Shi, F. H. da Jornada, Y. Zhang, D. Y. Qiu, W. Ruan, S.-K. Mo, Z. Hussain, Z.-X. Shen, F. Wang, S. G. Louie, M. F. Crommie. Giant bandgap renormalization and excitonic effects in a monolayer

transition metal dichalcogenide semiconductor. *Nat. Mater.* **13**, 1091–1095 (2014).

[87] A. Kormányos, G. Burkard, M. Gmitra, J. Fabian, V. Zólyomi, N. D. Drummond, V. Fal'ko. **k·p** theory for two-dimensional transition metal dichalcogenide semiconductors. *2D Mater.* **2 (2)**, 022001 (2015).

[88] R. C. Miller, D. A. Kleinman, W. T. Tsang, A. C. Gossard. Observation of the excited level of excitons in GaAs quantum wells. *Phys. Rev. B* **24 (2)**, 1134(R) (1981).

[89] R. L. Greene, K. K. Bajaj, D. E. Phelps. Energy levels of Wannier excitons in GaAs-$\text{Ga}_{1-x}\text{Al}_x$As quantum-well structures. *Phys. Rev. B* **29 (4)**, 1807 (1984).

[90] H. Haug, S. W. Koch. *Quantum theory of the optical and electronic properties of semiconductors* (World Scientific Publishing Co. Pte. Ltd, Singapore, 2009), 5th edn. ISBN: 9789812838834.

[91] C. Zhang, H. Wang, W. Chan, C. Manolatou, F. Rana. Absorption of light by excitons and trions in monolayers of metal dichalcogenide MoS_2: experiments and theory. *Phys. Rev. B* **89 (20)**, 205436 (2014).

[92] C. Robert, D. Lagarde, F. Cadiz, G. Wang, B. Lassagne, T. Amand, A. Balocchi, P. Renucci, S. Tongay, B. Urbaszek, X. Marie. Exciton radiative lifetime in transition metal dichalcogenide monolayers. *Phys. Rev. B* **93 (20)**, 205423 (2016).

[93] H. Wang, C. Zhang, W. Chan, C. Manolatou, S. Tiwari, F. Rana. Radiative lifetimes of excitons and trions in monolayers of the metal dichalcogenide MoS_2. *Phys. Rev. B* **93 (4)**, 045407 (2016).

[94] K. Kheng, R. T. Cox, Y. Merle d'Aubigné, F. Bassani, K. Saminadayar, S. Tatarenko. Observation of negatively charged excitons X^- in semiconductor quantum wells. *Phys. Rev. Lett.* **71 (11)**, 1752 (1993).

[95] A. Ayari, E. Cobas, O. Ogundadegbe, M. S. Fuhrer. Realization and electrical characterization of ultrathin crystals of layered transition-metal dichalcogenides. *J. Appl. Phys.* **101 (1)**, 014507 (2007).

[96] J. S. Ross, S. Wu, H. Yu, N. J. Ghimire, A. M. Jones, G. Aivazian, J. Yan, D. G. Mandrus, D. Xiao, W. Yao, X. Xu. Electrical control of neutral and charged excitons in a monolayer semiconductor. *Nat. Commun.* **4**, 1474 (2013).

[97] M. Van der Donck, M. Zarenia, F. M. Peeters. Excitons and trions in monolayer transition metal dichalcogenides: a comparative study between the multiband model and the quadratic single-band model. *Phys. Rev. B* **96 (3)**, 035131 (2017).

[98] G. Plechinger, P. Nagler, J. Kraus, N. Paradiso, C. Strunk, C. Schüller, T. Korn. Identification of excitons, trions and biexcitons in single-layer WS_2. *Phys. Status Solidi Rapid Res. Lett.* **9 (8)**, 457–461 (2015).

[99] J. Shang, X. Shen, C. Cong, N. Peimyoo, B. Cao, M. Eginligil, T. Yu. Observation of excitonic fine structure in a 2D transition-metal dichalcogenide semiconductor. *ACS Nano* **9 (1)**, 647–655 (2015).

[100] C. Mai, A. Barrette, Y. Yu, Y. G. Semenov, K. W. Kim, L. Cao, K. Gundogdu. Many-body effects in valleytronics: direct measurement of valley lifetimes in single-layer MoS_2. *Nano Lett.* **14 (1)**, 202–206 (2014).

[101] Y. You, X.-X. Zhang, T. C. Berkelbach, M. S. Hybertsen, D. R. Reichman, T. F. Heinz. Observation of biexcitons in monolayer WSe_2. *Nat. Phys.* **11**, 477–481 (2015).

[102] A. Arora, M. Koperski, K. Nogajewski, J. Marcus, C. Faugeras, M. Potemski. Excitonic resonances in thin films of WSe_2: from monolayer to bulk material. *Nanoscale* **7 (23)**, 10421–10429 (2015).

[103] A. Arora, K. Nogajewski, M. Molas, M. Koperski, M. Potemski. Exciton band structure in layered $MoSe_2$: from a monolayer to the bulk limit. *Nanoscale* **7 (48)**, 20769–20775 (2015).

[104] A. Chernikov, A. M. van der Zande, H. M. Hill, A. F. Rigosi, A. Velauthapillai, J. Hone, T. F. Heinz. Electrical tuning of exciton binding energies in monolayer WS_2. *Phys. Rev. Lett.* **115 (12)**, 126802 (2015).

[105] K. F. Mak, K. He, C. Lee, G. H. Lee, J. Hone, T. F. Heinz, J. Shan. Tightly bound trions in monolayer MoS_2. *Nat. Mater.* **12**, 207–211 (2013).

[106] B. Scharf, Z. Wang, D. V. Tuan, J. Shan, K. F. Mak, I. Zutic, H. Dery. Probing many-body interactions in monolayer transition-metal dichalcogenides. *Preprint at https://arxiv.org/abs/1606.07101* (2016).

[107] A. Singh, G. Moody, K. Tran, M. E. Scott, V. Overbeck, G. Berghäuser, J. Schaibley, E. J. Seifert, D. Pleskot, N. M. Gabor, J. Yan, D. G. Mandrus, M. Richter, E. Malic, X. Xu, X. Li. Trion formation dynamics in monolayer transition metal dichalcogenides. *Phys. Rev. B* **93 (4)**, 041401(R) (2016).

[108] G. Moody, C. K. Dass, K. Hao, C.-H. Chen, L.-J. Li, A. Singh, K. Tran, G. Clark, X. Xu, G. Berghäuser, E. Malic, A. Knorr, X. Li. Intrinsic homogeneous linewidth and broadening mechanisms of excitons in monolayer transition metal dichalcogenides. *Nat. Commun.* **6**, 8315 (2015).

[109] A. Srivastava, M. Sidler, A. V. Allain, D. S. Lembke, A. Kis, A. Imamoğlu. Optically active quantum dots in monolayer WSe_2. *Nat. Nanotechnol.* **10**, 491–496 (2015).

[110] Y.-M. He, G. Clark, J. R. Schaibley, Y. He, M.-C. Chen, Y.-J. Wei, X. Ding, Q. Zhang, W. Yao, X. Xu, C.-Y. Lu, J.-W. Pan. Single quantum emitters in monolayer semiconductors. *Nat. Nanotechnol.* **10**, 497–502 (2015).

[111] M. Koperski, K. Nogajewski, A. Arora, V. Cherkez, P. Mallet, J. Y. Veuillen, J. Marcus, P. Kossacki, M. Potemski. Single photon emitters in exfoliated WSe_2 structures. *Nat. Nanotechnol.* **10**, 503–506 (2015).

[112] Y.-H. Lee, X.-Q. Zhang, W. Zhang, M.-T. Chang, C.-T. Lin, K.-D. Chang, Y.-C. Yu, J. T.-W. Wang, C.-S. Chang, L.-J. Li, T.-W. Lin. Synthesis of large-area MoS_2 atomic layers with chemical vapor deposition. *Adv. Mater.* **24 (17)**, 2320–2325 (2012).

[113] C. Cong, J. Shang, X. Wu, B. Cao, N. Peimyoo, C. Qiu, L. Sun, T. Yu. Synthesis and optical properties of large-area single-crystalline 2D semiconductor WS_2 monolayer from chemical vapor deposition. *Adv. Opt. Mater.* **2 (2)**, 131–136 (2014).

[114] J.-K. Huang, J. Pu, C.-L. Hsu, M.-H. Chiu, Z.-Y. Juang, Y.-H. Chang, W.-H. Chang, Y. Iwasa, T. Takenobu, L.-J. Li. Large-area synthesis of highly crystalline WSe_2 monolayers and device applications. *ACS Nano* **8 (1)**, 923–930 (2014).

[115] X. Wang, Y. Gong, G. Shi, W. L. Chow, K. Keyshar, G. Ye, R. Vajtai, J. Lou, Z. Liu, E. Ringe, B. K. Tay, P. M. Ajayan. Chemical vapor deposition growth of crystalline monolayer $MoSe_2$. *ACS Nano* **8 (5)**, 5125–5131 (2014).

[116] Y. Zhan, Z. Liu, S. Najmaei, P. M. Ajayan, J. Lou. Large-area vapor-phase growth and characterization of MoS_2 atomic layers on a SiO_2 substrate. *Small* **8 (7)**, 966–971 (2012).

[117] S. Najmaei, Z. Liu, W. Zhou, X. Zou, G. Shi, S. Lei, B. I. Yakobson, J.-C. Idrobo, P. M. Ajayan, J. Lou. Vapour phase growth and grain boundary structure of molybdenum disulphide atomic layers. *Nat. Mater.* **12**, 754–759 (2013).

[118] J. N. Coleman, M. Lotya, A. O'Neill, S. D. Bergin, P. J. King, U. Khan, K. Young, A. Gaucher, S. De, R. J. Smith, I. V. Shvets, S. K. Arora,

G. Stanton, H.-Y. Kim, K. Lee, G. T. Kim, G. S. Duesberg, T. Hallam, J. J. Boland, J. J. Wang, J. F. Donegan, J. C. Grunlan, G. Moriarty, A. Shmeliov, R. J. Nicholls, J. M. Perkins, E. M. Grieveson, K. Theuwissen, D. W. McComb, P. D. Nellist, V. Nicolosi. Two-dimensional nanosheets produced by liquid exfoliation of layered materials. *Science* **331 (6017)**, 568–571 (2011).

[119] V. Nicolosi, M. Chhowalla, M. G. Kanatzidis, M. S. Strano, J. N. Coleman. Liquid exfoliation of layered materials. *Science* **340 (6139)**, 1226419 (2013).

[120] K.-K. Liu, W. Zhang, Y.-H. Lee, Y.-C. Lin, M.-T. Chang, C.-Y. Su, C.-S. Chang, H. Li, Y. Shi, H. Zhang, C.-S. Lai, L.-J. Li. Growth of large-area and highly crystalline MoS_2 thin layers on insulating substrates. *Nano Lett.* **12 (3)**, 1538–1544 (2012).

[121] L. Britnell, R. V. Gorbachev, R. Jalil, B. D. Belle, F. Schedin, A. Mishchenko, T. Georgiou, M. I. Katsnelson, L. Eaves, S. V. Morozov, N. M. R. Peres, J. Leist, A. K. Geim, K. S. Novoselov, L. A. Ponomarenko. Field-effect tunneling transistor based on vertical graphene heterostructures. *Science* **335 (6071)**, 947–950 (2012).

[122] L. Britnell, R. V. Gorbachev, A. K. Geim, L. A. Ponomarenko, A. Mishchenko, M. T. Greenaway, T. M. Fromhold, K. S. Novoselov, L. Eaves. Resonant tunnelling and negative differential conductance in graphene transistors. *Nat. Commun.* **4**, 1794 (2013).

[123] M. Bernardi, M. Palummo, J. C. Grossman. Extraordinary sunlight absorption and one nanometer thick photovoltaics using two-dimensional monolayer materials. *Nano Lett.* **13 (8)**, 3664–3670 (2013).

[124] L. Britnell, R. M. Ribeiro, A. Eckmann, R. Jalil, B. D. Belle, A. Mishchenko, Y.-J. Kim, R. V. Gorbachev, T. Georgiou, S. V. Morozov, A. N. Grigorenko, A. K. Geim, C. Casiraghi, A. H. Castro Neto, K. S. Novoselov. Strong

light-matter interactions in heterostructures of atomically thin films. *Science* **340 (6138)**, 1311–1314 (2013).

[125] F. Withers, O. Del Pozo-Zamudio, A. Mishchenko, A. P. Rooney, A. Gholinia, K. Watanabe, T. Taniguchi, S. J. Haigh, A. K. Geim, A. I. Tartakovskii, K. S. Novoselov. Light-emitting diodes by band-structure engineering in van der Waals heterostructures. *Nat. Mater.* **14**, 301–306 (2015).

[126] J. Kang, S. Tongay, J. Zhou, J. Li, J. Wu. Band offsets and heterostructures of two-dimensional semiconductors. *Appl. Phys. Lett.* **102 (1)**, 012111 (2013).

[127] C. Gong, H. Zhang, W. Wang, L. Colombo, R. M. Wallace, K. Cho. Band alignment of two-dimensional transition metal dichalcogenides: application in tunnel field effect transistors. *Appl. Phys. Lett.* **103 (5)**, 053513 (2013).

[128] X. Hong, J. Kim, S.-F. Shi, Yu Zhang, C. Jin, Y. Sun, S. Tongay, J. Wu, Y. Zhang, F. Wang. Ultrafast charge transfer in atomically thin MoS_2/WS_2 heterostructures. *Nat. Nanotechnol.* **9**, 682–686 (2014).

[129] F. Ceballos, M. Z. Bellus, H.-Y. Chiu, H. Zhao. Ultrafast charge separation and indirect exciton formation in a MoS_2–$MoSe_2$ van der Waals heterostructure. *ACS Nano* **8 (12)**, 12717–12724 (2014).

[130] H. Heo, J. H. Sung, S. Cha, B.-G. Jang, J.-Y. Kim, G. Jin, D. Lee, J.-H. Ahn, M.-J. Lee, J. H. Shim, H. Choi, M.-H. Jo. Interlayer orientation-dependent light absorption and emission in monolayer semiconductor stacks. *Nat. Commun.* **6**, 7372 (2015).

[131] J. P. Perdew, K. Burke, M. Ernzerhof. Generalized gradient approximation made simple. *Phys. Rev. Lett.* **77 (18)**, 3865 (1996).

[132] S. Adachi. *Properties of semiconductor alloys: group-IV, III-V and II-VI semiconductors* (John Wiley & Sons, Inc., Chichester, UK, 2009). ISBN: 9780470744383.

[133] A. F. Rigosi, H. M. Hill, K. T. Rim, G. W. Flynn, T. F. Heinz. Electronic band gaps and exciton binding energies in monolayer $Mo_xW_{1-x}S_2$ transition metal dichalcogenide alloys probed by scanning tunneling and optical spectroscopy. *Phys. Rev. B* **94 (7)**, 075440 (2016).

[134] R. Frisenda, E. Navarro-Moratalla, P. Gant, D. Pérez De Lara, P. Jarillo-Herrero, R. V. Gorbachev, A. Castellanos-Gomez. Recent progress in the assembly of nanodevices and van der Waals heterostructures by deterministic placement of 2D materials. *Chem. Soc. Rev.* **47 (1)**, 53–68 (2018).

[135] Y. Gong, J. Lin, X. Wang, G. Shi, S. Lei, Z. Lin, X. Zou, G. Ye, R. Vajtai, B. I. Yakobson, H. Terrones, M. Terrones, B. K. Tay, J. Lou, S. T. Pantelides, Z. Liu, W. Zhou, P. M. Ajayan. Vertical and in-plane heterostructures from WS_2/MoS_2 monolayers. *Nat. Mater.* **13**, 1135–1142 (2014).

[136] Y. Gong, S. Lei, G. Ye, B. Li, Y. He, K. Keyshar, X. Zhang, Q. Wang, J. Lou, Z. Liu, R. Vajtai, W. Zhou, P. M. Ajayan. Two-step growth of two-dimensional WSe_2/$MoSe_2$ heterostructures. *Nano Lett.* **15 (9)**, 6135–6141 (2015).

Chapter 2

Experimental techniques

2.1 Sample fabrication methods

As discussed in chapter 1, optical and electronic properties of transition metal dichalcogenides (TMDCs) are significantly changed when it is thinned down from bulk to a monolayer. All samples used in our experiments are produced from bulk materials by micromechanical cleavage (exfoliation) and peel/lift transfer. Additionally, some samples are encapsulated (to protect them from environmental contamination and/or thermal cycling) and electrically contacted (to apply voltage for modifications of optoelectronic properties). Fabrication techniques will be described in detail in this section.

2.1.1 Mechanical exfoliation

Nowadays, mechanical exfoliation (also known as the 'Scotch-tape' method) is still the most common fabrication method to produce high-quality two-dimensional (2D) materials and devices consisting of one or few atomic layers. It was used for the first time by Novoselov *et al.* in 2004 to measure the electric field effect in atomically thin carbon films called graphene [1]. This procedure is technologically very simple (schematically shown in Fig. 2.1), but currently produces monolayers with a better quality than, for example, the chemical vapour deposition (CVD) method [2, 3]. An

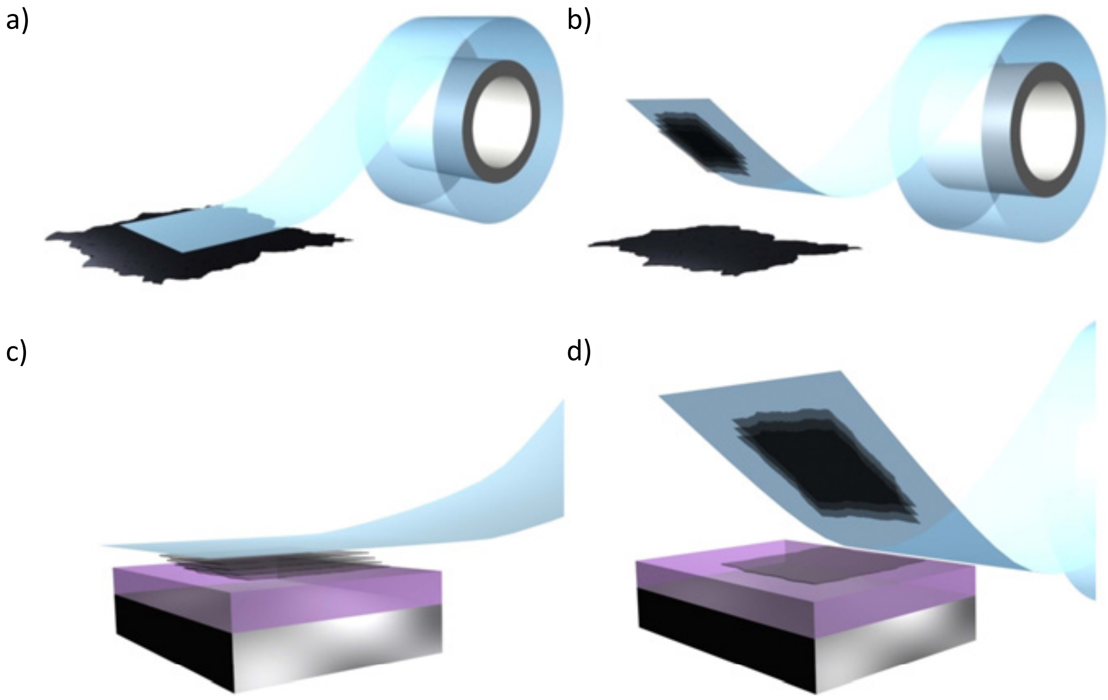

Fig. 2.1 The schematic representation of mechanical exfoliation. Reproduced from [6]. (a) An adhesive tape is pressed against a crystal and (b) peeled off with attached flakes. (c) Then, the tape is pressed against a surface of choice (for example, the SiO_2/Si substrate). (d) Upon peeling off, the thin films of the material remain on the substrate due to stronger van der Waals interaction with the substrate than the interlayer bonding of layered materials.

adhesive tape used for mechanical exfoliation is similar to the wafer dicing tape which protects the surface of a semiconductor wafer when a micrometer saw cuts the wafer. Such tape does not leave significant glue residues on substrates and consequently is ideal for the exfoliation process. First, the sticky tape is pressed against a bulk piece of the material (Fig. 2.1a) so that the top few layers are stuck to the tape (Fig. 2.1b) because of the weak van der Waals forces of the crystal lattice. To thin down pieces of the material attached to the tape, another strip of the tape could be applied for peeling off. Thinner flakes are created with every iteration of this process. Eventually, the tape with thin flakes is pressed again against a substrate (Fig. 2.1c). When the tape is peeled off, some layers of the material remain on the substrate (Fig. 2.1d), because the van der Waals attraction to the substrate is stronger than the interlayer bonding in graphite and TMDCs [4, 5].

The described exfoliation technique produces monolayer sheets, but it has several

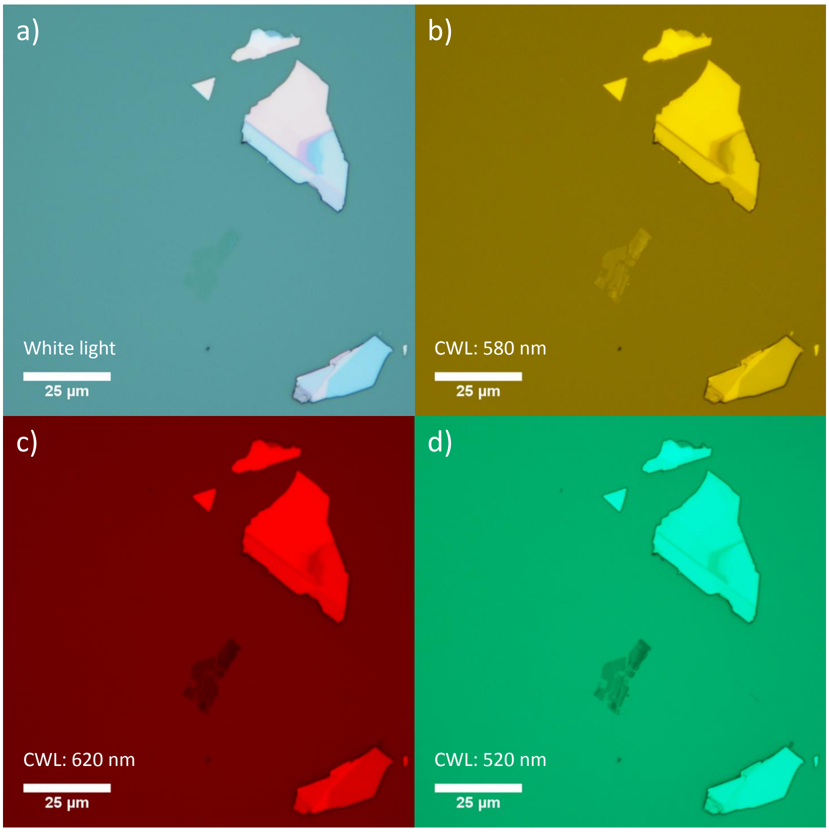

Fig. 2.2 The visibility of the TMDC nanolayers in the microscope images. (a) The presented micrograph contains hardly visible WSe_2 monolayer sheets (center of the image) and thicker flakes on a polymer substrate. Terraces with different number of atomic layers are distinguished by colour. The scale bar is 25 μm. (b)–(d) The same pictures but with the use of different bandpass filters. The central wavelengths (CWL) of these filters are denoted. Bandpass regions: 10–15 nm.

disadvantages. There is no guarantee to obtain single layers. Moreover, multiple films with a variety of thicknesses are left on the substrate. Every additional peeling off could make the exfoliated flakes thinner but potentially decrease their lateral dimensions. Apart from that, some crystals start to have more terraces with different thicknesses. Hence, it is better to apply only once the tape with flakes on the target substrate.

Dimensions of monolayers formed during the exfoliation procedure vary and could be from few microns up to a millimetre in the case of graphene [7] and tens to hundreds of micrometers for the hexagonal boron nitride (hBN) and TMDCs [8]. The lateral sizes of the cleaved layers depend not only on the fabrication technique but on the natural roughness of the substrate surface and the quality of the layered material itself. Also, it is easier to achieve bigger TMDC monolayer or graphene sheets on polymers (for instance, polypropylene carbonate (PPC)) or hBN, which have an atomically smooth surface without dangling bonds and surface charge traps, rather than on SiO_2 [9].

Exfoliated flakes usually consist of terraces with different thicknesses, showing differing contrast colour in the images taken with an optical microscope (Fig. 2.2a). Nevertheless, it is difficult to see peel-off single atomic layers on many substrates. To make thin flakes more visible, narrow bandpass filters are often employed to facilitate the imaging process. In this case due to the interference effects, the contrast of monolayers can be increased as demonstrated in Fig. 2.2b–d. For the SiO_2/Si substrates, the initial white light image contrast of the TMDC and graphene sheets is the highest when the thickness of the silicon dioxide layer is about either 70–100 nm or 270–300 nm [10–13]. For the reliable determination of the number of atomic layers contained in exfoliated crystals, the atomic force microscopy (AFM) measurements are performed. In addition, Raman spectroscopy is sensitive to the film thickness [14–16]. Other alternative and powerful option is the photoluminescence imaging [17] developed in the University of Sheffield and described in detail below in subsubsection 2.2.1.5.

2.1.2 Transfer of ultrathin films onto arbitrary substrates

In the previous subsection, it is mentioned that the substrate surface influences the quality and observation of exfoliated material layers. Transfer of cleaved thin films from one substrate (mostly polymer) to another is frequently used in fabrication particularly for heterostructure samples. Here, we consider the transfer methods necessary to produce the layered structures investigated in our experiments.

2.1.2.1 PMMA-based transfer

One of the most typical transfer techniques includes the use of a hydrophobic polymer polymethyl methacrylate (PMMA) and a water-soluble polymer layer, mostly polymethylglutarimide (PMGI). A similar procedure is outlined in [9]. The

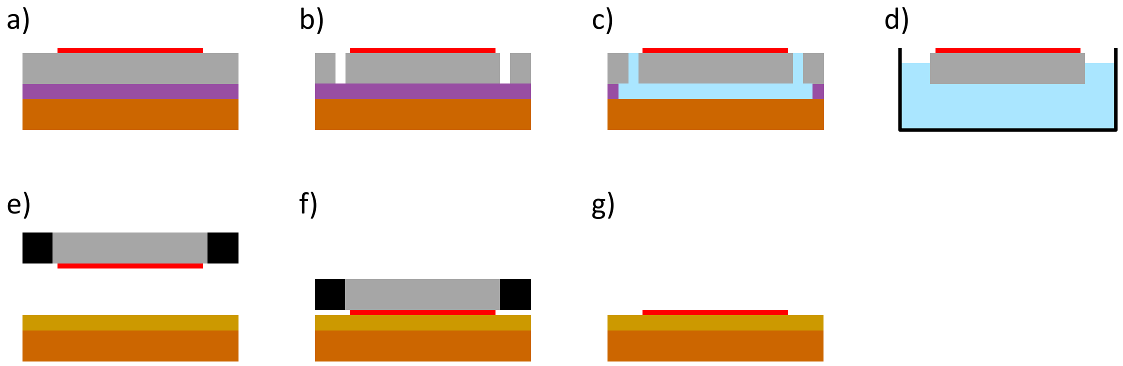

Fig. 2.3 The schematic illustration of the tranfer procedure using the polymer PMMA/PMGI structure. (a) The ultrathin sheets (red) are exfoliated on top of the silicon substrate (brown) which is coated with two polymers: PMGI (purple) and PMMA (grey). (b) The PMMA membrane is scratched with a dental pick or a sharp pair of tweezers around the contour of the best flake. (c) Dissolving the PMGI layer underneath with a developer. (d) When the PMGI is completely dissolved, the membrane with the thin film free floats and (e) is caught by a metal washer (black). (f) The flipped down washer with the captured flake is put onto the target substrate (for example, the SiO_2 (dark yellow)/Si (brown)). Then, the substrate is heated to 65–70 °C. (g) The polymer membrane is removed with either slow peeling off or washing off by means of acetone.

first step is the substrate preparation: a common silicon substrate is spin coated with the PMGI, baked to eliminate the solvent residues and then again spin coated with the PMMA. When all polymers are deposited, the flakes of layered material are exfoliated by a Scotch tape onto the prepared substrate and searched with an optical microscope equipped with the above-mentioned bandpass filters if necessary (subsection 2.1.1). Next, an area around the desired flake is scored using a sharp-edged tool. Some etchant (MF26A or MF319) is added into the formed scratches to dissolve the PMGI film. The PMMA membrane and selected flake on top start to float and are fished out onto a metallic sample holder. The latter is inverted and brought in contact with the target substrate which is further warmed on a hot place to 65–70 °C. This heating increases the flexibility of the remaining PMMA and promotes better adhesion of the transferred sheet to the substrate. Finally, the PMMA film is removed. There are two options: either it is peeled off (in this case, the method is called the ‘dry-peel transfer’) or dissolved in acetone (‘wet transfer’). For the dry-peel transfer, it is important that the cleaved ultrathin film preferentially adheres to the target surface during the detachment of the PMMA.

Thus, the substrate is often covered with other materials, such as hBN. The basic concepts of the PMMA-based transfer technique are depicted in Fig. 2.3. Regardless of the ways of polymer removing, some contamination exists on the flake and could affect its optical properties.

2.1.2.2 PDMS-based transfer

Another effective dry-transfer method relates to the use of polydimethylsiloxane (PDMS) polymer. A detailed description of this process is given in [18] and a schematic is shown in Fig. 2.4.

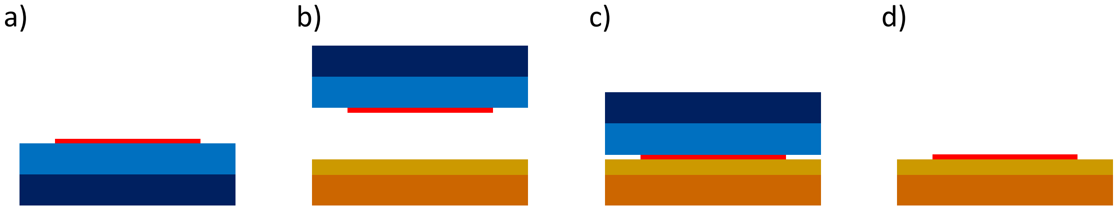

Fig. 2.4 The schematic illustration of the tranfer procedure using the PDMS polymer. (a) The ultrathin sheets (red) are exfoliated on top of the PDMS (blue) deposited onto a microscope glass slide (dark blue). (b) The above stamp is flipped down, aligned with the desired position on the target substrate (for example, the SiO_2 (dark yellow)/ Si (brown)) and (c) brought in contact with the latter. (d) Extremely slow peeling off of the PDMS layer is performed so that the flakes remain on the substrate.

The commercially available PDMS gel (preferably with in-plane dimensions not exceed the length of 1 cm) is put on a glass slide so that no apparent wrinkles or bubbles occur. The thin 2D films peeled off by an adhesive tape are attached to the polymer surface. The formed stamp is aligned and placed face down on the target substrate. A good contact is achieved when the color and visibility of the flakes are changed, which we can identify using an optical microscope. Then, the PDMS has to be very slowly lifted up. At that moment, the viscous properties of the polymer overwhelm its elastic behaviour. As a result, the stamp detaches living the cleaved crystals on the substrate.

On the whole, all dry-transfer approaches have some advantages since the solvent residues can reduce the quality of the flakes after washing off during the wet transfer. Also, it is worth noting that the aforementioned viscoelastic stamping works with almost any substrate independently from its surface roughness. Nonetheless, the disadvantage of the PDMS-based method is that polymer residues still remain on both surfaces of the flake. This provides 'natural' encapsulation of the transferred film, but makes consequent assembly of vertical stacks nearly impossible.

2.1.3 Two-dimensional heterostructures

In our work, the production of the vertically stacked heterostructures (HSs) containing two different TMDC monolayers is a combination of the mechanical exfoliation and PMMA-based transfer techniques. First of all, the bottom TMDC layer of the HS is cleaved on a SiO_2/Si substrate spin coated with PPC polymer. The top TMDC layer of the HS is placed on a PMMA/PMGI/Si and then transferred to the bottom film as described in subsubsection 2.1.2.1 except for the last step (Fig. 2.3a–f). When the substrate is heated to 65–70 ℃, the PMMA membrane is slowly peeled back up lifting the whole heterobilayer off the PPC. Next, the HS is put in contact with either a blank SiO_2/Si or hBN layer preliminary exfoliated on the SiO_2/Si substrate. Ultimately, the PMMA is either detached or washed off with acetone. In the case of the gated samples, this PMMA layer is used as a resist to pattern electrodes by means of e-beam lithography. For encapsulation, we wet transfer an hBN crystal on top of the HSs. An electron-beam evaporation of 20 nm HfO_2 in the main completes the fabrication procedure for the capped samples.

2.1.4 Electron-beam lithography

In order to create electric contacts on our samples, electron-beam (or e-beam) lithography [19] has been applied. We choose the PMMA as a positive polymeric resist whose long molecule chains are destroyed by the beam of electrons [20].

Before making the patterns by this method, the PMMA layer must be on top of the fabricated structure. This can be either the membrane which remains from the previous fabrication steps or new spin-coated layer. A methyl isobutyl ketone (MIBK)/isopropyl alcohol (IPA) 1:5 solution is prepared to develop the PMMA [21]. The development changes the solubility in the exposed PMMA areas owing to the

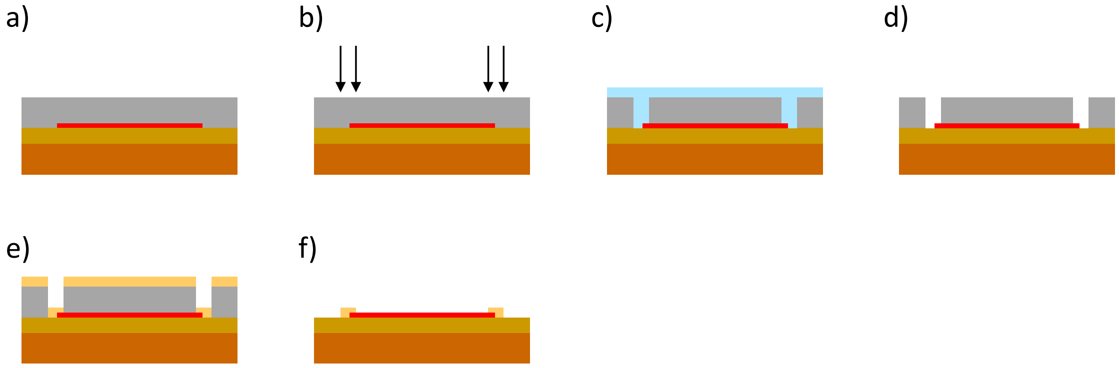

Fig. 2.5 The schematic drawing of the PMMA-based electron-beam lithography. (a) Capping with the PMMA layer (grey) a produced structure (red) on a substrate (for example, the SiO_2 (dark yellow)/Si (brown)). (b) All electrodes are patterned via the e-beam exposure (black arrows). (c)–(d) Dissolving the exposed regions of the resist with a developer. (e) An electron-beam evaporation of Cr/Au (yellow). (f) A lift-off process removes the remaining PMMA and keeps the formed metallic contacts on the sample.

molecular weight reduction [20]. After etching, 5 nm Cr and 50 nm Au is e-beam evaporated to form the contacts. The excess resist covered with the Cr/Au is dissolved in acetone. The last process is called the lift-off. The main steps of the e-beam lithography procedure are illustrated in Fig. 2.5.

2.2 Optical techniques

This section details the experimental methods used in our optical experiments.

2.2.1 Photoluminescence

Photoluminescence (PL) describes emission of light in the material following absorption of light from an external source. Since we only investigate the semiconducting TMDCs, the explanation of the PL mechanisms will be considered for inorganic semiconductors.

2.2.1.1 Photoluminescence in semiconductors

To begin with, we will review the relevant relaxation and recombination mechanisms occurring in semiconductor materials. The sketch in Fig. 2.6a depicts these

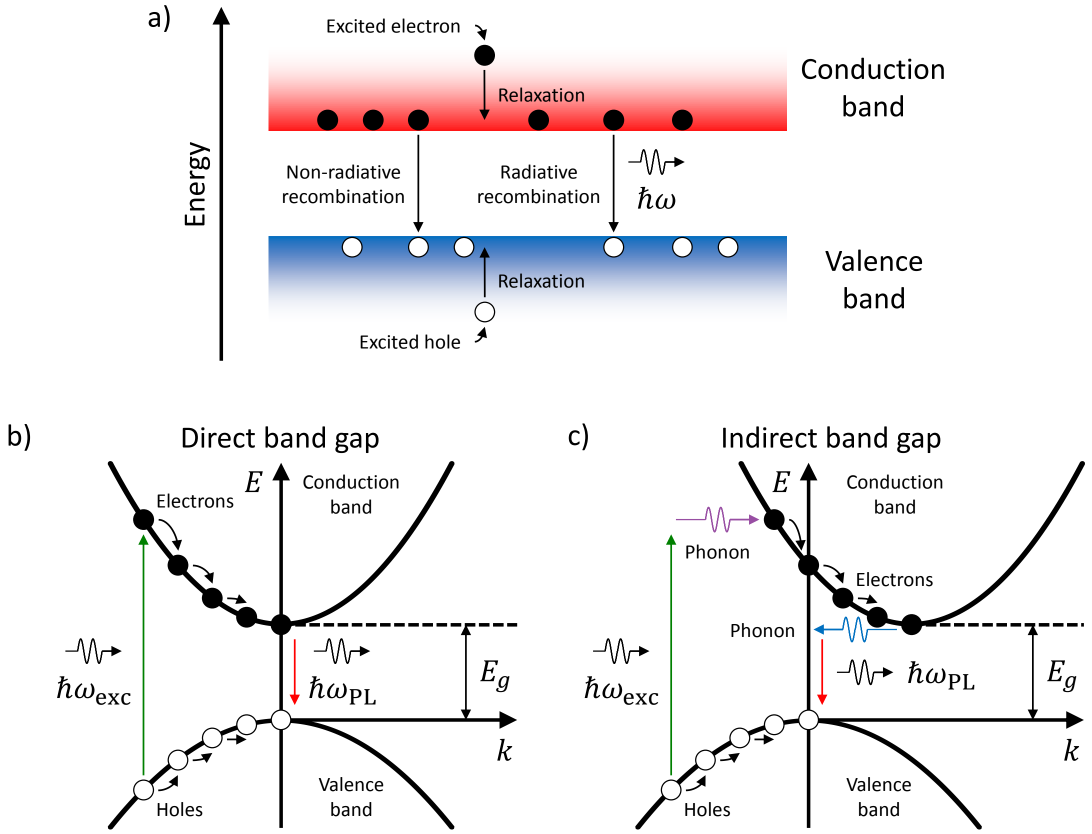

Fig. 2.6 The schematic of the relaxation and recombination processes in semiconductors. This cartoon neglects the excitonic effects that are robust in the TMDC monolayers. (a) The basic concepts of the relaxation and recombination phenomena. Charge carriers can radiatively and non-radiatively recombine. $\hbar\omega$ denotes an energy of an emitted photon. Energy axis has vertical direction. One of the real-space dimensions is horizontally directed. (b)–(c) The PL of the direct- and indirect-bandgap structures, respectively (E the energy, k the wave vector). $\hbar\omega_{\mathrm{exc}}$, $\hbar\omega_{\mathrm{PL}}$ and E_g correspond to the energies of absorbed and emitted photons as well the as band gap. Photoexcited electrons and holes move down to lower energy level because of relaxation. In the case of the indirect band gap, phonons (blue and purple wave arrows) participate in all optical transitions.

phenomena. Electrons are promoted into the conduction band via absorption of photons of high energy. The Coulomb scattering and interaction with phonons cause the energy losses of the electrons and this process is called relaxation. The charge carriers relax towards the band edges very quickly and the following electron-hole recombination usually arises around the band-gap energy. Before this in the 2D TMDCs due to large excitonic effects [22], bound electron-hole pairs (excitons) are formed. Their binding energies exceed 100 meV [22], resulting in a strong exciton PL (radiative recombination) even at room temperature [23]. More complicated kinds of non-radiative recombination also have to be taken into account, as the quantum yield, which is the ratio of the emitted to absorbed photons, is ordinarily below 1 % in those structures [23].

Such optically excited light emission is typical for the semiconductors with the direct band gap when the conduction band minimum (CBM) and valence band maximum (VBM) are located at the same point of the Brillouin zone (Fig. 2.6b). Fig. 2.6c demonstrates another mechanism of the PL creation. In the indirect-bandgap materials, there is a difference Δk between the CBM and VBM in momentum space. To compensate that shift, phonons must be involved in the procedure. This condition significantly lowers the light emission efficiency as the optical transitions in the indirect-gap semiconductors are second-order processes with relatively low PL probability [24]. Consequently, most of the photoexcited charge carriers undergo non-radiative recombination in such materials.

In the TMDCs, the presence of disorder potential and various defects leads to an inhomogeneous broadening of the detected PL spectrum. Such inhomogeneity is mainly the dominating factor particularly at low temperatures and often conceals the intrinsic homogeneous linewidth. Therefore, interpretation of the observed peak widths should be carried out with especial care.

2.2.1.2 Polarization-resolved photoluminescence

Some of our experiments are carried out using polarization-resolved PL. In these measurements, both the excitation and PL detection are conducted in a specific polarization basis.

Polarization specifies the geometrical orientation of oscillations of the transverse waves. For an electromagnetic wave (light) consisting of the coupled oscillating orthogonal electric E and magnetic B fields, it deals with the direction of the electric field by convention. A multitude of randomly oriented atomic emitters form a source of ordinary (natural) light which is randomly polarized or unpolarized. When the resultant electric field of electromagnetic waves oscillates in a single direction along the direction of propagation, the polarization is called linear. Circularly or elliptically polarized light contains the E-vector rotating at a constant rate in any fixed plane perpendicular to the wave motion. The tip of that electric field vector describes a circle or ellipse. Its clockwise (anticlockwise) rotation with the fixed amplitude as seen by an observer looking toward the source refers to right (left) circular polarization [25].

Polarization-resolved PL measurements are useful for the systems where inversion symmetry of the crystal lattice unit cell is broken (for instance, monolayer TMDCs). Inversion asymmetry determines contrasted circular dichroism in different k-space regions so that optical selection rules for interband transitions at high symmetry points are observed [26]. In the single-layer TMDCs, such as MoS_2, WS_2, $MoSe_2$ and WSe_2, the light absorption as well as emission near the K $(-K)$ valleys of the Brillouin zone are only allowed with right (left) circularly polarized light [27–30]. Hence, the study of the PL polarization properties in these materials could provide important information about the electronic band structure and light-matter interactions.

The degree of polarization ρ is used for quantitative description of the polarized emission. In accordance with [26, 28, 29, 31], we express this parameter (in percent) as

$$\rho = \frac{I_{co} - I_{cross}}{I_{co} + I_{cross}} \cdot 100\,\%, \tag{2.1}$$

where I_{co} and I_{cross} are the integrated intensities of the detected spectral signal in two senses of polarization: either right and left circular, or horizontally and vertically linear, respectively (usually co- and cross-polarized with respect to the excitation).

During the polarization-resolved PL experiments, we operate with optical elements, specifically linear polarizers and retarders, namely half- and quarter-waveplates, aimed to create and analyse the polarized light. The set-up used by us for the detection of the polarized signal is described in the next subsubsection (Fig. 2.7) and section 5.2.

2.2.1.3 Photoluminescence measurements

We perform all experiments on the set-up which is schematically depicted in Fig. 2.7.

This set-up consists of two parts: micro-photoluminescence (μPL) and micro-reflectance contrast (μRC). The μPL technique is used in order to measure PL with micron spatial resolution.

In most cases, the excitation light beam is produced by 532 nm, 660 nm or 730 nm continuous-wave (CW) laser diodes filtered by a corresponding bandpass filter to remove undesirable spectral tails. The photoluminescence excitation regime is operated with another tunable laser as presented in subsubsection 2.2.1.4. To achieve a homogeneous distribution in the beam profile, light is coupled through an optical single-mode (SM) fiber designed for an appropriate wavelength range (mostly Thorlabs P3-460B-FC-5 or P3-630A-FC-5). A corresponding shortpass filter eliminates residual spectral artifacts of the laser excitation passing through the SM fiber.

The linear polarizers and wave plates are mounted in the set-up during the polarization-resolved PL measurements. A detailed information on what the light polarization is and how those optical elements work is described in the previous subsubsection and section 5.2.

A special white light source with a multi-mode fiber, an optical system consisting of achromatic doublets and a precision pinhole, a near complementary metal–oxide–semiconductor (CMOS) camera are used in the reflectance contrast experiments discussed in detail in subsection 2.2.2.

A 1 inch 50:50 non-polarizing cube beam splitter (Thorlabs CM1-BS2) divides the laser beam into two beams of equal light intensity: one of them goes to a Si power meter (Thorlabs PM100D) and the other to a 50 × microscope objective (Mitutoyo M Plan Apo 50 ×) with a 13 mm working distance and a numerical aperture (NA) of 0.55. Behind the objective, the latter beam is focused onto a target sample in a spot of $\sim 2\ \mu$m diameter within the 1–100 μW power range.

To visualize the sample, manipulate the spatial profile and position of the laser spot, a 1.3 megapixel colour CMOS camera (Thorlabs DCC1645C) and white light source are included in the set-up.

Light emitted by the sample is collected with the 50 × objective, goes through a

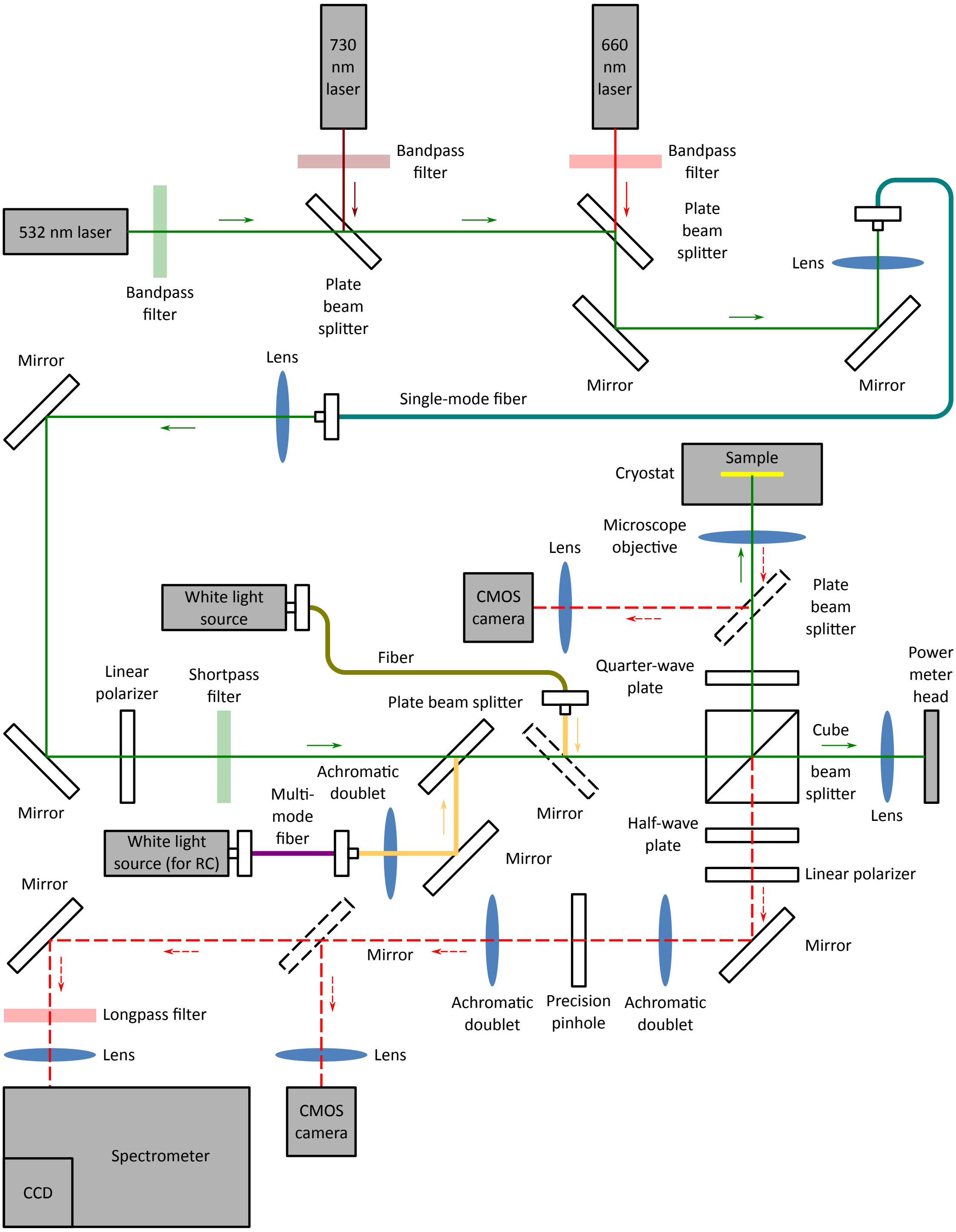

Fig. 2.7 The sketch of the experimental set-up used in the PL measurements with the continuous-wave laser excitation as well as in the reflectance contrast measurements. The arrows near the laser beam (green, red and maroon solid lines), white light beam (yellow solid line) and emitted signal (red dashed line) pathways indicate the direction of the movement. The dashed optical elements denote that they are able to be taken out from the optical path.

longpass filter (to remove laser light partially reflected from the surface of the sample and other optical elements), and is guided to a 50 micron slit of a 0.5 m optical spectrometer (Princeton Instruments SP-2-500i). A liquid nitrogen cooled charge coupled device (CCD) (Princeton Instruments PyLoN:100BR) is used to detect PL. Three diffraction gratings (300 lines/mm, 600 lines/mm and 1200 lines/mm) are provided in the spectrometer to obtain different spectral resolution. The CCD has a chip of 100 pixels × 1240 pixels.

For the low-temperature measurements, the sample is mounted in vacuum on a cold finger of a continuous flow He cryostat (Janis ST-500 or Oxford Instruments Microstat HiRes2). The circulation of liquid helium across the cryostat from a special dewar via a transfer tube allows to cool down the sample to approximately 5–6 K and set controllable temperatures up to ambient conditions by means of a heater. The gated samples are placed and bonded to a sample holder which lies on the cryostat cold finger and is connected via wires to a voltage source (Keithley 2400 or 2450).

The entire cryostat is fixed on heavy duty XYZ stages based on the single-axis Mercury C-663.11 stepper motor controller and Mercury C-863.11 servo controller with Standa 8CMA06-25 motorized actuators and Standa 8MVT40-13-1 motorized vertical translation stage. A travel range of the stages in the horizontal plane is 50 mm × 50 mm with an accuracy of ~ 1 micron. In the vertical direction (focusing), the travel range is 13 mm with 0.1 μm resolution. The translation stages are needed to align various areas of the sample under the excitation spot. When the experiments are conducted at room temperature, the sample is positioned on the stages without the cryostat and thus maintained in ambient conditions.

2.2.1.4 Photoluminescence excitation

In the photoluminescence excitation (PLE) experiments, the excitation laser is tuned and a series of PL spectra are measured. PLE spectroscopy allows to investigate a correlation between the absorption and emission processes. PLE spectra may reveal absorption peaks, but relaxation effects should also be taken into account. This optical method is practical for the study of the excited state structure as well as identification of the origin of various PL spectral features. In certain conditions, the PLE approach could lead to an improved signal-to-noise ratio compared to classical absorption measurements in the transmission geometry.

Some modifications in our set-up shown in Fig. 2.7 are applied in the PLE experimental regime. Instead of the laser diodes with fixed excitation energies, a Ti:sapphire CW laser (M Squared SolsTiS) forms the incident light beam whose wavelength can be varied from 700 nm to 820 nm. An SM fiber (Thorlabs S630-HP-Custom) operating in a 630–860 nm wavelength range is used to transmit laser light and create the homogeneous distribution in the beam profile. Other parts of the μPL set-up remain the same as presented in subsubsection 2.2.1.3.

2.2.1.5 Photoluminescence imaging

For rapid monitoring of the quality of the few layer crystals, we have developed a PL imaging technique based on the use of a bright-field optical microscope. A full description of this method is reported in [17]. Here, we outline the main concepts of the above experimental procedure. A schematic of the PL imaging set-up and examples of PL images are given in Fig. 2.8.

We employ this technique for the signal identification of the TMDC-based structures (single- and few-layer flakes, HSs and alloys). Our commercial bright-field microscope (Nikon LV150N) includes a 550 nm shortpass filter (Thorlabs FESH0550) to leave only short-wavelength components of light in the beam formed by a white light source (Fig. 2.8a). This is necessary for PL excitation in a sample. To isolate the generated PL from the incident light reflected from the sample, microscope objective and beam splitter surfaces, a 600 nm longpass filter (Thorlabs FELH0600) is mounted in the optical detection path. All spectral edgepass filters are installed into slots of an illuminator (Nikon LV-UEPI-N). Such arrangement allows to quickly switch between PL and bright-field imaging regimes. A spatial distribution of the emission taken from the sample results in the PL image captured with a 2.0 megapixel colour microscope camera (Nikon DS-Vi1). Originally, a hot mirror embedded in the camera limits the sensor sensitivity to the visible spectrum. By removing this

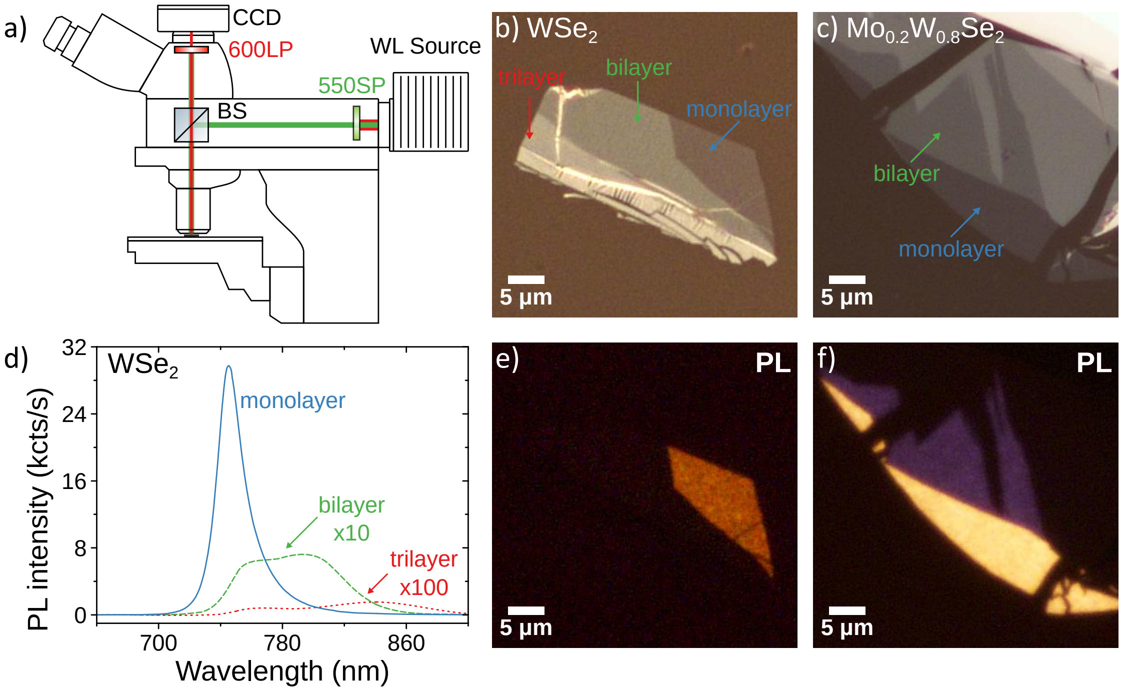

Fig. 2.8 PL imaging of TMDC-containing flakes using a bright-field optical microscope. Reproduced from [17]. (a) The schematic drawing of the PL imaging set-up. The microscope is equipped with a white light source (*WL Source*), 550 nm shortpass (550*SP*) and 600 nm longpass (600*LP*) filters, beam splitter (*BS*) and colour camera with CCD and CMOS sensors (*CCD*). (b)–(c) Bright-field and (e)–(f) corresponding PL micrographs of WSe$_2$ and Mo$_{0.2}$W$_{0.8}$Se$_2$ flakes on PDMS substrates. The scale bars are 5 μm. Each sample has areas with different thicknesses some of which are indicated in (b)–(c). Parameters of the PL images: (e) 1 s acquisition time and 9.6 × analog gain; (f) 1 s acquisition time and 3.4 × analog gain. For the WSe$_2$, PL spectra recorded in the monolayer (blue), bilayer (green), and trilayer (red) regions are illustrated in (d). Data from the few-layers are scaled-up (the magnifications are denoted).

mirror, the PL detection can be extended to the near-infrared range.

Because of the indirect-to-direct band-gap crossover [23], the difference in the PL quantum yield between the monolayer and few-layer (or bulk) TMDCs is noticeable as seen in Fig. 2.8d. In addition, the emission peaks are redshifted when the film thickness is increased. These effects are clearly visible in the PL images through the changes in brightness and colour (Fig. 2.8e–f). Moreover, such micrographs reveal spatial variation of the PL intensity owing to the influence of non-uniform doping, mechanical strain and different structural defects (for instance, folds) existing in the flakes. Overall using this optical method, we can conduct a rapid characterization of fluorescence of the fabricated mono- and few-layer TMDC crystals on various substrates. PL imaging also allows to visually establish a strength of the interlayer coupling in the HSs [17].

2.2.2 Reflectance contrast measurements

Reflectance $\mathcal{R}$ refers to the effectiveness of the surface of a material to reflect electromagnetic radiation. In other words, it is a proportion of power of light reflected at the interface between different optical media to that of incident light. The reflectance as a function of the photon energy $\hbar\omega$ (or wavelength λ) forms the reflectance spectrum. In practice, when we deal with a flake on a substrate, it is better to operate with the reflectance contrast (RC) the spectrum of which, $\mathcal{C}(\hbar\omega)$, can be determined [32] as follows:

$$\mathcal{C}(\hbar\omega) = \frac{\mathcal{R}(\hbar\omega) - \mathcal{R}_0(\hbar\omega)}{\mathcal{R}(\hbar\omega) + \mathcal{R}_0(\hbar\omega)} \cdot 100\,\%, \tag{2.2}$$

$\mathcal{R}(\hbar\omega)$ and $\mathcal{R}_0(\hbar\omega)$ are the reflectance spectra of the flake on the substrate and the substrate itself, respectively. Another definition [33] is

$$\mathcal{C}^*(\hbar\omega) = \frac{\mathcal{R}(\hbar\omega) - \mathcal{R}_0(\hbar\omega)}{\mathcal{R}_0(\hbar\omega)} \cdot 100\,\%. \tag{2.3}$$

Both $\mathcal{C}(\hbar\omega)$ and $\mathcal{C}^*(\hbar\omega)$ are just normalizations of the reflectance spectra and contain the same energy (or wavelength) positions of spectral resonances which appear as maxima or minima depending on the substrate reflectance properties. In our experiments, we formulate the RC as in Eq. (2.2). The $\mathcal{C}^*$ is proportional to the absorption $\mathcal{A}$ [33, 34]:

$$\mathcal{C}^*(\hbar\omega) = \frac{4}{n_0^2 - 1}\mathcal{A}(\hbar\omega), \tag{2.4}$$

n_0 is the substrate refractive index. Therefore, the positions of the resonances in the RC spectra are identical to the corresponding absorption peak positions. RC spectroscopy is useful for the study of the electronic excited states (for example, the band structure of semiconductors). In combination with PL, such approach can also provide information on the Stokes shifts [24], which are the consequence of exciton/carrier relaxation in a disordered material.

For the RC measurements, the μRC part of the set-up depicted in Fig. 2.7 is used. Some additional information about the set-up is presented in subsubsection 2.2.1.3. Broadband radiation in a 360–2600 nm wavelength range from a stabilized tungsten-halogen source (Thorlabs SLS201/M) is coupled through multi-mode (MM) fiber patch cable (Thorlabs M67L02) to decrease the diameter of the light beam. An achromatic doublet (Thorlabs AC254-030-A), which is designed to limit the effects of the chromatic and spherical aberration, collimates the beam. As in the μPL experiments, the same microscope objective focuses the white light on the sample in a $\sim$ 11 micron spot and collects the reflected signal. Sample visualisation on a computer monitor is performed by means of another white light source and CMOS camera near the objective. Positioned in the collection pathway, a 30 μm precision pinhole (Thorlabs P30S) and two achromatic doublets (Thorlabs AC254-050-A) with the aligned common axis form an optical system allowing to spatially cut off the signal focused in the pinhole. To control this procedure, an image on the pinhole is viewed via an additional 1.3 megapixel colour CMOS camera (Thorlabs DCC1645C). As a result, data are gathered from a region of about 8 μm in diameter on the sample surface. Similarly to the PL measurements, the spectrometer including the CCD acquires and analyses the signal. A longpass filter before the 50 micron spectrometer slit is only necessary in the PL experiments and is removed during the RC detection.

Our entire set-up in Fig. 2.7 is built to have fast and easy switching between the PL and RC measuring modes so that the desired emission and reflected light are collected at the same experimental conditions from the same point on the sample.

References

[1] K. S. Novoselov, A. K. Geim, S. V. Morozov, D. Jiang, Y. Zhang, S. V. Dubonos, I. V. Grigorieva, A. A. Firsov. Electric field effect in atomically thin carbon films. *Science* **306 (5696)**, 666–669 (2004).

[2] H. S. Song, S. L. Li, H. Miyazaki, S. Sato, K. Hayashi, A. Yamada, N. Yokoyama, K. Tsukagoshi. Origin of the relatively low transport mobility of graphene grown through chemical vapor deposition. *Sci. Rep.* **2**, 337 (2012).

[3] H. Zhou, W. J. Yu, L. Liu, R. Cheng, Y. Chen, X. Huang, Y. Liu, Y. Wang, Y. Huang, X. Duan. Chemical vapour deposition growth of large single crystals of monolayer and bilayer graphene. *Nat. Commun.* **4**, 2096 (2013).

[4] M. Yi, Z. Shen. A review on mechanical exfoliation for the scalable production of graphene. *J. Mater. Chem. A* **3 (22)**, 11700–11715 (2015).

[5] M. J. Allen, V. C. Tung, R. B. Kaner. Honeycomb carbon: a review of graphene. *Chem. Rev.* **110 (1)**, 132–145 (2010).

[6] K. S. Novoselov, A. H. Castro Neto. Two-dimensional crystals-based heterostructures: materials with tailored properties. *Phys. Scr.* **2012 (T146)**, 014006 (2012).

[7] J. Kim, H. Park, J. B. Hannon, S. W. Bedell, K. Fogel, D. K. Sadana, C. Dimitrakopoulos. Layer-resolved graphene transfer via engineered strain layers. *Science* **342 (6160)**, 833–836 (2013).

[8] A. V. Kretinin, Y. Cao, J. S. Tu, G. L. Yu, R. Jalil, K. S. Novoselov, S. J. Haigh, A. Gholinia, A. Mishchenko, M. Lozada, T. Georgiou, C. R. Woods, F. Withers, P. Blake, G. Eda, A. Wirsig, C. Hucho, K. Watanabe, T. Taniguchi, A. K. Geim, R. V. Gorbachev. Electronic properties of graphene encapsulated with different two-dimensional atomic crystals. *Nano Lett.* **14 (6)**, 3270–3276 (2014).

[9] C. R. Dean, A. F. Young, I. Meric, C. Lee, L. Wang, S. Sorgenfrei, K. Watanabe, T. Taniguchi, P. Kim, K. L. Shepard, J. Hone. Boron nitride substrates for high-quality graphene electronics. *Nat. Nanotechnol.* **5**, 722–726 (2010).

[10] P. Blake, E. W. Hill, A. H. Castro Neto, K. S. Novoselov, D. Jiang, R. Yang, T. J. Booth, A. K. Geim. Making graphene visible. *Appl. Phys. Lett.* **91 (6)**, 063124 (2007).

[11] M. M. Benameur, B. Radisavljevic, J. S. Héron, S. Sahoo, H. Berger, A. Kis. Visibility of dichalcogenide nanolayers. *Nanotechnology* **22 (12)**, 125706 (2011).

[12] Y. Y. Wang, R. X. Gao, Z. H. Ni, H. He, S. P. Guo, H. P. Yang, C. X. Cong, T. Yu. Thickness identification of two-dimensional materials by optical imaging. *Nanotechnology* **23 (49)**, 495713 (2012).

[13] Hai Li, J. Wu, X. Huang, G. Lu, J. Yang, X. Lu, Q. Xiong, H. Zhang. Rapid and reliable thickness identification of two-dimensional nanosheets using optical microscopy. *ACS Nano* **7 (11)**, 10344–10353 (2013).

[14] Hong Li, Q. Zhang, C. C. R. Yap, B. K. Tay, T. H. T. Edwin, A. Olivier, D. Baillargeat. From bulk to monolayer MoS_2: evolution of Raman scattering. *Adv. Funct. Mater.* **22 (7)**, 1385–1390 (2012).

[15] C. Lee, H. Yan, L. E. Brus, T. F. Heinz, J. Hone, S. Ryu. Anomalous lattice vibrations of single- and few-layer MoS_2. *ACS Nano* **4 (5)**, 2695–2700 (2010).

[16] Q. H. Wang, K. Kalantar-Zadeh, A. Kis, J. N. Coleman, M. S. Strano. Electronics and optoelectronics of two-dimensional transition metal dichalcogenides. *Nat. Nanotechnol.* **7**, 699–712 (2012).

[17] E. M. Alexeev, A. Catanzaro, O. V. Skrypka, P. K. Nayak, S. Ahn, S. Pak, J. Lee, J. I. Sohn, K. S. Novoselov, H. S. Shin, A. I. Tartakovskii. Imaging of interlayer coupling in van der Waals heterostructures using a bright-field optical microscope. *Nano Lett.* **17 (9)**, 5342–5349 (2017).

[18] A. Castellanos-Gomez, M. Buscema, R. Molenaar, V. Singh, L. Janssen, H. S. J. van der Zant, G. A. Steele. Deterministic transfer of two-dimensional materials by all-dry viscoelastic stamping. *2D Mater.* **1 (1)**, 011002 (2014).

[19] H. J. Levinson, M. A. McCord, F. Cerrina, R. D. Allen, J. G. Skinner, A. R. Neureuther, M. C. Peckerar, F. K. Perkins, M. J. Rooks. *Handbook of microlithography, micromachining, and microfabrication*, vol. 1: microlithography (SPIE, Bellingham, USA, 1997). ISBN: 9780819423788.

[20] M. Hatzakis. Electron resists for microcircuit and mask production. *J. Electrochem. Soc.* **116 (7)**, 1033–1037 (1969).

[21] S. Yasin, D. G. Hasko, H. Ahmed. Comparison of MIBK/IPA and water/IPA as PMMA developers for electron beam nanolithography. *Microelectron. Eng.* **61-62**, 745–753 (2002).

[22] A. Ramasubramaniam. Large excitonic effects in monolayers of molybdenum and tungsten dichalcogenides. *Phys. Rev. B* **86 (11)**, 115409 (2012).

[23] K. F. Mak, C. Lee, J. Hone, J. Shan, T. F. Heinz. Atomically thin MoS_2: a new direct-gap semiconductor. *Phys. Rev. Lett.* **105 (13)**, 136805 (2010).

[24] M. Fox. *Optical properties of solids* (Oxford University Press, Oxford, UK, 2001). ISBN: 9780198506133.

[25] E. Hecht. *Optics* (Pearson Education Ltd, London, UK, 2016), 5th edn. ISBN: 9781292096933.

[26] W. Yao, D. Xiao, Q. Niu. Valley-dependent optoelectronics from inversion symmetry breaking. *Phys. Rev. B* **77 (23)**, 235406 (2008).

[27] D. Xiao, G.-B. Liu, W. Feng, X. Xu, W. Yao. Coupled spin and valley physics in monolayers of MoS_2 and other group-VI dichalcogenides. *Phys. Rev. Lett.* **108 (19)**, 196802 (2012).

[28] T. Cao, G. Wang, W. Han, H. Ye, C. Zhu, J. Shi, Q. Niu, P. Tan, E. Wang, B. Liu, J. Feng. Valley-selective circular dichroism of monolayer molybdenum disulphide. *Nat. Commun.* **3**, 887 (2012).

[29] K. F. Mak, K. He, J. Shan, T. F. Heinz. Control of valley polarization in monolayer MoS_2 by optical helicity. *Nat. Nanotechnol.* **7**, 494–498 (2012).

[30] X. Xu, W. Yao, D. Xiao, T. F. Heinz. Spin and pseudospins in layered transition metal dichalcogenides. *Nat. Phys.* **10**, 343–350 (2014).

[31] A. Al-Qasimi, O. Korotkova, D. James, E. Wolf. Definitions of the degree of polarization of a light beam. *Opt. Lett.* **32 (9)**, 1015–1016 (2007).

[32] A. Arora, M. Koperski, K. Nogajewski, J. Marcus, C. Faugeras, M. Potemski. Excitonic resonances in thin films of WSe_2: from monolayer to bulk material. *Nanoscale* **7 (23)**, 10421–10429 (2015).

[33] K. F. Mak, M. Y. Sfeir, Y. Wu, C. H. Lui, J. A. Misewich, T. F. Heinz. Measurement of the optical conductivity of graphene. *Phys. Rev. Lett.* **101 (19)**, 196405 (2008).

[34] A. F. Rigosi, H. M. Hill, K. T. Rim, G. W. Flynn, T. F. Heinz. Electronic band gaps and exciton binding energies in monolayer $Mo_xW_{1-x}S_2$ transition metal dichalcogenide alloys probed by scanning tunneling and optical spectroscopy. *Phys. Rev. B* **94 (7)**, 075440 (2016).

Chapter 3

Photoluminescence and optical reflectance contrast measurements of $Mo_xW_{1-x}S_2$ transition metal dichalcogenide alloys

3.1 Introduction

The atomically thin semiconducting group-VI transition metal dichalcogenides (TMDCs), specifically MoS_2, $MoSe_2$, WS_2 and WSe_2, possess a multitude of unique optical properties described in detail in section 1.2. Alloying of one TMDC material with another may allow to tune the above characteristics more precisely because of modifications in the electronic structure. In this chapter, we focus on a photoluminescence (PL) and reflectance contrast (RC) study of the $Mo_xW_{1-x}S_2$ family of alloys with mono-, bi- and trilayer thicknesses at room temperature.

Changes of the band structure in the ternary monolayers relative to the binary ones are schematically demonstrated in Fig. 3.1a which is taken and altered from [1]. Similarly to single-layer MoS_2 and WS_2 [2–4], the valence-band maximum and conduction-band minimum in the $Mo_xW_{1-x}S_2$ atomic sheets are located at

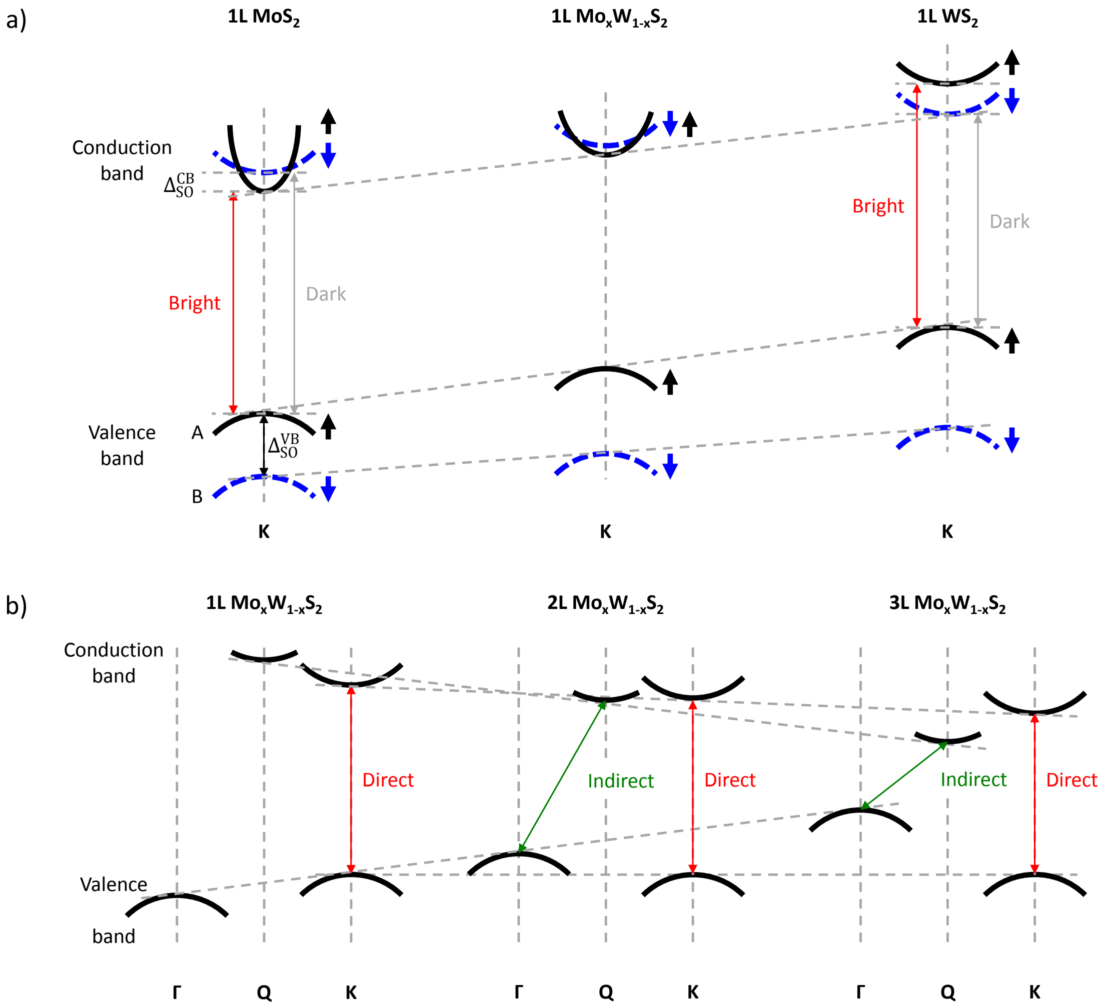

Fig. 3.1 The schematic representation of changes in the electronic band structure of the $Mo_xW_{1-x}S_2$ alloys with the alloy concentration and number of the atomic layers. (a) Transformation of the band structure (near the $+K$ point of the Brillouin zone), namely, valence (Δ_{SO}^{VB}) and conduction band spin splittings (Δ_{SO}^{CB}), band offsets, when going from MoS_2 to WS_2 monolayers. Red and grey arrows denote optically bright and dark A exciton transitions, respectively, without taking into account corresponding exciton binding energies. The edges of A and B exciton transitions in the valence band are indicated as A and B. Spin-up (black) and spin-down (blue) branches of the spin-split conduction and valence bands are also depicted. (b) The influence of the number of layers on the band structure of the $Mo_xW_{1-x}S_2$ along the Γ–K direction of the Brillouin zone (Γ, Q, K are points from that direction). The optically bright direct (red) and indirect (green) in momentum space transitions are indicated. The valence-band maximum is set as a zero level. $1L$, $2L$, $3L$ denote 1, 2, 3 layers. Figure is motivated from [1].

the K points of the two-dimensional (2D) hexagonal Brillouin zone. Thus, these ultrathin crystals have a direct band gap in the momentum space. Another feature of the 2D semiconducting TMDCs is the giant spin-orbit coupling (SOC) in the valence band [2, 5, 6], resulting in the occurrence of A and B excitons [2, 5, 7], which are associated with the direct-gap optical transitions between the band edges. Similar SOC is observed in the alloys with a value between those of two binary compounds. It is worth noting that the valence band splitting is also typical for the bulk TMDCs [8–10] due to the combination of the interlayer interaction and SOC effect [10]. Owing to the presence of the small conduction-band spin-orbit splitting [10–14], the transitions of optically bright and dark excitons (electron-hole complexes built with the particles with the same and opposite spin orientations, respectively) have different energy values in the 2D MoS_2 and WS_2. Additionally, the spin-split conduction bands modifies from crossed to parallel [15], when going from the MoS_2 to WS_2 monolayers. Relative to the vacuum level, the band edges of the single-layer MoS_2 and WS_2 are positioned at different energy levels [16]. The corresponding band edges of the alloys are gradually shifted between those of the binary compounds, following the changes in the alloy composition.

In the few-layer and bulk TMDC semiconductors, the band gap becomes to be indirect [2, 4]: its extrema are located at the Γ point in the valence and at the Q point [11, 17] (in other references either the T [18], Y [19], Σ [20] or Λ [21–23] point) along the Γ–K direction in the conduction band. The strong interlayer coupling effect influences the atomic orbitals so that the energy gap decreases with the increase in the number of the atomic layers [5]. We suggest that the few-layer $Mo_xW_{1-x}S_2$ alloys are affected by the same band structure modifications as shown in Fig. 3.1b, since these ternary materials completely consist of the TMDC compounds. Our spectral results reported in section 3.3 confirm this hypothesis.

The previous room-temperature PL [24, 25] and RC [26] investigations have been carried out to understand the composition-dependent electronic structures of the monolayer semiconducting TMDC-based alloys. Apart from these experimental methods and conditions, Raman [1, 24, 25, 27–30], scanning tunneling [26] and temperature-dependent PL [1, 30] spectroscopies are employed for the similar study of the above 2D materials. However, a detailed analysis of the band structure changes via the variation of both component concentration and material thickness in the TMDC-containing alloys has been necessary until now. This analysis opens the way for the use of such crystals in devices where the electronic structure will be tailored for the required device functionality. Therefore, we have conducted the relevant measurements the most important results of which are discussed here.

3.2 Samples and experimental methods

The studied mono-, bi- and trilayer $Mo_xW_{1-x}S_2$ flakes are produced with mechanical exfoliation (given in subsection 2.1.1) followed by polydimethilsiloxane (PDMS) dry transfer. Subsubsection 2.1.2.2 presents a description of this transfer method. The binary and ternary bulk crystals are delivered from a commercial supplier (HQ Graphene). The substrates of the samples are regular 90–100 nm SiO_2/Si, but the bi- and trilayer WS_2 and $Mo_{0.3}W_{0.7}S_2$ alloys have been deposited on high-quality 100 nm SiO_2/Si. The slight signal differences detected only in the RC spectral shape will be considered in subsection 3.3.4.

The preliminary optical characterization of the cleaved $Mo_xW_{1-x}S_2$ films is performed by PL imaging with the use of a bright-field optical microscope. This approach is described in detail in subsubsection 2.2.1.5 and [31]. The microscope and PL images of the samples of the $Mo_{0.1}W_{0.9}S_2$, $Mo_{0.4}W_{0.6}S_2$ and $Mo_{0.7}W_{0.3}S_2$ alloys are demonstrated as examples in Fig. 3.2. As seen in the micrographs, the monolayer areas of the different alloys emit PL signals with noticeably different colour. Especially strong changes in colour are observed for the ternary monolayers with the small Mo concentration. This indicates that the wavelength of the emission depends on the alloy composition. Another important conclusion obtained from the PL images is that the PL intensity quenches with the increase in the Mo content in the alloys.

All measurements with the single- and few-layer $Mo_xW_{1-x}S_2$ are carried out at

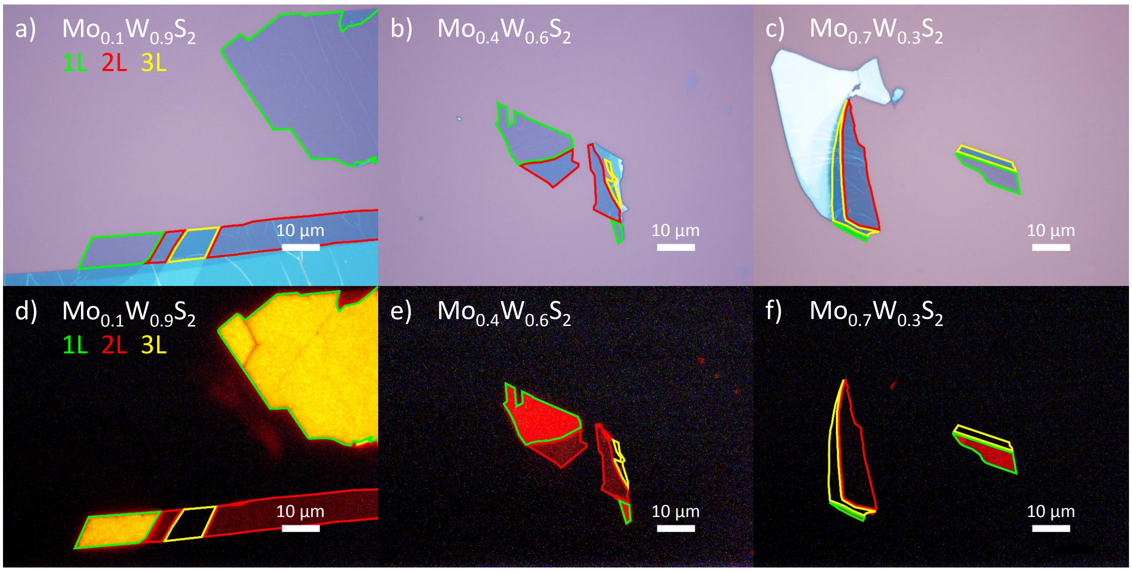

Fig. 3.2 (a)–(c) Bright-field microscope and (d)–(f) PL images of three samples as examples (with 10, 40 and 70 % Mo content). Depicted green, red and yellow lines border the edges of the alloy mono- (1L), bi- (2L) and trilayers (3L), respectively. The scale bars on the images correspond to 10 μm. Parameters of the bright-field images: 100 × magnification, 100 % light power, 1 ms acquisition time and 1 × analog gain. Parameters of the PL images: 100 × magnification, 100 % light power, 10 s acquisition time and 9.6 × analog gain.

room temperature using the micro-photoluminescence (μPL) and micro-reflectance contrast (μRC) techniques. More information on these methods is given in section 2.2.

3.3 Results

3.3.1 Photoluminescence from monolayer $Mo_xW_{1-x}S_2$ alloys

Fig. 3.3 and Fig. 3.4 show data from the monolayer $Mo_xW_{1-x}S_2$ alloys. Normalized PL spectra from single-layer alloys with different Mo concentrations are depicted in Fig. 3.3a. The peak position redshift with the increasing Mo content is observed. Each spectrum consists of two pronounced peaks denoted on the graph as A and A^*. These two peaks correspond to the emission from neutral and charged excitons, respectively. Spectra from the monolayer alloys with the high Mo content contain an additional less pronounced peak denoted as B which is attributed to the PL from

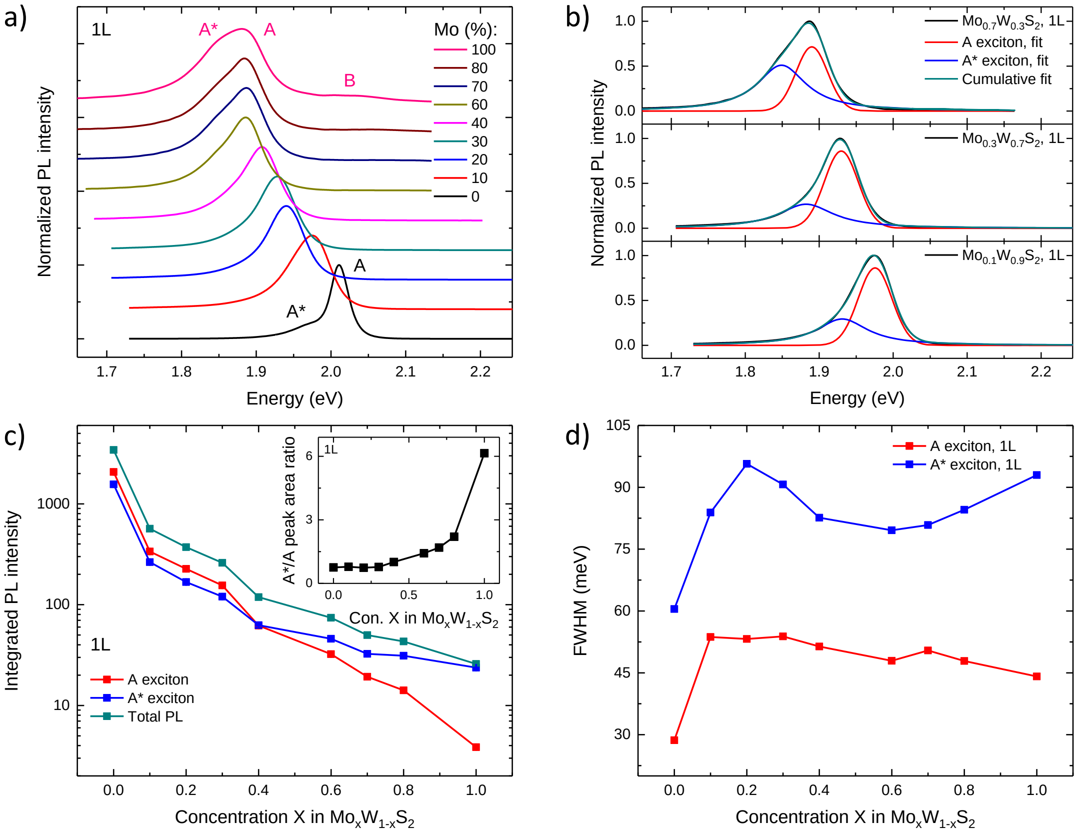

Fig. 3.3 Room-temperature PL measurements of monolayer $Mo_xW_{1-x}S_2$ alloys under 20 μW laser excitation at 2.33 eV. (a) Vertically stacked normalized PL spectra taken from the alloy monolayers with different Mo concentrations. A, A^* and B indicates peak positions for corresponding excitons. (b) Three examples of spectral fits (for the single-layer alloys with 10 %, 30 % and 70 % Mo content) consisting of two peaks which correspond to A (red curve) and A^* (blue curve) excitons. The cumulative fits are denoted with the dark cyan solid curves. (c) Integrated PL peak intensities obtained from the fitting as functions of the Mo concentration in the alloys. Data for A, A^* peaks and full-range spectra are plotted with red, blue and dark cyan symbols and lines, respectively. Inset: dependence of the ratio between A^* and A exciton peak areas on the Mo content. (d) FWHM values for A (red) and A^* (blue) exciton peaks as functions of the Mo concentration.

the B exciton states [1].

In what follows we analyse the spectral properties of the PL emission presented in Fig. 3.3a. PL spectra in Fig. 3.3a are fitted with Gaussian and Lorentzian peak functions. Fig. 3.3b demonstrates several fitted spectra. The best fits for the neutral A exciton peaks are obtained using a Gaussian lineshape, while the charged A^* exciton peak shapes correspond to Lorentzians. In comparison with the neutral excitons, the trions contain additional charge carriers and as a result may exhibit stronger scattering at room temperature, which may be responsible for the Lorentzian lineshape. Spectral parameters, such as peak positions, integrated peak areas and full widths at half maxima (FWHM), are obtained from the fitting and presented in Fig. 3.3b–d and Fig. 3.4. The standard error bars for those parameters are very small and less than the size of the data points on the plots (except for the error bars depicted in Fig. 3.4b for the parameter $E_{A^*\text{-}A}$). The B exciton peaks are fitted with Gaussian functions and included in the fitting only for the emission from the monolayer $Mo_{0.8}W_{0.2}S_2$ alloy and MoS_2. For the other materials with higher tungsten concentrations and WS_2, the B exciton signal is negligible.

As seen in Fig. 3.3c, both areas of A and A^* peaks decrease with the increasing Mo concentration. The total integrated PL intensity shows a similar behaviour. However, the charged exciton peak area increases relative to the neutral exciton peak area as shown in the inset of Fig. 3.3c. The ratio of A^* to A exciton peak area changes non-linearly and reaches 6 for the monolayer MoS_2. Contributions of A and A^* exciton peaks to the total PL signal are almost equal at 40 % Mo content. Such changes of the A^*/A peak area ratio appear to be a consequence of the doping effect when adding Mo. Our suggestions on this topic are discussed in section 3.4.

The presence of Mo in the alloys makes their spectral peaks much broader than the peaks from the WS_2 sample (Fig. 3.3d). Nevertheless, the A exciton peak linewidth becomes slightly smaller with the increasing Mo concentration and decreases from almost 54 meV for the $Mo_{0.1}W_{0.9}S_2$ alloy to 44 meV for the MoS_2 sample. FWHM of the A^* exciton peak shows more complicated behaviour exhibiting a maximum at 20 % Mo content ($\sim$ 96 meV) and a minimum at 60 % Mo content ($\sim$ 80 meV). In

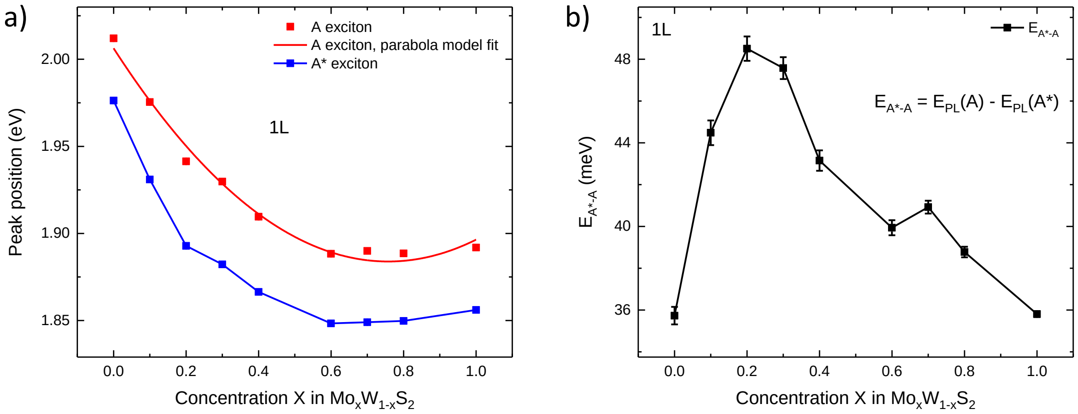

Fig. 3.4 Spectral positions of the A and A^* peaks in the monolayer $Mo_xW_{1-x}S_2$ alloys. (a) The A (red dots) and A^* (blue lines and dots) exciton peak positions obtained from the spectral peak fitting as functions of the Mo concentration in the alloys. The red curve is the parabola fit as described in the text. (b) Dependence of difference $E_{A^*\text{-}A}$ between the A and A^* exciton peak positions on the Mo content. Dots with standard error bars are taken from the spectral fits.

contrast to the neutral exciton peak linewidth, FWHM of the trion peak increases in the range of 60–100 % Mo concentration.

Similarly to the results from many bulk semiconductor alloys [32, 33], the band-edge PL of $Mo_xW_{1-x}S_2$ alloys is a non-linear function of the Mo concentration x (the so-called bowing effect) and can be well described by the following parabolic dependence:

$$E(x) = xE_{\mathrm{PL,MoS_2}} + (1-x)E_{\mathrm{PL,WS_2}} - bx(1-x), \tag{3.1}$$

where b is the so-called bowing parameter [32, 33]. From such parabola fitting of the A exciton peak positions (Fig. 3.4a), parameters b of 0.21 ± 0.02 eV, $E_{\mathrm{PL,WS_2}}$ of 2.006 ± 0.004 eV and $E_{\mathrm{PL,MoS_2}}$ of 1.90 ± 0.03 eV are obtained. The bowing parameter $b = 0.21$ eV is notably higher than the difference between the bandgap values of the pure WS_2 and MoS_2, 0.11 eV [25]. Using the identical method, Chen *et al.* [24] reported almost the same value of the bowing parameter $b = 0.25 \pm 0.04$ eV for $Mo_xW_{1-x}S_2$ monolayers. The parabola fit minimum in our calculation is around 70–80 % Mo content [24, 27]. The total peak position redshift is approximately 120 meV (from 2.01 eV to 1.88 eV) for the A exciton peak with the increase in the Mo concentration. The difference $E_{A^*\text{-}A}$ between peak positions for A and A^* is shown in Fig. 3.4b. This difference is usually interpreted as the binding energy of A^* excitons. In our case, we observe that the peak energy difference grows for $x < 0.2$ from 36 to 49 meV, and then gradually decreases back to 36 meV for $x = 1$. Because of the low A^*/A peak area ratio at 0–20 % Mo (the inset of Fig. 3.3c), it is more likely that the fitting of the A^* peak shapes with Lorentzian functions does not work well in that range of the alloy composition, causing the aforesaid drastic rise of $E_{A^*\text{-}A}$. Or such dramatic changes occur due to the effects in the electronic structure as discussed in section 3.4.

3.3.2 Photoluminescence from bilayer $Mo_xW_{1-x}S_2$ alloys

In this subsection, the results for the PL measurements of the bilayer $Mo_xW_{1-x}S_2$ alloys are described and illustrated in Fig. 3.5 and Fig. 3.6. The normalized PL spectra taken from alloy bilayers are presented in Fig. 3.5a. The energy redshift of spectral peak positions is observed with the increasing Mo concentration. Each spectrum contains the signal from A excitons and most of the spectra show the PL from B excitons. Recombination of A and B excitons is direct in momentum space. In addition to the direct-gap exciton peaks, the broad feature I, which is presented in all PL spectra from the bilayer alloys at significantly lower energy compared with the A exciton, seems to be the result of the indirect-gap transitions (the details are in section 3.1).

We now analyse the PL spectra using the fitting methods similar to those in Fig. 3.3 and Fig. 3.4. Fig. 3.5b shows three fitted spectra as an example. In contrast to monolayers, all bilayer direct-gap peak shapes correspond to Lorentzians. This may be explained by the presence of additional carrier relaxation in bilayers. The B exciton peaks are visible from the $Mo_{0.3}W_{0.8}S_2$ alloy up to MoS_2. The indirect-gap features I are fitted with Gaussian peaks. Fig. 3.5c–d and Fig. 3.6 present dependences of spectral parameters, namely PL peak positions, the integrated area and FWHM, on the Mo concentration in the alloys. Except for the linewidth values of the B exciton peaks, the calculated standard error bars are smaller than the point

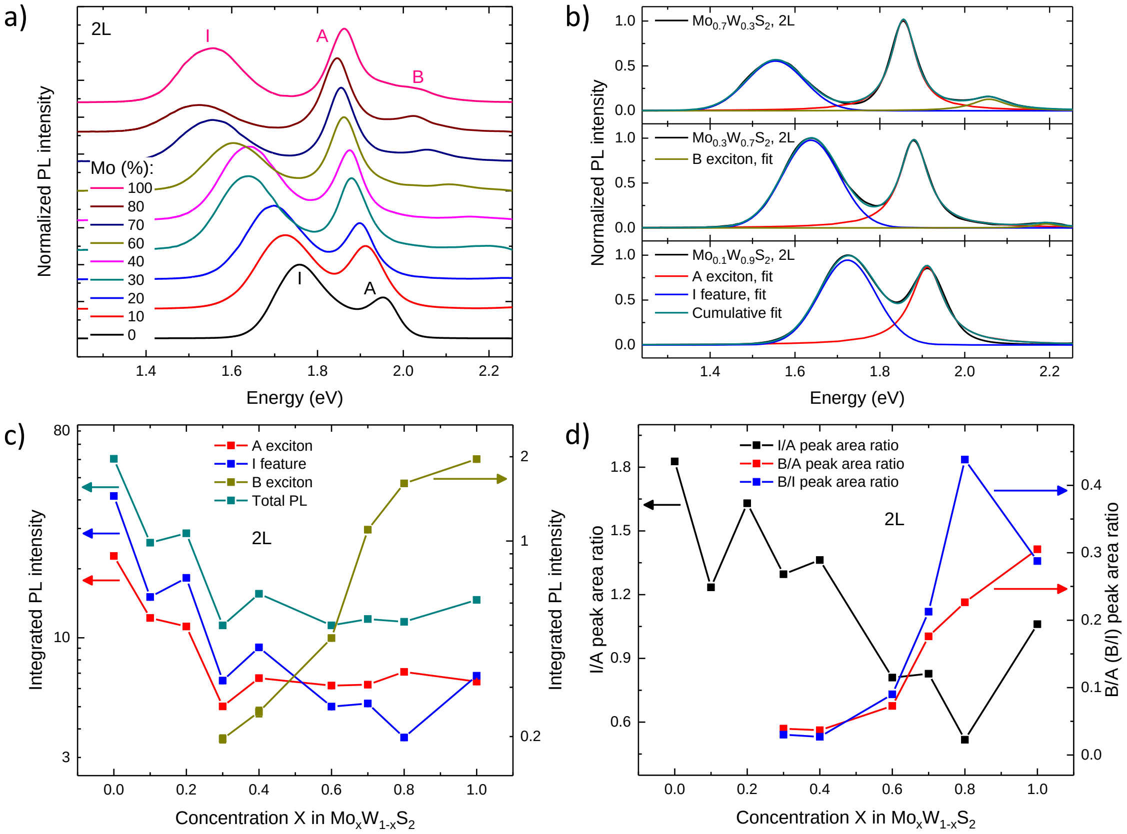

Fig. 3.5 Room-temperature PL measurements of bilayer $Mo_xW_{1-x}S_2$ alloys under 20 μW laser excitation at 2.33 eV. (a) Vertically stacked normalized PL spectra taken from the alloy bilayers with different Mo concentrations. *A*, *B* and *I* indicate peak positions for direct-gap (in momentum space) *A*, *B* excitons and indirect-gap transition, respectively. (b) Three examples of spectral fits (for the alloys with 10 %, 30 % and 70 % Mo content) consisting of three peaks which correspond to *A* (red curve), *B* (dark yellow curve) excitons and *I* (blue curve) feature (the spectral fit for the alloy with 10 % Mo content does not contain the *B* exciton peak fit). The cumulative fits are denoted with the dark cyan solid curves. (c) Integrated PL peak intensities obtained from the fitting as functions of the Mo concentration in the alloys. Data for *A*, *I* peaks, full-range spectra (left vertical scale) and *B* peak (right vertical scale) are plotted with red, blue, dark cyan and dark yellow symbols and lines, respectively. (d) Dependence of the ratios between different peak areas on the Mo content. Left vertical scale: *I* to *A* (black). Right vertical scale: *B* to *A* (red) and *B* to *I* (blue).

size on the figures.

The indirect band gap of the bilayer $Mo_xW_{1-x}S_2$ alloys makes the PL peak intensities much lower relative to the signal from the monolayer alloys (Fig. 3.3c and Fig. 3.5c), because the energetically preferable indirect-gap transitions mostly occur in a non-radiative way, and the radiative indirect-gap recombination is slower than the direct-gap one in the monolayer alloys due to the involvement of the phonons in the recombination processes. As shown in Fig. 3.5c, the integrated PL intensities of A and I peaks decrease with the increasing Mo concentration. The total area under the whole PL signal has the same tendency. Nevertheless, the B exciton peak area increases for alloys with higher Mo concentration. For the pure bilayer WS_2, the integrated intensity of the A peak is only half of that of the I peak. However, the area of the indirect-gap feature I quenches more dramatically than that of the A exciton peak with the increase in the Mo concentration and both areas become nearly equal in a range of 40–60 % Mo content in the alloys as shown in Fig. 3.5c–d.

According to the FWHM values from all PL spectra of $Mo_xW_{1-x}S_2$ bilayers, the indirect-gap feature I is much broader than the direct-gap A exciton (Fig. 3.6a). In the WS_2 bilayer, the linewidth of the I peak is around 143 meV and the A peak has $\sim$ 90 meV FWHM. With the increase in the Mo concentration, the peak of the feature I slightly widens up to 157–160 meV while the A exciton peak decreases in the linewidth down to 72–75 meV. Broadening of the B exciton peak is more significant: from almost 71 mev in the $Mo_{0.3}W_{0.7}S_2$ alloy to $\sim$ 135 meV in the pure MoS_2. It is worth mentioning that the width of the A exciton PL in the bilayers is significantly increased relative to that in the monolayers. The comparison and analysis of the A exciton linewidths will be presented in subsection 3.3.3.

As discussed in subsection 3.3.1, the peak positions of the band-edge PL of $Mo_xW_{1-x}S_2$ alloys can be described by the parabolic dependence in Eq. (3.1). Similar parabola fitting is applied to the peak positions from spectral fits in Fig. 3.6b. For the A exciton peak positions, parameters b of 0.15 ± 0.02 eV, $E_{\mathrm{PL,WS_2}}$ of 1.938 ± 0.004 eV and $E_{\mathrm{PL,MoS_2}}$ of 1.86 ± 0.03 eV are calculated. The bowing effect is significant, because the bowing parameter $b = 0.15$ eV is higher than the bandgap energy difference

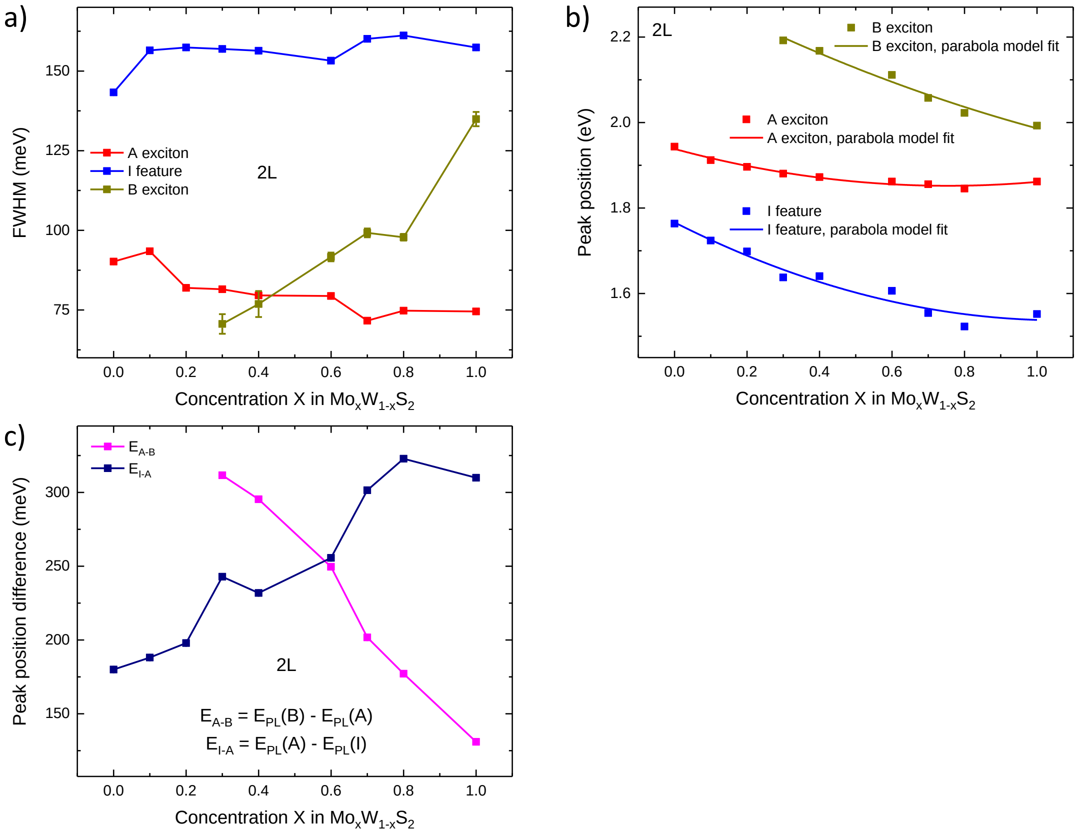

Fig. 3.6 FWHM and spectral positions of the exciton peaks in the bilayer $Mo_xW_{1-x}S_2$ alloys. (a) The FWHM values with standard error bars for the *A* (red), *I* (blue) and *B* (dark yellow) peaks as functions of the Mo concentration in the alloys. (b) The composition-dependent *A* (red dots), *I* (blue dots) and *B* (dark yellow dots) peak positions obtained from the spectral peak fitting. The corresponding coloured curves are the parabola fits as described in the text. (c) Dependence of difference $E_{I\text{-}A}$ between the *A* and *I* exciton peak positions (navy) as well as the *A*-*B* separation (magenta) on the Mo content. Dots are taken from the spectral fits.

between the pure WS_2 and MoS_2, 0.08 eV [25]. The value of the parameter b for the *A* exciton peak positions is decreased in the bilayers with regard to the monolayers. For the *I* feature peak positions, we use the similar parabolic dependence for the indirect-gap optical transitions:

$$E(x) = xE_{\mathrm{PL}_{ind},\mathrm{MoS}_2} + (1-x)E_{\mathrm{PL}_{ind},\mathrm{WS}_2} - b_{ind}x(1-x) \tag{3.2}$$

and obtain the following parameters: b_{ind} of 0.20 ± 0.07 eV, $E_{\mathrm{PL}_{ind},\mathrm{WS}_2}$ of 1.766 ± 0.015 eV and $E_{\mathrm{PL}_{ind},\mathrm{MoS}_2}$ of 1.54 ± 0.11 eV. The difference between indirect-gap energies of the WS_2 and MoS_2, 0.23 eV, is comparable to the bowing parameter value

$b_{ind} = 0.20$ eV. The *B* exciton peak positions show almost linear dependence without the bowing effect on the alloy composition. The significant peak position redshifts of $\sim$ 230 meV (from 1.77 eV to 1.54 eV) for the *I* peak and $\sim$ 210 meV (from 2.20 eV to 1.99 eV) for the *B* peak are observed with the increasing Mo concentration. The total *A* peak position redshift is almost 80 meV (from 1.94 eV to 1.86 eV). This represents a significant change compared with the tuning of the *A* exciton peak positions in the monolayer alloys in Fig. 3.4a. The detailed comparison of the *A* exciton peak position behaviour in the alloy mono-, bi- and trilayers will be presented in subsection 3.3.4. Similarly to the *A* exciton peak positions in the single-layer alloys, the parabola fit for the *A* exciton peak positions has a minimum in the range of 70–80 % Mo content. The energy separation $E_{A\text{-}B}$ of *A* and *B* exciton states as well as difference $E_{I\text{-}A}$ between peak positions for *A* and *I* are shown as functions of the alloy composition in Fig. 3.6c. These energy separations show large variations: from 316 meV to 125 meV for $E_{A\text{-}B}$ in the range of 30–100 % Mo content and from 172 meV to 323 eV for $E_{I\text{-}A}$ in the full range (0–100 %) of Mo content.

3.3.3 Photoluminescence from trilayer $Mo_xW_{1-x}S_2$ alloys

This subsection presents data taken from the trilayer $Mo_xW_{1-x}S_2$ alloys. The results are demonstrated in Fig. 3.7 and Fig. 3.8. A stack with the smoothed normalized PL spectra is plotted in Fig. 3.7a. The energy redshift of spectral peak positions is observed with the increasing Mo concentration. As for the PL spectra from the bilayers presented in subsection 3.3.2, almost all PL spectra from the alloy trilayers consist of the direct-gap peaks of *A* and *B* excitons as well as the broad feature *I* of the indirect-gap transition. The energy position of the *I* feature emission is much lower than that of the *A* exciton peak. More information on the origin of the above-mentioned optical transitions is written in section 3.1.

The PL spectra of the alloy trilayers are fitted for further analysis. Three fitted spectra of alloys with 10 %, 30 % and 70 % Mo content depicted in Fig. 3.7b are chosen as examples. Similarly to the spectral fitting for the bilayer alloys described in subsection 3.3.2, Lorentzian peak functions are used for the direct-gap, *A* and

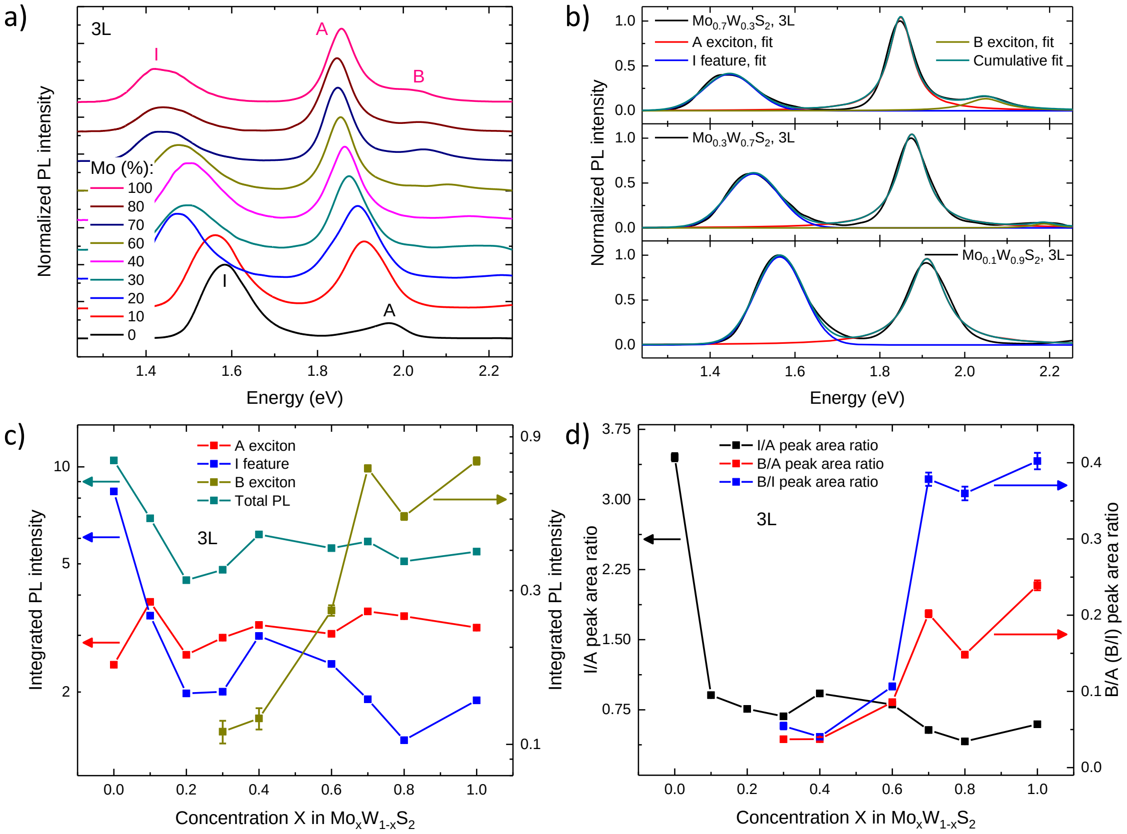

Fig. 3.7 Room-temperature PL measurements of trilayer $Mo_xW_{1-x}S_2$ alloys under 20 μW laser excitation at 2.33 eV. (a) Vertically stacked normalized PL spectra taken from the alloy trilayers with different Mo concentrations. *A*, *B* and *I* indicate peak positions for direct-gap (in momentum space) *A*, *B* excitons and indirect-gap transition, respectively. (b) Three examples of spectral fits (for the alloys with 10 %, 30 % and 70 % Mo content) consisting of three peaks which correspond to *A* (red curve), *B* (dark yellow curve) excitons and *I* (blue curve) feature (the spectral fit for the alloy with 10 % Mo content does not contain the *B* exciton peak fit). The cumulative fits are denoted with the dark cyan solid curves. (c) Integrated PL peak intensities with standard error bars obtained from the fitting as functions of the Mo concentration in the alloys. Data for *A*, *I* peaks, full-range spectra (left vertical scale) and *B* peak (right vertical scale) are plotted with red, blue, dark cyan and dark yellow symbols and lines, respectively. (d) Dependence of the ratios (with standard error bars) between different peak areas on the Mo content. Left vertical scale: *I* to *A* (black). Right vertical scale: *B* to *A* (red) and *B* to *I* (blue).

B, exciton signals while the I feature corresponds to Gaussian fits. The B exciton fitted spectra are analysed for the alloys with 30–100 % Mo content. The spectral fitting parameters are shown as functions of the alloy composition in Fig. 3.7c–d and Fig. 3.8. Standard errors of the plotted parameters are also calculated and depicted in the figures. In most cases, the error bars are less than the point size on the plots.

Fig. 3.7c–d shows the integrated PL intensities of all spectral peaks and their relative ratios for the trilayer alloys. The I feature peak area and, as a consequence, the total area under the whole spectral curve dramatically decline when the Mo concentration in the alloys rises from 0 to 20 %. The similar changes of the I/A peak area ratio happen in that range. With further increase in the Mo concentration, the above areas do not change their values significantly while the I/A peak area ratio slightly decreases. The A exciton peak areas show almost the same values of about 2.4–3.6 cts·eV·s^{-1} in the full range (0–100 %) of Mo content. As in the case of the bilayers, the integrated PL intensity of the B exciton peak dramatically grows in absolute terms and in comparison to the A and I peaks with the increasing Mo concentration.

The spectral linewidths of A, B and I peaks for all measured alloy trilayer compositions are illustrated in Fig. 3.8a. In the pure WS_2 trilayer, A and I peaks have almost the same broad widths $\sim$ 125–128 meV. When the Mo fraction increases in the alloys, FWHM values of the A exciton peak significantly drop down to 71 meV in the pure MoS_2, while the I feature peak becomes to be slightly broader (up to $\sim$ 139–143 meV). The peak of the B excitons widens from 70 meV in the $Mo_{0.3}W_{0.7}S_2$ alloy to 129 meV in the MoS_2. Note that the A exciton peak width in the bi- and trilayers is significantly increased compared to the monolayers as shown in Fig. 3.8d. The presence of the interlayer coupling, band structure changes (the indirect-gap transitions with the phonon involvement) in the multilayer alloys influence the spectral parameters of the emitted direct-gap peaks.

The parabolic dependence of the peak positions of the band-edge emission of the trilayer $Mo_xW_{1-x}S_2$ alloys, which is the so-called bowing effect, is observed. Therefore, we apply again the parabola model fitting as presented in Fig. 3.8b and previously

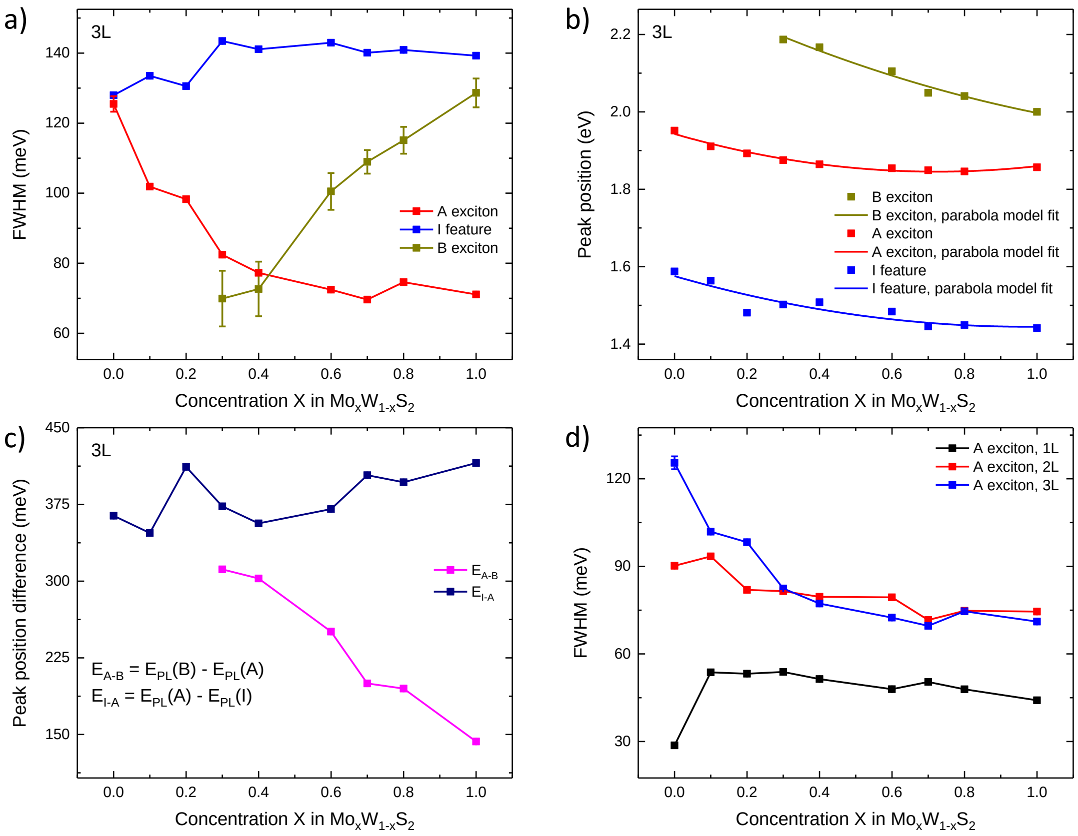

Fig. 3.8 FWHM and spectral positions of the exciton peaks in the trilayer $Mo_xW_{1-x}S_2$ alloys. (a) The FWHM values with standard error bars for the A (red), I (blue) and B (dark yellow) peaks as functions of the Mo concentration in the alloys. (b) The composition-dependent A (red dots), I (blue dots) and B (dark yellow dots) peak positions obtained from the spectral peak fitting. The corresponding coloured curves are the parabola fits as described in the text. (c) Dependence of difference $E_{I\text{-}A}$ between the A and I exciton peak positions (navy) as well as the A-B separation (magenta) on the Mo content. Dots are taken from the spectral fits. (d) The comparison of the FWHM values of the A exciton peaks taken from the alloy mono- (black), bi- (red) and trilayers (blue) as functions of the alloy composition.

described in subsections 3.3.1 and 3.3.2. The following parameters for A exciton peak positions are obtained: b of 0.19 ± 0.02 eV, $E_{\mathrm{PL,WS_2}}$ of 1.943 ± 0.005 eV and $E_{\mathrm{PL,MoS_2}}$ of 1.86 ± 0.03 eV. The bandgap energy difference between the trilayer WS_2 and MoS_2, 0.08 eV, is much lower that the value of the bowing parameter $b = 0.19$ eV. This confirms the presence of the considerable bowing effect [25]. As in the alloy bilayers, the bowing parameter $b = 0.19 \pm 0.02$ eV for the A exciton peak positions in the trilayers is slightly lower than that in the monolayers ($b = 0.21 \pm 0.02$ eV). Having used Eq. (3.2) and calculated the fitting parameters for the I feature peak positions, we obtain the following: b_{ind} of 0.14 ± 0.09 eV, $E_{\mathrm{PL}_{ind},\mathrm{WS}_2}$ of 1.58 ± 0.02 eV, $E_{\mathrm{PL}_{ind},\mathrm{MoS}_2}$ of 1.44 ± 0.13 eV and $E_{\mathrm{PL}_{ind},\mathrm{WS}_2} - E_{\mathrm{PL}_{ind},\mathrm{MoS}_2} =\sim 0.13$ eV. Bowing is weak since the bowing parameter $b_{ind} = 0.14$ eV is almost equal to the indirect-gap energy difference $E_{\mathrm{PL}_{ind},\mathrm{WS}_2} - E_{\mathrm{PL}_{ind},\mathrm{MoS}_2} = 0.13$ eV. Additionally, this bowing parameter $b_{ind} = 0.14$ eV for the I feature peak positions in the trilayers is much less relative to that in the bilayers ($b_{ind} = 0.20$ eV). This is an evidence that the number of layers significantly influences the electronic band structure of the TMDC alloy materials. It is established that the peak positions for the B excitons have almost linear dependence on the alloy composition. Unlike the case of the bilayers, the peak position redshift for the feature I is much less and equals $\sim$ 130 meV (from 1.58 eV to 1.44 eV). The B exciton peak position redshift in the trilayers remains almost the same: $\sim$ 200 meV (from 2.19 eV to 2.00 eV) against about 210 meV in the bilayers. The signal of A excitons show $\sim$ 100 meV redshift (from 1.94 eV to 1.85 eV). The parabola fit minimum of the A exciton peak positions is located between 70 % and 80 % Mo content [24, 27]. Fig. 3.8c represents the energy separations $E_{A\text{-}B}$ and $E_{I\text{-}A}$, which are defined in subsection 3.3.2, as functions of the alloy composition. Comparing with the data from the alloy bilayers, $E_{A\text{-}B}$ does not so remarkably vary (from 311 meV to 143 meV in the range of 30–100 % Mo content) but the $E_{I\text{-}A}$ values are much energetically higher (from 364 meV to 415 meV in the range of 0–100 % Mo content). In accordance with [4] in the pure MoS_2 and WS_2 materials, the indirect-gap energies are dramatically changed with the flake thickness (by hundreds of meV from bilayer to 6-layer) while the direct-gap energies do not show such large modifications. Thus, the I-A energy separation of the studied alloys considerably differs for the bi- and trilayers.

3.3.4 Reflectance contrast measurements

Fig. 3.9 and Fig. 3.10 demonstrate our room-temperature RC spectroscopy results from the $\mathrm{Mo}_x\mathrm{W}_{1-x}\mathrm{S}_2$. The white light source with 360–2600 nm wavelength has been used to analyse the optical reflection from the mono-, bi- and trilayer alloys.

The general view of the normalized RC spectra is represented in Fig. 3.9. For our

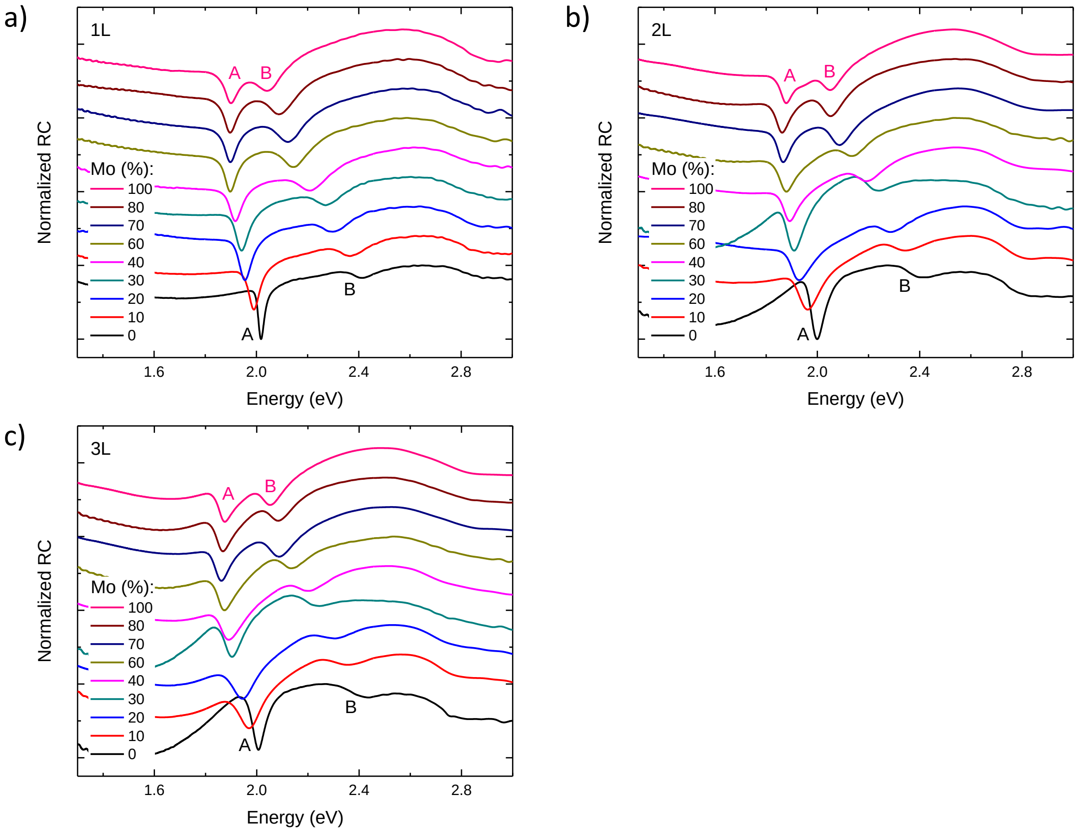

Fig. 3.9 Room-temperature vertically stacked normalized RC spectra taken from the (a) mono-, (b) bi- and (c) trilayer $Mo_xW_{1-x}S_2$ alloys with the different Mo concentrations under the white light (360–2600 nm) excitation. *A* and *B* indicate peak positions for direct-gap (in momentum space) *A* and *B* excitons, respectively. The Mo content percentage are specified in the legends of the plots. $1L$, $2L$, $3L$ denote 1, 2, 3 layers.

experiments, we use Eq. (2.2) to calculate reflectance contrast values. This formula is described in detail in subsection 2.2.2. The RC spectra of the bi- and trilayer WS_2 and $Mo_{0.3}W_{0.7}S_2$ alloys have slightly different spectral shapes because of the influence of the substrates: most samples are positioned on the regular 90–100 nm SiO_2/Si substrates while those on the high-quality 100 nm SiO_2/Si. The peaks of *A* and *B* excitons, which are the result of the valence-band spin-orbit coupling as discussed in the previous subsections, are located at the extremal minima and clearly visible in the spectra. The energy redshift of the *A* and *B* exciton peak positions with the increase in the Mo concentration are observed. It is also seen from the presented spectra that the *A*-*B* energy separation decreases when changing the alloy from the pure WS_2 to MoS_2. Spectral peaks of the alloy bi- and trilayers

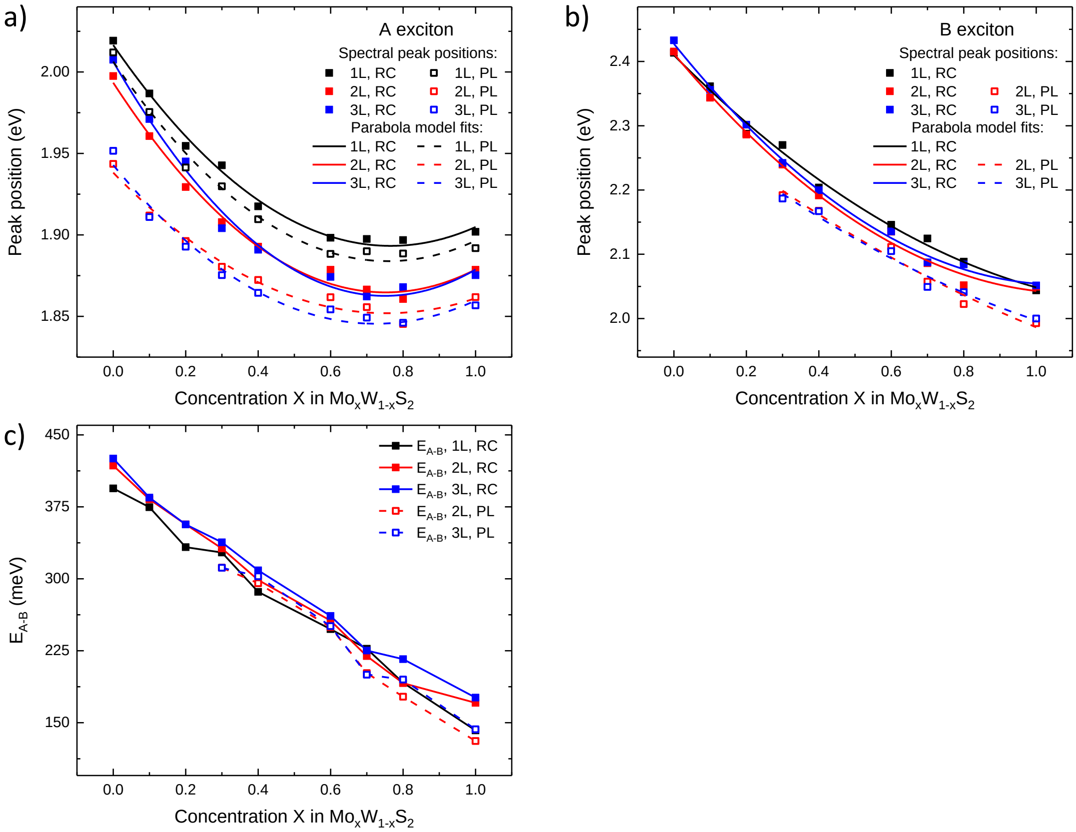

Fig. 3.10 Peak positions and energy differences from the RC spectra of the mono- (1L), bi- (2L) and trilayer (3L) $\mathbf{Mo_xW_{1-x}S_2}$ alloys. (a) The A and (b) B exciton peak positions obtained from the RC spectra of the mono- (black solid dots), bi- (red solid dots) and trilayer (blue solid dots) alloys as functions of the Mo concentration. The corresponding coloured curves are the parabola model fits as described in the text. (c) The A-B energy separation $E_{A\text{-}B}$ values taken from the RC spectra as functions of the alloy composition. Black, red and blue symbols and lines relate to the data from the RC spectra of the mono-, bi- and trilayer alloys, respectively. (a)–(c) For comparison with the RC data, coloured unfilled dots and dashed curves are the peak positions and their parabola fits taken from the PL spectra presented in subsections 3.3.1–3.3.3.

Table 3.1 The parabola model fitting parameters for the A exciton peak positions obtained from the PL and RC spectra. The unit for the parameters is eV. $1L$, $2L$ and $3L$ denote the mono-, bi- and trilayer $Mo_xW_{1-x}S_2$ alloys. Standard errors are taken from the fitting.

Thickness	Method	b	E_{MoS_2}	E_{WS_2}	$E_{WS_2} - E_{MoS_2}$
1L	RC	0.21 ± 0.02	1.905 ± 0.022	2.017 ± 0.003	0.112 ± 0.023
	PL	0.21 ± 0.02	1.896 ± 0.030	2.006 ± 0.004	0.110 ± 0.030
2L	RC	0.23 ± 0.02	1.879 ± 0.027	1.993 ± 0.004	0.115 ± 0.027
	PL	0.15 ± 0.02	1.861 ± 0.028	1.938 ± 0.004	0.077 ± 0.029
3L	RC	0.26 ± 0.02	1.879 ± 0.032	2.006 ± 0.005	0.128 ± 0.032
	PL	0.19 ± 0.02	1.860 ± 0.032	1.943 ± 0.005	0.083 ± 0.032

are broader than those of the monolayers. Note that the RC spectra do not contain data from the A^* charged exciton peak and indirect-gap feature I because of their low oscillator strength [2, 34].

Peak positions as extremal minima are extracted from the smoothed RC spectra and analysed in Fig. 3.10. For comparison, the corresponding peak positions and energy separations obtained from the PL spectra, discussed in the previous subsections (3.3.1–3.3.3), are included in Fig. 3.10. The PL peak positions are lower in energy (for a few tens of meV) than those from the RC spectra, being in agreement with the previously published results from semiconducting TMDCs [35, 36]. This appears to be related to the so-called Stokes shifts.

As in the case of PL, the peak positions from the RC spectra of the $Mo_xW_{1-x}S_2$ alloys can be described by the parabolic dependence which is similar to Eq. (3.1):

$$E(x) = xE_{\mathrm{RC,MoS_2}} + (1-x)E_{\mathrm{RC,WS_2}} - b_{\mathrm{RC}}x(1-x). \tag{3.3}$$

Fig. 3.10a contains RC data for the A peak positions. From the parabola model fitting, we estimate parameters and compare them with those from the PL data in Table 3.1.

From both PL and RC spectral results, it is clear that the A exciton peak positions in the $Mo_xW_{1-x}S_2$ monolayers are shifted relatively those in the bi- and trilayers which look almost similar. This difference in the peak positions becomes smaller when the alloy composition parameter $x \to 0$ in the RC data and $x \to 1$ in the PL data. On average, that shift equals $\sim$ 10–25 meV in the RC spectra and $\sim$ 35–65 meV in the PL spectra. The observation of the shift of the A peak positions with the number of the atomic layers occurs because the band edges at the K points of the Brillouin zone are sensitive to the interlayer coupling but not too much as they are made of the metal d orbitals (similarly to the effects considered in section 1.2 in the pure semiconducting TMDCs). Additionally, various relaxation processes including the phonon involvement are likely to have time to significantly impact A excitons before the light emission. Hence, the composition-dependent A peak position trends obtained from the RC and PL spectra are different. For B excitons, such trends are noticeably larger in energy so that the existed difference between the RC peak positions in the mono- and few-layers is hardly visible in Fig. 3.10b (PL data for the single atomic layers is absent owing to the negligible B exciton signal).

As presented in Table 3.1, the RC spectra of the mono-, bi- and trilayer alloys have big parabolic bowing of the A peak positions: the bowing parameter b_{RC} is higher than the bandgap energy difference $E_{\mathrm{RC,WS_2}} - E_{\mathrm{RC,MoS_2}}$ between the WS_2 and MoS_2 (the same effect has been earlier established in the monolayer $Mo_xW_{1-x}Se_2$ [25]). The values of b_{RC} and $E_{\mathrm{RC,WS_2}} - E_{\mathrm{RC,MoS_2}}$ increase with the number of layers. The energy minima of the parabola fits are between 70 and 80 % Mo content which are similar to the results from the PL spectra and published papers [24, 27]. The energy redshift of the A exciton peak positions with the increase in the Mo concentration also grows from the monolayer to trilayer alloys in the RC spectra: $\sim$ 120 meV in the monolayers (from 2.02 eV to 1.89 eV); $\sim$ 130 meV in the bilayers (from 1.99 eV to 1.86 eV); $\sim$ 140 meV in the trilayers (from 2.01 eV to 1.86 eV).

According to the data from Table 3.1 and previous subsections (3.3.1–3.3.3), all PL A exciton peak parameters, such as the linewidth, intensity, position shift, bowing parameter b and energy difference $E_{\mathrm{WS_2}} - E_{\mathrm{MoS_2}}$, have prominent changes when going from the monolayer to the multilayer alloys. Between the bilayer and trilayer alloys, all PL parameter variations conform to the same behaviour as in the RC results.

Table 3.2 The parabola model fitting parameters for the *B* exciton peak positions obtained from the PL and RC spectra. The unit for the parameters is eV. 1*L*, 2*L* and 3*L* denote the mono-, bi- and trilayer $Mo_xW_{1-x}S_2$ alloys. Standard errors are taken from the fitting.

Thickness	Method	b	E_{MoS_2}	E_{WS_2}*	E_{WS_2}* $- E_{MoS_2}$
1L	RC	0.20 ± 0.04	2.048 ± 0.061	2.410 ± 0.009	0.361 ± 0.062
2L	RC	0.30 ± 0.04	2.043 ± 0.057	2.412 ± 0.008	0.369 ± 0.057
	PL	0.11 ± 0.12	1.986 ± 0.196	2.322 ± 0.045*	0.335 ± 0.201*
3L	RC	0.33 ± 0.03	2.054 ± 0.042	2.428 ± 0.006	0.373 ± 0.042
	PL	0.13 ± 0.11	1.997 ± 0.180	2.319 ± 0.041*	0.321 ± 0.184*

* For the PL results, $E_{Mo_{0.3}W_{0.7}S_2}$ and $E_{Mo_{0.3}W_{0.7}S_2} - E_{MoS_2}$ are calculated.

The *B* exciton peak positions with their parabola model fits based on PL and RC data of the mono-, bi- and trilayer $Mo_xW_{1-x}S_2$ alloys are illustrated in Fig. 3.10b. Table 3.2 demonstrates the data from the parabola model fitting. Because of the weak signal, the PL *B* exciton peak parameters are estimated for the alloys with 30–100 % Mo content. Bowing of the *B* exciton peak positions as functions of the alloy composition is presented in the RC spectra of all alloys and the bowing parameters b_{RC} are rather significant ($\sim$ 0.20–0.30 eV) in contrast to b_{PL} (0.11–0.13 eV). Nevertheless, the bowing appears to be weak compared with the energy difference between the optical transitions of *B* excitons of the pure WS_2 ($E_{Mo_{0.3}W_{0.7}S_2}$ for the PL results) and MoS_2. The positions of the *B* exciton peak show a giant energy redshift with the growth of the Mo fraction in the alloys. Additionally, this redshift rises with the flake thickness: 361 meV in the monolayers (from 2.41 eV to 2.05 eV); 369 meV in the bilayers (from 2.41 eV to 2.04 eV); 373 meV in the trilayers (from 2.43 eV to 2.05 eV). Similarly to the parameters obtained from the RC *A* exciton peak positions, b_{RC} and $E_{RC,WS_2} - E_{RC,MoS_2}$ of the *B* exciton peak positions also increase with the number of layers (Table 3.2).

The *A*-*B* energy separations $E_{A\text{-}B}$, which indicate the size of the valence-band spin-orbit coupling, are demonstrated in Fig. 3.10c as functions of the alloy composition. As in Fig. 3.10a-b, the RC data are compared with the PL data. Similarly to the PL results, $E_{A\text{-}B}$ from the RC spectra linearly changes with the Mo content in the alloys.

These changes are very large in the full range of the composition variation: from 394 meV to 142 meV in the monolayers; from 418 meV to 171 meV in the bilayers; from 425 meV to 176 meV in the trilayers. In addition to that, the $E_{A\text{-}B}$ values grow in absolute terms with the flake thickness.

3.4 Discussion

Due to the same lattice symmetry and small lattice mismatch between the MoS_2 and WS_2 (less than 1 % [37]), the so-called bowing effect of the energy band gaps which is described in subsections 3.3.1–3.3.4 can originate from orbital hybridization [38]. The explanation how the bowing originates in the Mo and W based TMDC monolayer alloys is presented in [25]. The orbital projected band structures were obtained in the monolayer MoS_2 by Liu *et al.* [15] using the first-principles calculations and can be extended to other monolayer semiconducting TMDCs (Fig. 3.11). From those calculations, the main contribution to the conduction-band electronic states of TMDCs at the $\pm K$ points of the Brillouin zone is from the d_{z^2} orbitals of the cation (metal) atoms. These orbitals operate along the out-of-plane, z direction and therefore, the in-plane inter-cation coupling of states is negligible. Additionally, the d_{z^2} orbitals of the Mo atoms are positioned energetically lower (by 0.47 eV) than those of the W atoms. As a consequence, the electronic states of the conduction band minimum (CBM), which is near the K points in the alloy monolayers, are localized around the Mo atoms even at very small Mo concentrations. This results in the rapid transformation of the CBM edges of the monolayer $Mo_xW_{1-x}X_2$ alloys towards that of the monolayer MoX_2 with adding the Mo content. In contrast to this, the valence band maximum (VBM) at the K points of the Brillouin zone mostly contains the d_{xy} and $d_{x^2-y^2}$ orbitals of the transition metals. These orbitals are spread in the x-y plane of the atomic lattice and strongly coupled to each other. Hence, the wavefunctions of the states are not localized and homogeneously distributed over all cations, leading to a linear change of the VBM energy. Combining all the above orbital states, the bandgap variation of the monolayer $Mo_xW_{1-x}X_2$ can be described

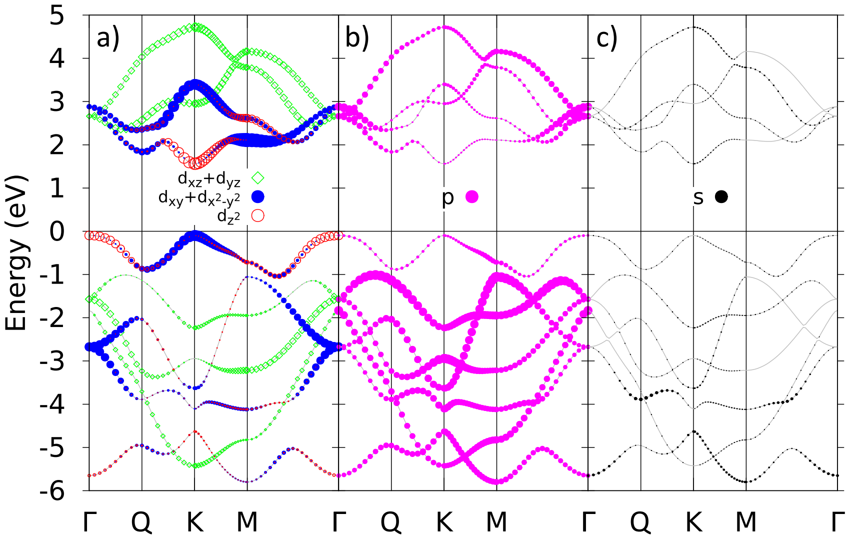

Fig. 3.11 The orbital contributions in the band structure of the monolayer MoS_2. The valence band maximum is set as a zero level. The orbital population in a state is reflected with the symbol size. (a) The Mo d orbitals in the monolayer MoS_2: d_{z^2} (red unfilled circles); d_{xy} and $d_{x^2-y^2}$ (blue circles); d_{xz} and d_{yz} (green unfilled diamonds). (b) The total p orbitals (mostly from the S atoms). (c) The total s orbitals. Taken and altered from [15].

by the parabolic dependence in Eq. (3.1) with the alloy composition.

The strong localization of the electronic states around the Mo atoms even with a small Mo fraction causes the significant changes in the optical properties of the single-layer $Mo_xW_{1-x}S_2$ alloys. Particularly, these changes are pronounced with the integrated intensities, linewidths of the PL peaks and energy difference $E_{A^*\text{-}A}$ in Fig. 3.3c–d and Fig. 3.4b. The intensity dropping is also a consequence of the spin-orbit splitting (Fig. 3.1a). The crossing of the spin-split conduction bands for the preferable states surrounding the Mo atoms (as in the pure molybdenum-containing TMDC monolayers [15, 39]) results that the energy of the bright exciton transitions is less than that of the dark exciton transitions in the ternary monolayers. Room temperature excites higher energetic states including dark excitons and the radiative recombination is partly replaced with non-radiative one. However, the Pauli exclusion principle probably keeps three-particle trion complexes to be optically bright in all studied monolayers. Thus, the A^*/A peak area ratio increases with the growth of the Mo content in the alloys.

The bi- and trilayers do not show the mentioned drastic changes in the integrated PL peak intensities, linewidths and energy separations at low Mo fractions because of the presence of the interlayer coupling and band structure modifications. As a result of increased number of layers, the band gap of the multilayer alloys is indirect, because the indirect-gap optical transitions between the VBM at the Γ point and CBM at the Q point (halfway across the Γ–K direction) of the Brillouin zone are energetically favorable as shown in Fig. 3.1b and described in section 3.1. From the first-principles results (Fig. 3.11), the Γ point contains the metal d_{z^2} orbitals while the metal d_{xy} and $d_{x^2-y^2}$ orbitals contribute to the Q point wavefunction [15]. According to the conclusions in [25] in the bi- and trilayer alloys, it should be expected that the CBM states at the Q point and the VBM states at the Γ point have linear and non-linear dependences on the alloy composition, respectively. This may explain a bowing effect for the indirect-gap peak I.

3.5 Conclusions

Using μPL and μRC spectroscopies at room temperature, we investigate in this study the mechanically exfoliated $\mathrm{Mo}_x\mathrm{W}_{1-x}\mathrm{S}_2$ alloys deposited on the SiO_2/Si substrates. The full set of the bi- and trilayer semiconducting TMDC alloys has been optically studied for the first time and compared with the results from the monolayers of the same materials. We present a detailed description of the spectral parameters (integrated intensities, linewidths, peak positions and peak separations) as functions of the alloy composition. The behaviour of the spectral peaks attributed to the indirect-gap optical transitions with the crystal thickness has been first demonstrated in the TMDC alloys. Further theoretical investigations are necessary in order to interpret our findings. We show that the indirect-to-direct band-gap crossover plays a significant role in changing the band structures and hence optical properties of the emitted signals from the alloys. Additional control of the band-gap energies with alloying allows to accomplish more precise band engineering which reveals new energetic landscapes for the applications in optoelectronics and energy conversion.

References

[1] G. Wang, C. Robert, A. Suslu, B. Chen, S. Yang, S. Alamdari, I. C. Gerber, T. Amand, X. Marie, S. Tongay, B. Urbaszek. Spin-orbit engineering in transition metal dichalcogenide alloy monolayers. *Nat. Commun.* **6**, 10110 (2015).

[2] K. F. Mak, C. Lee, J. Hone, J. Shan, T. F. Heinz. Atomically thin MoS_2: a new direct-gap semiconductor. *Phys. Rev. Lett.* **105 (13)**, 136805 (2010).

[3] A. Kuc, N. Zibouche, T. Heine. Influence of quantum confinement on the electronic structure of the transition metal sulfide TS_2. *Phys. Rev. B* **83 (24)**, 245213 (2011).

[4] A. Kumar, P. K. Ahluwalia. Electronic structure of transition metal dichalcogenides monolayers $1H$-MX_2 (M = Mo, W; X = S, Se, Te) from *ab-initio* theory: new direct band gap semiconductors. *Eur. Phys. J. B* **85**, 186 (2012).

[5] A. Splendiani, L. Sun, Y. Zhang, T. Li, J. Kim, C.-Y. Chim, G. Galli, F. Wang. Emerging photoluminescence in monolayer MoS_2. *Nano Lett.* **10 (4)**, 1271–1275 (2010).

[6] Z. Y. Zhu, Y. C. Cheng, U. Schwingenschlögl. Giant spin-orbit-induced spin splitting in two-dimensional transition-metal dichalcogenide semiconductors. *Phys. Rev. B* **84 (15)**, 153402 (2011).

[7] J. A. Wilson, A. D. Yoffe. The transition metal dichalcogenides discussion and interpretation of the observed optical, electrical and structural properties. *Advan. Phys.* **18 (73)**, 193 (1969).

[8] R. V. Kasowski. Band structure of MoS_2 and NbS_2. *Phys. Rev. Lett.* **30 (23)**, 1175 (1973).

[9] R. Coehoorn, C. Haas, R. A. de Groot. Electronic structure of $MoSe_2$, MoS_2 and WSe_2. II. The nature of the optical band gaps. *Phys. Rev. B* **35 (12)**, 6203 (1987).

[10] T. Cheiwchanchamnangij, W. R. L. Lambrecht. Quasiparticle band structure calculation of monolayer, bilayer, and bulk MoS_2. *Phys. Rev. B* **85 (20)**, 205302 (2012).

[11] E. S. Kadantsev, P. Hawrylak. Electronic structure of a single MoS_2 monolayer. *Solid State Commun.* **152 (10)**, 909–913 (2012).

[12] H. Zeng, B. Zhu, K. Liu, J. Fan, X. Cui, Q. M. Zhang. Low-frequency Raman modes and electronic excitations in atomically thin MoS_2 films. *Phys. Rev. B* **86 (24)**, 241301(R) (2012).

[13] H. Zeng, G.-B. Liu, J. Dai, Y. Yan, B. Zhu, R. He, L. Xie, S. Xu, X. Chen, W. Yao, X. Cui. Optical signature of symmetry variations and spin-valley coupling in atomically thin tungsten dichalcogenides. *Sci. Rep.* **3**, 1608 (2013).

[14] Y. Song, H. Dery. Transport theory of monolayer transition-metal dichalcogenides through symmetry. *Phys. Rev. Lett.* **111 (2)**, 026601 (2013).

[15] G.-B. Liu, W.-Y. Shan, Y. Yao, W. Yao, D. Xiao. Three-band tight-binding model for monolayers of group-VIB transition metal dichalcogenides. *Phys. Rev. B* **88 (8)**, 085433 (2013).

[16] J. Kang, S. Tongay, J. Zhou, J. Li, J. Wu. Band offsets and heterostructures of two-dimensional semiconductors. *Appl. Phys. Lett.* **102 (1)**, 012111 (2013).

[17] X. Li, J. T. Mullen, Z. Jin, K. M. Borysenko, M. B. Nardelli, K. W. Kim. Intrinsic electrical transport properties of monolayer silicene and MoS_2 from first principles. *Phys. Rev. B* **87 (11)**, 115418 (2013).

[18] H. R. Gutiérrez, N. Perea-López, A. L. Elías, A. Berkdemir, B. Wang, R. Lv, F. López-Urías, V. H. Crespi, H. Terrones, M. Terrones. Extraordinary room-temperature photoluminescence in triangular WS_2 monolayers. *Nano Lett.* **13 (8)**, 3447–3454 (2013).

[19] J. Xi, T. Zhao, D. Wang, Z. Shuai. Tunable electronic properties of two-dimensional transition metal dichalcogenide alloys: a first-principles prediction. *J. Phys. Chem. Lett.* **5 (2)**, 285–291 (2014).

[20] A. Steinhoff, J.-H. Kim, F. Jahnke, M. Rösner, D.-S. Kim, C. Lee, G. H. Han, M. S. Jeong, T. O. Wehling, C. Gies. Efficient excitonic photoluminescence in direct and indirect band gap monolayer MoS_2. *Nano Lett.* **15 (10)**, 6841–6847 (2015).

[21] D. Kozawa, R. Kumar, A. Carvalho, K. K. Amara, W. Zhao, S. Wang, M. Toh, R. M. Ribeiro, A. H. Castro Neto, K. Matsuda, G. Eda. Photocarrier relaxation pathway in two-dimensional semiconducting transition metal dichalcogenides. *Nat. Commun.* **5**, 4543 (2014).

[22] J. Pei, J. Yang, R. Xu, Y.-H. Zeng, Y. W. Myint, S. Zhang, J.-C. Zheng, Q. Qin, X. Wang, W. Jiang, Y. Lu. Exciton and trion dynamics in bilayer MoS_2. *Small* **11 (48)**, 6384–6390 (2015).

[23] M. Selig, G. Berghäuser, A. Raja, P. Nagler, C. Schüller, T. F. Heinz, T. Korn, A. Chernikov, E. Malic, A. Knorr. Excitonic linewidth and coherence lifetime in monolayer transition metal dichalcogenides. *Nat. Commun.* **7**, 13279 (2016).

[24] Y. Chen, J. Xi, D. O. Dumcenco, Z. Liu, K. Suenaga, D. Wang, Z. Shuai, Y.-S. Huang, L. Xie. Tunable band gap photoluminescence from atomically thin transition-metal dichalcogenide alloys. *ACS Nano* **7 (5)**, 4610–4616 (2013).

[25] S. Tongay, D. S. Narang, J. Kang, W. Fan, C. Ko, A. V. Luce, K. X. Wang, J. Suh, K. D. Patel, V. M. Pathak, J. Li, J. Wu. Two-dimensional semiconductor alloys: monolayer $Mo_{1-x}W_xSe_2$. *Appl. Phys. Lett.* **104 (1)**, 012101 (2014).

[26] A. F. Rigosi, H. M. Hill, K. T. Rim, G. W. Flynn, T. F. Heinz. Electronic band gaps and exciton binding energies in monolayer $Mo_xW_{1-x}S_2$ transition metal dichalcogenide alloys probed by scanning tunneling and optical spectroscopy. *Phys. Rev. B* **94 (7)**, 075440 (2016).

[27] M. Zhang, J. Wu, Y. Zhu, D. O. Dumcenco, J. Hong, N. Mao, S. Deng, Y. Chen, Y. Yang, C. Jin, S. H. Chaki, Y.-S. Huang, J. Zhang, L. Xie. Two-dimensional molybdenum tungsten diselenide alloys: photoluminescence, Raman scattering, and electrical transport. *ACS Nano* **8 (7)**, 7130–7137 (2014).

[28] S. Zheng, L. Sun, T. Yin, A. M. Dubrovkin, F. Liu, Z. Liu, Z. X. Shen, H. J. Fan. Monolayers of $W_xMo_{1-x}S_2$ alloy heterostructure with in-plane composition variations. *Appl. Phys. Lett.* **106 (6)**, 063113 (2015).

[29] Y. Kobayashi, S. Mori, Y. Maniwa, Y. Miyata. Bandgap-tunable lateral and vertical heterostructures based on monolayer $Mo_{1-x}W_xS_2$ alloys. *Nano Res.* **8 (10)**, 3261–3271 (2015).

[30] Y. Chen, W. Wen, Y. Zhu, N. Mao, Q. Feng, M. Zhang, H.-P. Hsu, J. Zhang, Y.-S. Huang, L. Xie. Temperature-dependent photoluminescence emission and Raman scattering from $Mo_{1-x}W_xS_2$ monolayers. *Nanotechnol.* **27 (44)**, 445705 (2016).

[31] E. M. Alexeev, A. Catanzaro, O. V. Skrypka, P. K. Nayak, S. Ahn, S. Pak, J. Lee, J. I. Sohn, K. S. Novoselov, H. S. Shin, A. I. Tartakovskii. Imaging of interlayer coupling in van der Waals heterostructures using a bright-field optical microscope. *Nano Lett.* **17 (9)**, 5342–5349 (2017).

[32] S. Adachi. *Properties of semiconductor alloys: group-IV, III-V and II-VI semiconductors* (John Wiley & Sons, Inc., Chichester, UK, 2009). ISBN: 9780470744383.

[33] W.-J. Yin, X.-G. Gong, S.-H. Wei. Origin of the unusually large band-gap bowing and the breakdown of the band-edge distribution rule in the Sn_xGe_{1-x} alloys. *Phys. Rev. B* **78 (16)**, 161203(R) (2008).

[34] A. Arora, R. Schmidt, R. Schneider, M. R. Molas, I. Breslavetz, M. Potemski, R. Bratschitsch. Valley Zeeman splitting and valley polarization of neutral and charged excitons in monolayer $MoTe_2$ at high magnetic fields. *Nano Lett.* **16 (6)**, 3624–3629 (2016).

[35] K. F. Mak, K. He, C. Lee, G. H. Lee, J. Hone, T. F. Heinz, J. Shan. Tightly bound trions in monolayer MoS_2. *Nat. Mater.* **12**, 207–211 (2013).

[36] W. Zhao, Z. Ghorannevis, L. Chu, M. Toh, C. Kloc, P. H. Tan, G. Eda. Evolution of electronic structure in atomically thin sheets of WS_2 and WSe_2. *ACS Nano* **7 (1)**, 791–797 (2013).

[37] L. M. Xie. Two-dimensional transition metal dichalcogenide alloys: preparation, characterization and applications. *Nanoscale* **7 (44)**, 18392–18401 (2015).

[38] N. Tit, I. M. Obaidat, H. Alawadhi. Origins of bandgap bowing in compound-semiconductor common-cation ternary alloys. *J. Phys.: Condens. Matter* **21 (7)**, 075802 (2009).

[39] A. Arora, K. Nogajewski, M. Molas, M. Koperski, M. Potemski. Exciton band structure in layered $MoSe_2$: from a monolayer to the bulk limit. *Nanoscale* **7 (48)**, 20769–20775 (2015).

Chapter 4

Optical investigation of temperature- and gate-voltage-dependent excitonic effects in monolayer $MoSe_2$

4.1 Introduction

In this study, we discuss in detail various modifications of the photoluminescence (PL) signal and its parameters in a transition metal dichalcogenide (TMDC) monolayer $MoSe_2$ under the influence of the carrier concentration and temperature variation.

The extensive investigations of the single-layer TMDC properties as functions of the charge density started a few years ago [1–10]. Such increasing attention is attributed to the intriguing characteristics and effects in these materials. Their reduced dimensionality, i. e. spatial confinement, causes the reduced and non-local dielectric screening, strong enhancement of the Coulomb interaction and giant bandgap renormalization [5, 11–18]. This results in the formation of tightly bound electron-hole pairs (excitons) with typical binding energies in the range of 0.2–0.5 eV [12–14, 18–21] which are more than an order of magnitude larger than those in the traditional III–V two-dimensional (2D) semiconductor quantum wells [22, 23]. Despite various differences in values of physical quantities, the TMDC monolayers demonstrate exciton physics similar to that in the GaAs and ZnSe quantum wells [24–27], so a comparison of optical properties between these systems is possible. Strongly bound excitons dominate the optical response and determine optical and charge-transport properties, including photoconduction and photocurrent generation [28–30]. In the single-layer TMDCs, these particles survive even at room temperature [2, 4, 31]. All the above discoveries give us an opportunity to study exciton and many-body interactions in a much wider range of temperatures and free-carrier densities relative to that for the conventional gated semiconductor quantum wells [29, 32–35].

In addition to ordinary bound electron-hole pairs, more complex exciton species also significantly influence the optoelectronic properties of the monolayer TMDCs. Charged three-particle states (trions) are most common and formed when neutral excitons interact with extra free carriers. A probability of the positive trion formation is often low, because unintentional doping in these materials is usually n-type [4, 36, 37]. The typical charged exciton binding energy is about 10 % of the exciton binding energy [38] which corresponds to a few tens of meV. Other interesting excitonic states are biexcitons (bound exciton-exciton pairs) which have been mostly observed in the single-layer WS_2 [8, 9, 39, 40]. Also, some excitonic species may recombine non-radiatively and thus they are optically dark. The existence of the dark excitons is theoretically and experimentally confirmed in the TMDC monolayers [15, 41–46].

The presence of electrically injected electrons and holes in the 2D TMDCs causes changes in the optical response by means of the following physical mechanisms: the elastic Coulomb scattering, Pauli blocking and screening of the Coulomb interaction [7]. The free-carrier-exciton (and trion) collisions contribute to the dephasing processes and broaden the peak widths [7, 9, 47, 48]. Rising of the Fermi level with the electron injection (doping) reduces the phase space for the electron scattering due to the Pauli exclusion and decreases the exciton binding energy owing to the screening [49–51]. As a consequence, the blueshift of the exciton transition energy is observed [2, 3, 8, 9, 16]. The corresponding trion energy is redshifted, because an ionized electron released after ionization of a trion is excited to a higher unoccupied state at the Fermi level. The electron-hole Coulomb attraction is screened with the electron doping; exchange and correlation interactions induce the shrinkage of the band gap [7, 29, 34, 35, 52]. The band-gap renormalization affects neutral exciton energies in molybdenum-based compounds, but this effect is negligible for the TMDC monolayers containing tungsten because of the different mechanism of the conduction-band spin-orbit coupling [41, 52]. Finally, disorder and thermalization suppress the screening of the Coulomb interaction [52].

Different types of defects and impurities as well as strain from the substrate result in the presence of disorder potential which is an origin of the localized states in the 2D TMDC materials [53] similar to the traditional semiconductor quantum wells, where the random potential arises from fluctuations in well width [54–56]. The certain deep potential traps may cause strong spatial localization of excitons and act as single photon emitters in some monolayers (for example, WSe_2) [57–59] with the pronounced redshift of the emission energy up to tens of meV below the trion transition. In other cases, excitons may be weakly localized and their transition energy is slightly redshifted relative to the PL from the delocalized states, resulting in the inhomogeneous broadening of the exciton resonance [53, 56, 60]. This energy difference between the localized and delocalized states defines a mobility edge [53–55, 61]. It is worth mentioning that trions are formed from the delocalized neutral excitons faster than from the localized ones [53]. Additionally, the trion dissociation energy is usually much higher than that of impurity-bound excitons [6]. The radiative lifetime of the localized excitons increases with the reducing localization length and can be almost three orders of magnitude larger than the average lifetime of the thermally distributed excitons at low temperatures [62, 63]. Takagahara [54] assumes a possibility of exciton moving between potential traps in the localized regime via phonon-assisted tunnelling in the conventional semiconductor quantum wells. In that scenario, the energy mismatch between the traps is compensated by absorption or emission of acoustic phonons. Also, the phonon-assisted transitions release excitons from the localized states. Due to the similarity of the systems as mentioned above, we can suggest the same behaviour of the localized excitons in the TMDC monolayers.

Temperature-related effects have an important impact on the optical properties in the TMDC atomic layers. The interactions with phonons define thermalization. The exciton scattering with acoustic phonons dominates at temperatures up to 50 K [60]. At higher temperatures, optical phonons become to involve in the collision processes. Overall, the acoustic and optical phonon contributions to the temperature-dependent exciton peak linewidth broadening are well understood in these ultrathin crystals [45, 46, 64–67]. Radiative recombination of the bright excitons induces the spectral peak widening which is invariable with the increase in temperature [67]. The exciton peak is mainly broadened with temperature growth through the non-radiative exciton–phonon scattering within the $\pm K$ valley of the hexagonal Brillouin zone (so-called intravalley scattering) in the molybdenum-based monolayers. In the single-layer tungsten-containing TMDCs, the temperature-dependent peak widening is attributed for the most part to the non-radiative intervalley scattering of the bright excitons with the dark states [67]. Additionally, it is established for the last-mentioned subkind of the materials that the integrated PL intensity of the exciton peak is gradually increased as a function of temperature owing to ‘brightening’ of the dark excitons [45]. However, a complex analysis of many-body interactions (through the behaviour of excitons) including changes in localization under the electrostatic doping with the system temperature rise has not been performed until now. Our work is aimed to solve this.

4.2 Sample preparation and experimental methods

We measure the gated monolayer $MoSe_2$ sample presented in Fig. 4.1 using photoluminescence (PL) spectroscopy.

The monolayer sheets in the above sample are produced by mechanical exfoliation

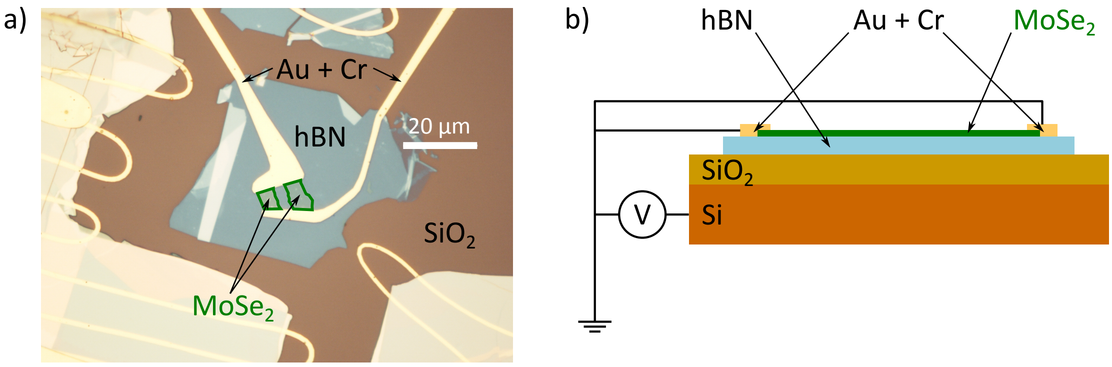

Fig. 4.1 The measured monolayer MoSe$_2$ sample. All materials are labelled with their chemical names. (a) An optical microscope image of the sample. The monolayer MoSe$_2$ flakes are bordered with green lines. (b) The sample's diagram.

followed by polymethyl methacrylate (PMMA) wet transfer. A detailed description of the exfoliation procedure and transfer method is given in subsection 2.1.1 and subsubsection 2.1.2.1. Before exfoliation of the MoSe$_2$ flakes, the 90 nm SiO$_2$/Si substrate for the sample is cleaned in acetone for 10 min, in isopropanol for 10 min, dried with N$_2$ gas, kept on a hot plate at 130 °C, and cooled for $\sim$ 20 sec. Then, the hexagonal boron nitride (hBN) crystals of several tens of nm thickness are cleaved onto the substrate using water soluble tape (Nitto tape) to make a flatter surface and hence provide stronger adhesion. A combination of dark- and bright-field microscopy allows to identify hBN crystals without terraces or contamination. Such crystals are suitable for exfoliation of the MoSe$_2$ thin films. When the monolayer flakes are on the necessary hBN surface, Cr/Au contacts are patterned by standard e-beam lithography described in subsection 2.1.4. The sample in Fig. 4.1 has been made in the University of Manchester by Dr. Freddie Withers.

Using fabricated contacts, we can apply the gate voltage V_g to the flakes as shown in Fig. 4.1b. The source-meter device used in the set-up is Keithley 2400. Our working V_g range in this study is from -10 V to +10 V with the step of 0.5 V for each measurement. The rising electron (hole) concentration in the sample occurs with the increasing (decreasing) V_g. During all experiments, the electric current from the I-V curves has varied in the range of $\sim$ +0.1–+0.7 nA.

The low-temperature micro-photoluminescence (μPL) technique presented in detail in subsubsection 2.2.1.3 is used for the measurements. The continuous flow

He cryostat is Oxford Instruments Microstat HiRes2.

4.3 Results

4.3.1 Photoluminescence in the low-temperature regime

This subsection presents data obtained from the PL measurements in the monolayer $MoSe_2$ at low temperatures (10–90 K) at which the inhomogeneous broadening of the spectral peaks and trion binding energy ($\sim$ 30 meV [4]) are larger than the thermal energy $k_B T$ where T is the temperature of the sample and k_B the Boltzmann constant. As examples, the displaced normalized PL spectra at three different temperatures (15 K, 50 K and 90 K) are demonstrated in Fig. 4.2a–c. All PL data are recorded with the V_g step of 0.5 V but Fig. 4.2a–c shows the spectra with difference of 1 V in V_g for clarity.

The emission consists of two peaks corresponding to a signal from neutral (A) and charged (A^*) excitons. Our monolayer $MoSe_2$ measured flake is n-doped because the initial PL spectra at $V_g = 0$ V do not show a clear A exciton peak but the prominent A^* one (Fig. 4.2). The neutral exciton PL rise is observed with the increasing hole concentration (when going to -10 V). The same behaviour was presented earlier in the monolayer TMDCs [2] but without a detailed analysis of the PL spectral parameters.

It is clearly visible that the excitonic peak positions are redshifted with temperature growth (Fig. 4.2 and Fig. 4.3e–f). This very typical evolution for semiconductors can be caused with the temperature effects, such as the lattice dilatation and increasing exciton-phonon coupling [4, 45, 46].

To evaluate the PL spectral parameters, namely the integrated PL intensities, full widths at half maxima (FWHM) and peak positions, all spectra are fitted with Lorentzians in this study. We illustrate the fittings of the spectra in Fig. 4.2d–f. The fitting parameters, specifically the gate-voltage-dependent linewidths, areas and peak positions of the A and A^* peaks at temperatures of 15 K, 50 K and 90 K for instance, are shown in Fig. 4.3. The standard errors of those parameters are mostly less than 1 % and their bars are not exceeded the size of the data points on the

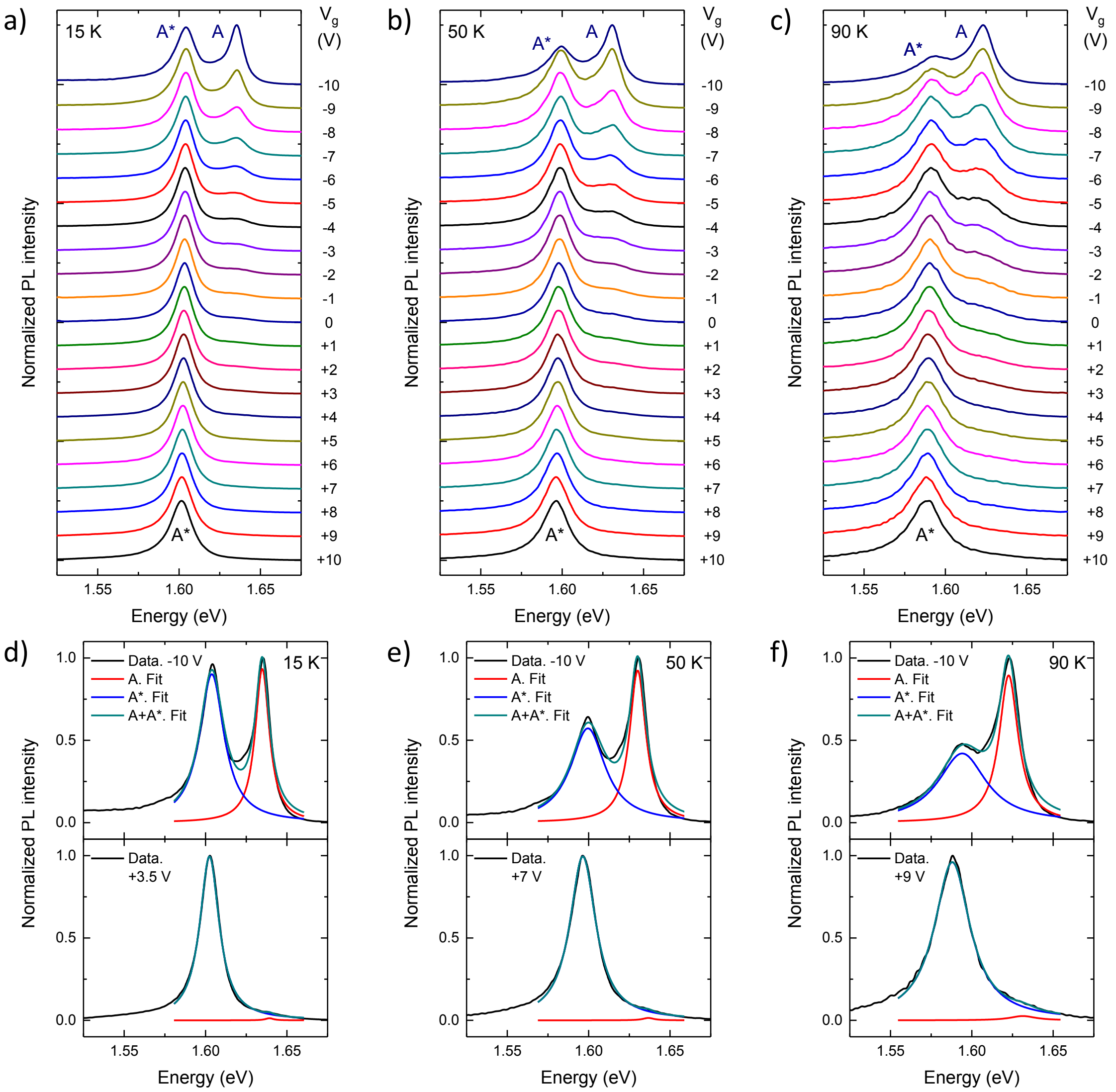

Fig. 4.2 Gate-voltage-dependent PL measurements of the monolayer $MoSe_2$ under 10 μW laser excitation at 2.33 eV and temperatures of (a), (d) 15 K, (b), (e) 50 K and (c), (f) 90 K. (a)-(c) Vertically stacked normalized PL spectra taken at the applied gate voltage V_g from -10 V to +10 V. The electron concentration is increased when going to +10 V. The V_g step for the depicted spectra is 1 V. A and A^* indicates peak positions for neutral and charged excitons, respectively. (d)-(f) The spectra with $V_g = -10$ V for each temperatures and +3.5 V for 15 K, +7 V for 50 K, +9 V for 90 K are chosen as examples of spectral fitting with two Lorentzians corresponding to the A (red curve) and A^* (blue curve) peaks. The dark cyan lines are cumulative fits. The spectra with the positive gate voltage values higher than those presented in (d)-(f) do not contain neutral exciton peak fits.

graphs. At high positive V_g, the neutral exciton peak is very weak and not fitted at some temperatures.

Both neutral A and charged A^* exciton peaks become broader with temperature rise due to an increase in populations of thermally excited excitonic states and other temperature effects (Fig. 4.3a–b). The corresponding FWHM of the above A and A^* peaks are almost equal to each other without the applied electrostatic gating. However, linewidth dependencies on the gate voltage values are different for excitons and trions. When going to either -10 V or +10 V, the trion peak broadens while neutral excitons emit the signal with sharper peak. These changes are more dramatic for the A^* peak with the increasing hole concentration. Interestingly, the maximum of FWHM for A and beginning of the dramatic broadening for A^* shift to higher V_g with the increase in temperature: -4.5 V at 15 K, -2.5 V at 50 K, 0 V at 90 K for A and -8 V at 15 K, -7 V at 50 K, -5.5 V at 90 K for A^*. All the above features of linewidth behaviour will be discussed in subsection 4.4.1.

Temperature-related changes in the PL signal cause significant reduction of the integrated intensity of each excitonic peak as well as the total emission when temperature grows (Fig. 4.3c–d). Such effect is a consequence of the increasing non-radiative recombination processes including the phonon involvement and formation of dark exciton states upon thermalization [45, 46]. In the monolayer MoSe$_2$, dark excitons have higher energy than bright ones because of the specific conduction-band spin-orbit coupling resulted in crossing of the spin-split bands [41]. Another issue concerned with heating is quenching of the trion peak area relative to exciton one (Fig. 4.2). The reason to observe this is fast breaking of more complicated trion bound states with thermal fluctuations and thus generation of simpler exciton states [2, 4, 45, 46]. The electrical doping brings conspicuous redistribution of charge carriers in k-space and this influences excitonic peak areas (Fig. 4.3c–d). The hole injection with negative V_g values simultaneously boosts the A exciton signal and reduces A^* charged exciton emission. However, the trion peak starts to show opposite behaviour and dramatically enlarges its integrated PL intensity at low V_g. The minimum of the A^* peak area shifts to higher gate voltage values with the

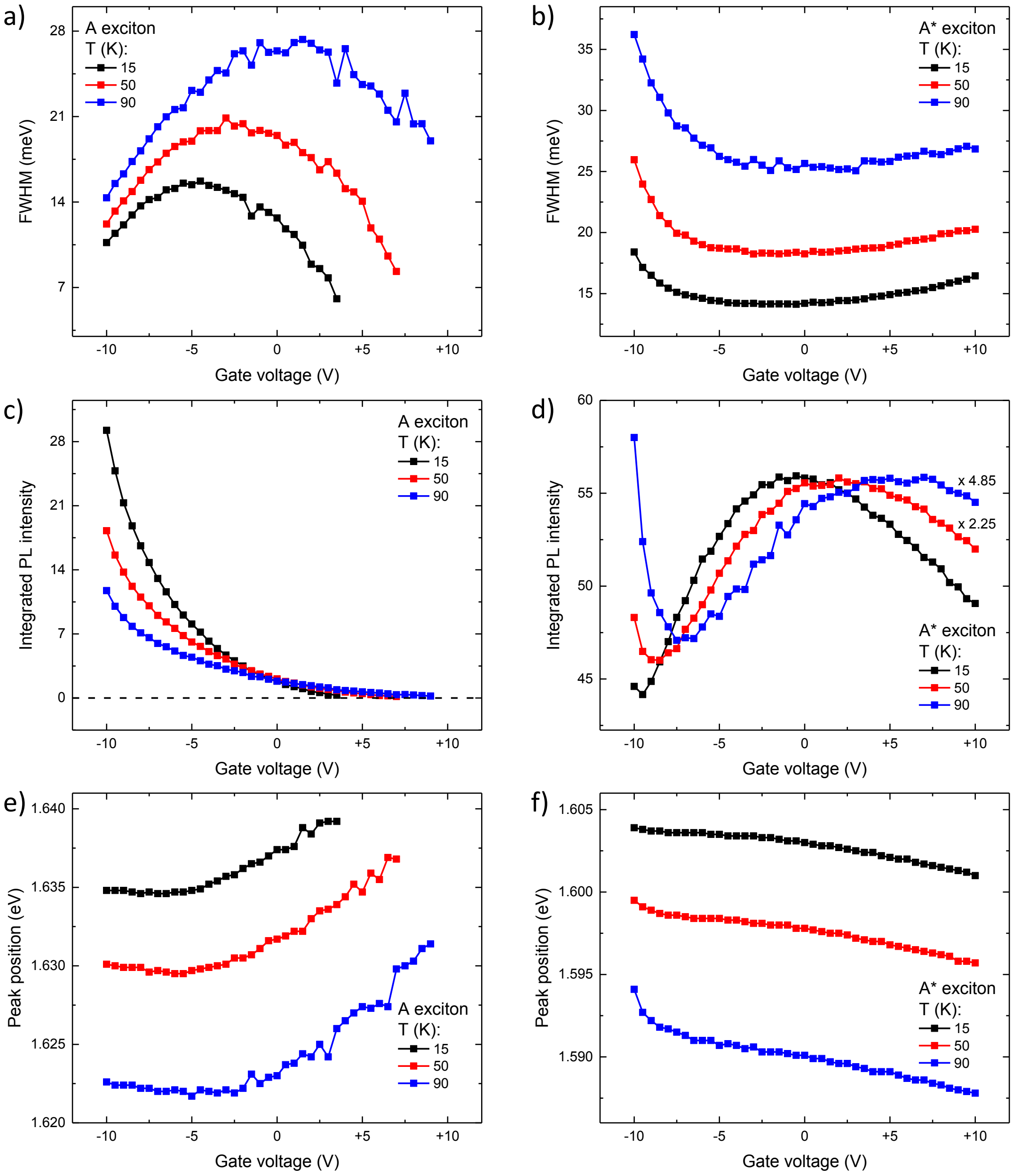

Fig. 4.3 Gate-voltage-dependent spectral parameters of the *A* (left column) and A^* (right column) peaks in the monolayer MoSe$_2$ at low temperatures. The data are compared at temperatures of 15 K (black), 50 K (red) and 90 K (blue). The spectral parameters are: (a)–(b) FWHM, (c)–(d) integrated PL intensities and (e)–(f) peak positions. The applied gate voltage: $-10\text{ V} \leq V_g \leq +10\text{ V}$. The electron concentration is increased when going to +10 V. (d) Dependencies of the A^* peak areas at 50 K (red) and 90 K (blue) are magnified for clarity.

increase in temperature: -9.5 V at 15 K, -8.5 V at 50 K and -7 V at 90 K. In other direction (the electron injection), the charged exciton peak area drops again so that the maximum of area values at $\mid V_g \mid \approx 0$ V is created. As the above minimum, this maximum is observed with bigger doped electron density when temperature rises: -1 V at 15 K, +1 V at 50 K and +5.5 V at 90 K. At $V_g > 0$ V, neutral exciton emission is very weak and almost negligible. It is worth mentioning that all gate-voltage-dependent variations in excitonic peak area values becomes smaller with growing temperature. Subsection 4.4.1 will present all explanations of the effects concerning changes in the integrated PL intensity of the signal with the electrostatic doping and temperature heating.

When V_g goes up to +10 V, the Fermi energy is increased with the electron injection into the measured system and the excitonic peak positions are varied by a few meV: the A emission energy is monotonically blueshifted (at $V_g > \sim -5$ V) while the A^* emission energy redshifted (Fig. 4.3e–f). The hole concentration since about $V_g = -5$ V almost does not affect neutral exciton peak position moving. The similar behaviour of the peak positions was observed earlier in both the monolayer TMDCs [2, 3, 8, 16, 52] and quantum wells [68–70], and can be explained as the influence of Pauli blocking and screening of the Coulomb interaction [7, 34, 49, 50, 52]. The band-gap renormalization weakens the shifts of the A peak positions with the injected gate-induced hole charge [52]. Minimal screening is likely to be at around $V_g = -5$ V due to the presence of initial unintentional doping in our sample. At low negative gate voltages, energy blueshift of the A^* peak positions is intensified with the rising hole concentration and this effect becomes to be more pronounced with temperature growth. We will present our suggestions why this happens in subsection 4.4.1.

4.3.2 Photoluminescence in the high-temperature regime

Here, we present the high-temperature PL data of the monolayer $MoSe_2$ (Fig. 4.4). These results contain some crucial differences in regard to those at low temperatures (subsection 4.3.1). $k_{\mathrm{B}}T$ becomes larger than the inhomogeneous broadening of the peaks and comparable to the trion binding energy. At three temperatures (230 K,

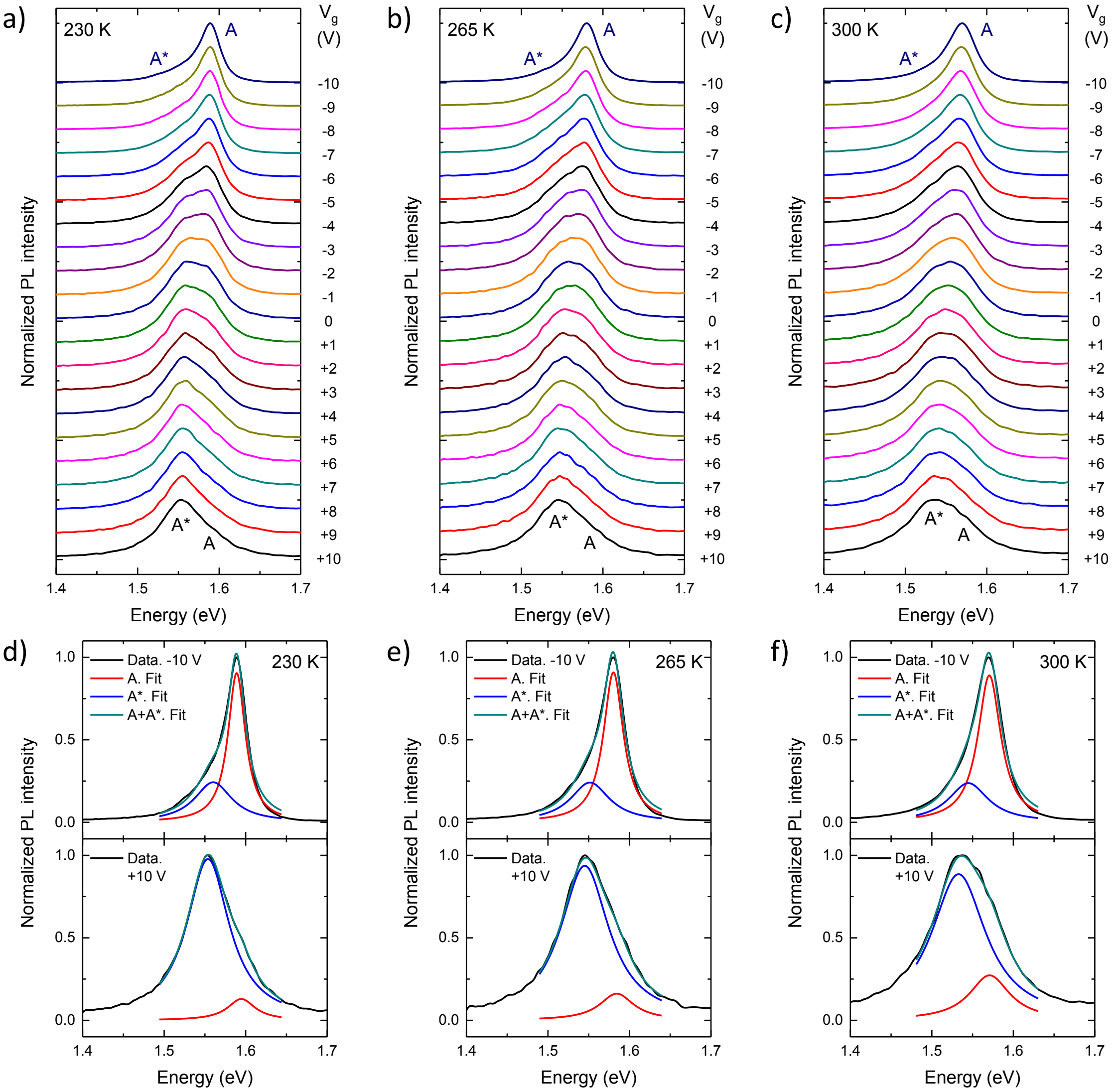

Fig. 4.4 Gate-voltage-dependent PL measurements of the monolayer $MoSe_2$ under 10 μW laser excitation at 2.33 eV and temperatures of (a), (d) 230 K, (b), (e) 265 K and (c), (f) 300 K. (a)-(c) Vertically stacked normalized PL spectra taken at the applied gate voltage V_g from -10 V to +10 V. The electron concentration is increased when going to +10 V. The V_g step for the depicted spectra is 1 V. A and A^* indicates peak positions for neutral and charged excitons, respectively. (d)-(f) The spectra with $V_g = \pm 10$ V for each temperatures are chosen as examples of spectral fitting with two Lorentzians corresponding to the A (red curve) and A^* (blue curve) peaks. The dark cyan lines are cumulative fits.

265 K and 300 K), spectra for the monolayer flake are obtained for a wide range of the applied gate voltage V_g. Fig. 4.4a–c shows those spectra with 1 V step for clarity (the experimental V_g step is equal to 0.5 V).

The PL signal still includes contributions from neutral A and charged A^* excitons described in section 4.1. These excitonic peaks are broad and not so distinct. Except the cases with low negative V_g values, emission mostly consists of the trion signal as the measured sample is n-doped. To extract the spectral parameters and make the above peaks more visual, the fitting with two Lorentzians are used. Fig. 4.4d–f demonstrates the fitting of the spectra at $V_g = \pm 10$ V as examples. In comparison with the low-temperature data in Fig. 4.2, the neutral exciton peaks are tuned stronger with the applied gate-induced hole doping because of thermal excitation from the trion states for the most part [2, 4, 45, 46]. Dependences of the spectral parameters (linewidths, areas and peak positions) on the applied gate voltage V_g are plotted in Fig. 4.5. The calculated standard error bars are smaller than the point size on the plots.

In contrast to the corresponding results at low temperatures, both exciton and trion peaks become more narrow with the hole injection from +10 V to -10 V (Fig. 4.5a–b). These FWHM changes are slightly bigger for A (18 meV at 230 K, 21 meV at 265 K, 26 meV at 300 K) than for A^* (8 meV at 230 K, 14 meV at 265 K, 24 meV at 300 K) and increase with heating due to the temperature effects and thermal neutral exciton excitation. The influence of the hole concentration on the peak widths will be discussed in subsection 4.4.1. The linewidth data for the A exciton peak at positive V_g are much dispersed owing to the weak signal.

The total emission area as well as the areas of each excitonic peak continue to drop with heating (Fig. 4.5c–d) because of temperature-related modifications explained in subsection 4.3.1. The integrated PL intensity of the neutral exciton peak has the same behaviour as the fuction of the applied gate voltage at both low and high temperatures: almost negligible values at $V_g \to +10$ V and dramatic growth at $V_g \to -10$ V. The charged exciton peak area shows little dependence on V_g (in accordance with [2]) down to -6 V, from where it rapidly rises. The explanations of

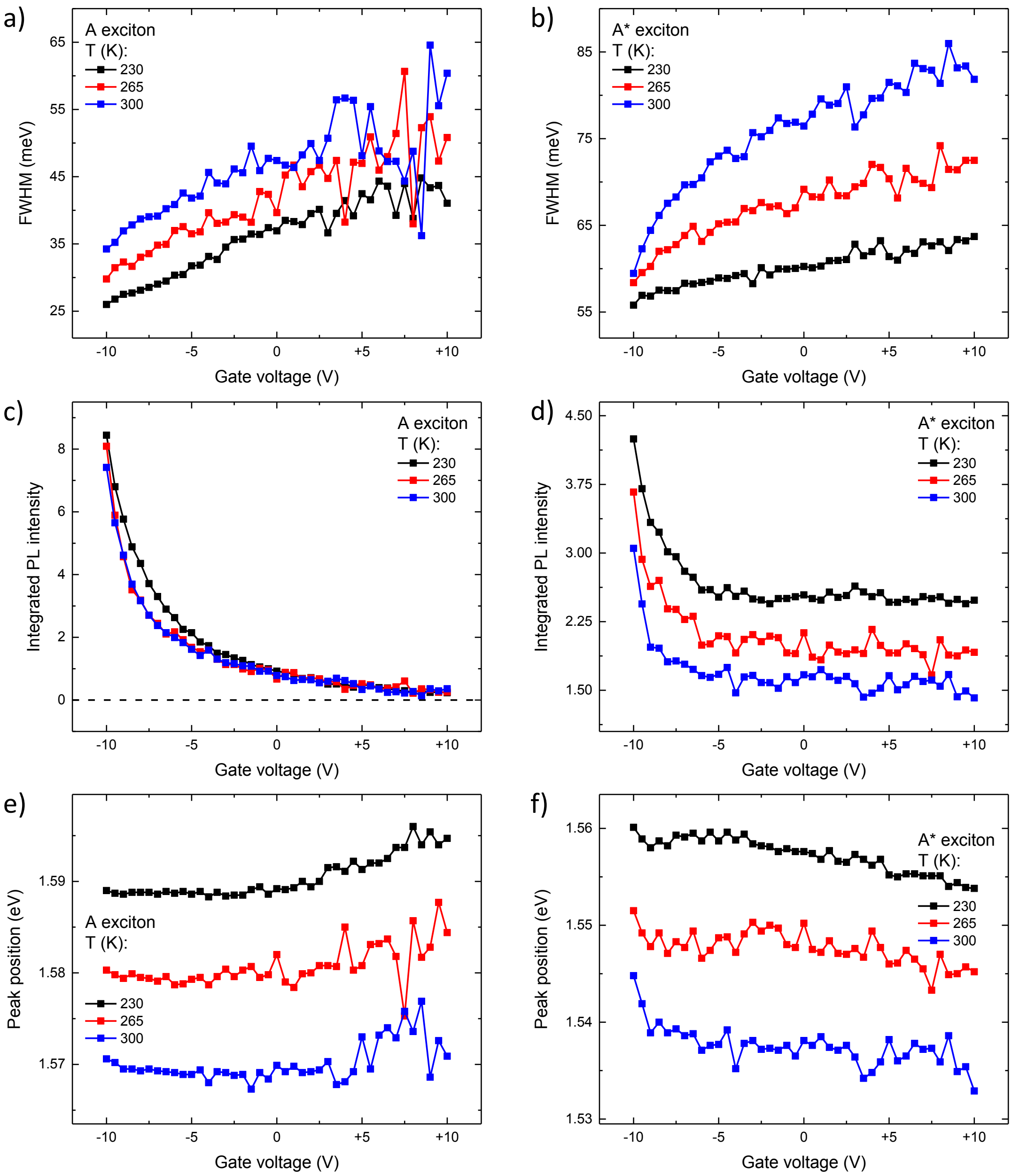

Fig. 4.5 Gate-voltage-dependent spectral parameters of the *A* (left column) and A^* (right column) peaks in the monolayer MoSe$_2$ at high temperatures. The data are compared at temperatures of 230 K (black), 265 K (red) and 300 K (blue). The spectral parameters are: (a)–(b) FWHM, (c)–(d) integrated PL intensities and (e)–(f) peak positions. The applied gate voltage: -10 V $\leq V_g \leq +10$ V. The electron concentration is increased when going to +10 V.

the above effects concerned with the electrostatic doping will be presented in detail in subsection 4.4.1.

The A and A^* peak positions (Fig. 4.5e–f) vary with the applied gate voltage in a similar way (except at the low negative V_g for A^*) as their corresponding low-temperature values (Fig. 4.3e–f). When $V_g \to -10$ V, stronger energy blueshift of the A^* peak positions almost does not appear owing to the temperature effects. All peak positions are also energetically redshifted with the increase in temperature due to the lattice dilatation and growing exciton-phonon scattering [4, 45, 46].

4.3.3 Photoluminescence in the intermediate-temperature regime

At temperatures of 110–200 K, the thermal energy is on the order of the inhomogeneous spectral peak widening and lower than the binding energy of charged excitons. The data of the intermediate temperature range are presented in this subsection. Fig. 4.6 demonstrates the normalized PL spectra at three temperatures (130 K, 175 K and 200 K) and different carrier concentration caused by the applied gate voltage V_g. The depicted V_g step equals 1 V to avoid a mess in data presenting (our experiments are measured with 0.5 V step).

Both neutral A and charged A^* exciton peaks are fitted with two Lorentzians as shown for the spectra at $V_g = \pm 10$ V as examples (Fig. 4.6d–f). The obtained fitting parameters, such as linewidths, areas and peak positions, are plotted in Fig. 4.7 as functions of applied V_g without standard error bars (they are less than the point size on the graphs).

Similarly to the data presented in subsections 4.3.1 and 4.3.2, the heating-related linewidth broadening of the excitonic peaks is also observed in the monolayer MoSe$_2$ at temperatures of 110–200 K (Fig. 4.7a–b). For the neutral exciton peak (Fig. 4.7a), the high electron concentration does not decrease the peak width sufficiently and the FWHM behaviour is similar to that at high temperatures (Fig. 4.5a). More important changes occur in the FWHM of the A^* peak (Fig. 4.7b). Its strong widening caused by the hole injection at $V_g \to -10$ V significantly weakens and

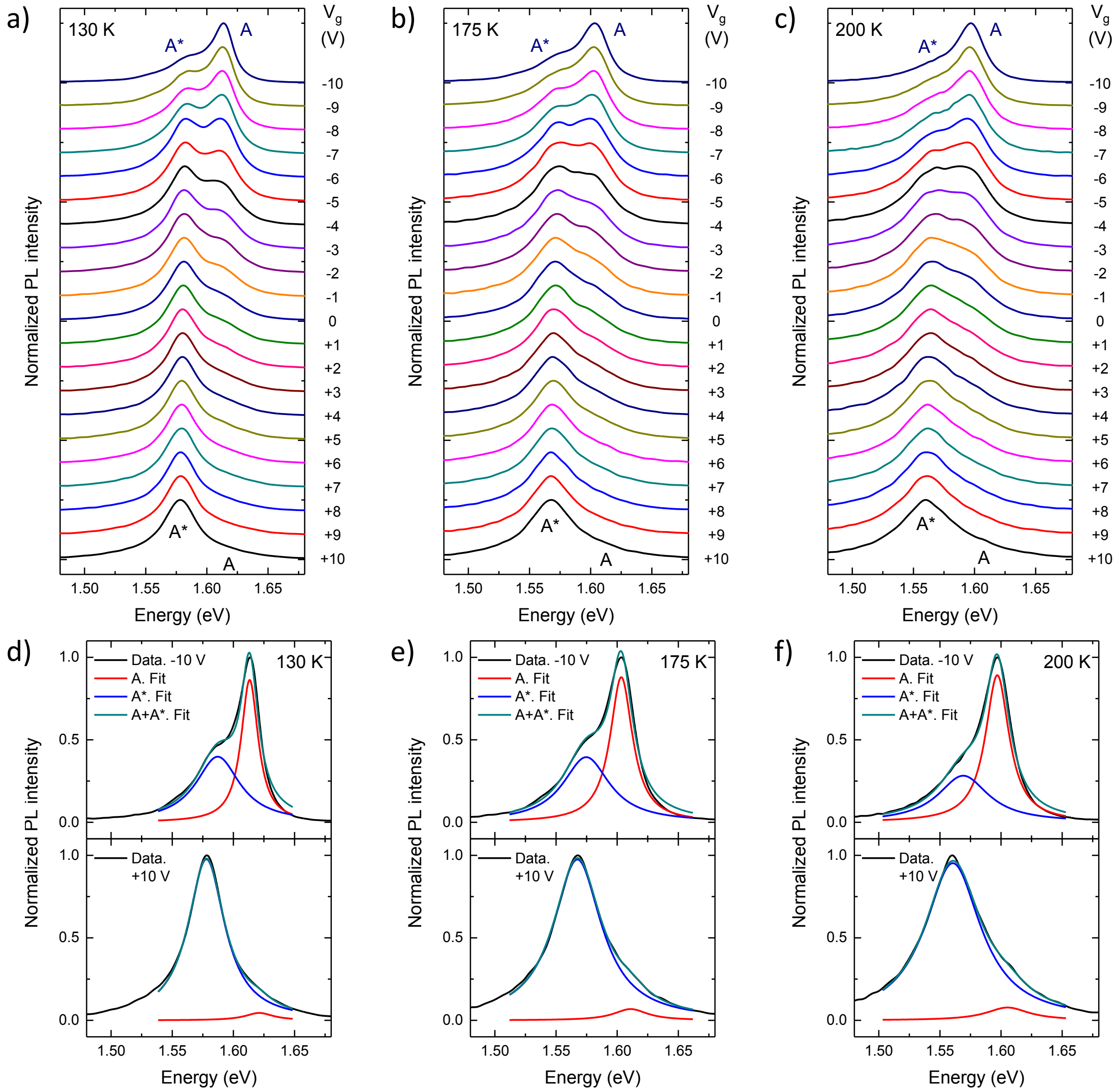

Fig. 4.6 Gate-voltage-dependent PL measurements of the monolayer MoSe$_2$ under 10 μW laser excitation at 2.33 eV and temperatures of (a), (d) 130 K, (b), (e) 175 K and (c), (f) 200 K. (a)-(c) Vertically stacked normalized PL spectra taken at the applied gate voltage V_g from -10 V to +10 V. The electron concentration is increased when going to +10 V. The V_g step for the depicted spectra is 1 V. A and A^* indicates peak positions for neutral and charged excitons, respectively. (d)-(f) The spectra with $V_g = \pm 10$ V for each temperatures are chosen as examples of spectral fitting with two Lorentzians corresponding to the A (red curve) and A^* (blue curve) peaks. The dark cyan lines are cumulative fits.

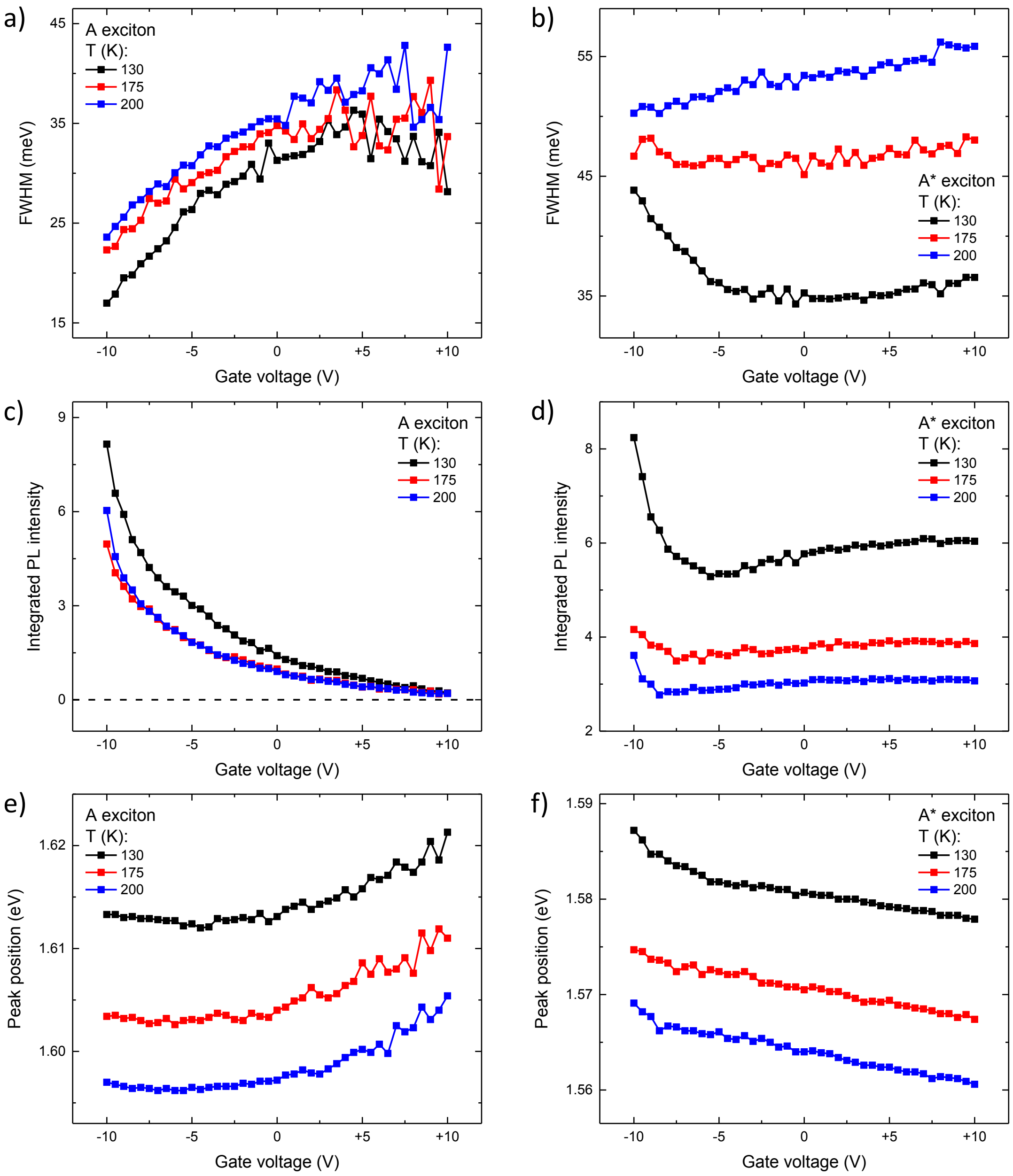

Fig. 4.7 Gate-voltage-dependent spectral parameters of the A (left column) and A^* (right column) peaks in the monolayer MoSe$_2$ at intermediate temperatures. The data are compared at temperatures of 130 K (black), 175 K (red) and 200 K (blue). The spectral parameters are: (a)–(b) FWHM, (c)–(d) integrated PL intensities and (e)–(f) peak positions. The applied gate voltage: $-10\text{ V} \leq V_g \leq +10\text{ V}$. The electron concentration is increased when going to +10 V.

whole dependence on the gate voltage becomes flatter with temperature growth at 110–175 K. At 200 K, the trion peak linewidth tends to decrease under applied V_g from +10 V to -10 V as in the case of the high-temperature results (Fig. 4.5b). All the above-mentioned effects will be considered in subsection 4.4.1.

The integrated intensity of the whole PL signal and specifically each excitonic peak also quench with heating (Fig. 4.7c–d) as those described in previous subsections 4.3.1 and 4.3.2. The only exception is almost the similar area values (even slight increasing at low negative V_g) for the A peak when going from 175 K to 200 K (Fig. 4.7c). Such effect is supposed to happen due to the temperature-related transition of the system conditions, which we clearly observe in the A^* peak linewidth in Fig. 4.7b. On the whole, the neutral exciton peak integrated intensity at 110–200 K depends on applied V_g in the same way as at other temperatures. The concave shape of the dependence of the trion peak area values on the gate voltage from +10 V to $\sim$ -5 V at low temperatures (Fig. 4.5d) gradually becomes flatter with the increase in temperature and is almost negligible from 150 K. The strong A^* peak enhancement at $V_g \to -10$ V occurs in the whole range of temperatures. The nature of all area dependencies will be discussed in subsection 4.4.1.

Except at the low negative V_g for A^*, the excitonic peak positions of the intermediate temperature range (Fig. 4.7e–f) follow the same temperature- and gate-voltage-dependent trends represented in subsections 4.3.1 and 4.3.2. Observed at low temperatures when $V_g \to -10$ V (Fig. 4.3f), the more dramatic blueshift of the trion peak positions weakens from 130 K to 175 K and disappears at temperatures of 175–300 K because of the temperature effects.

4.3.4 Temperature dependence of spectral parameters

Previous subsections 4.3.1–4.3.3 mostly describe dependencies of all fitting parameters taken from PL spectra on the applied gate voltage V_g. Here, we present an evolution of those spectral parameters (FWHM, integrated PL intensities and peak positions) only with temperature. Data at the applied gate voltages of -10 V, -5 V, 0 V and +10 V are compared in Fig. 4.8. The PL signal of the neutral exciton peak at

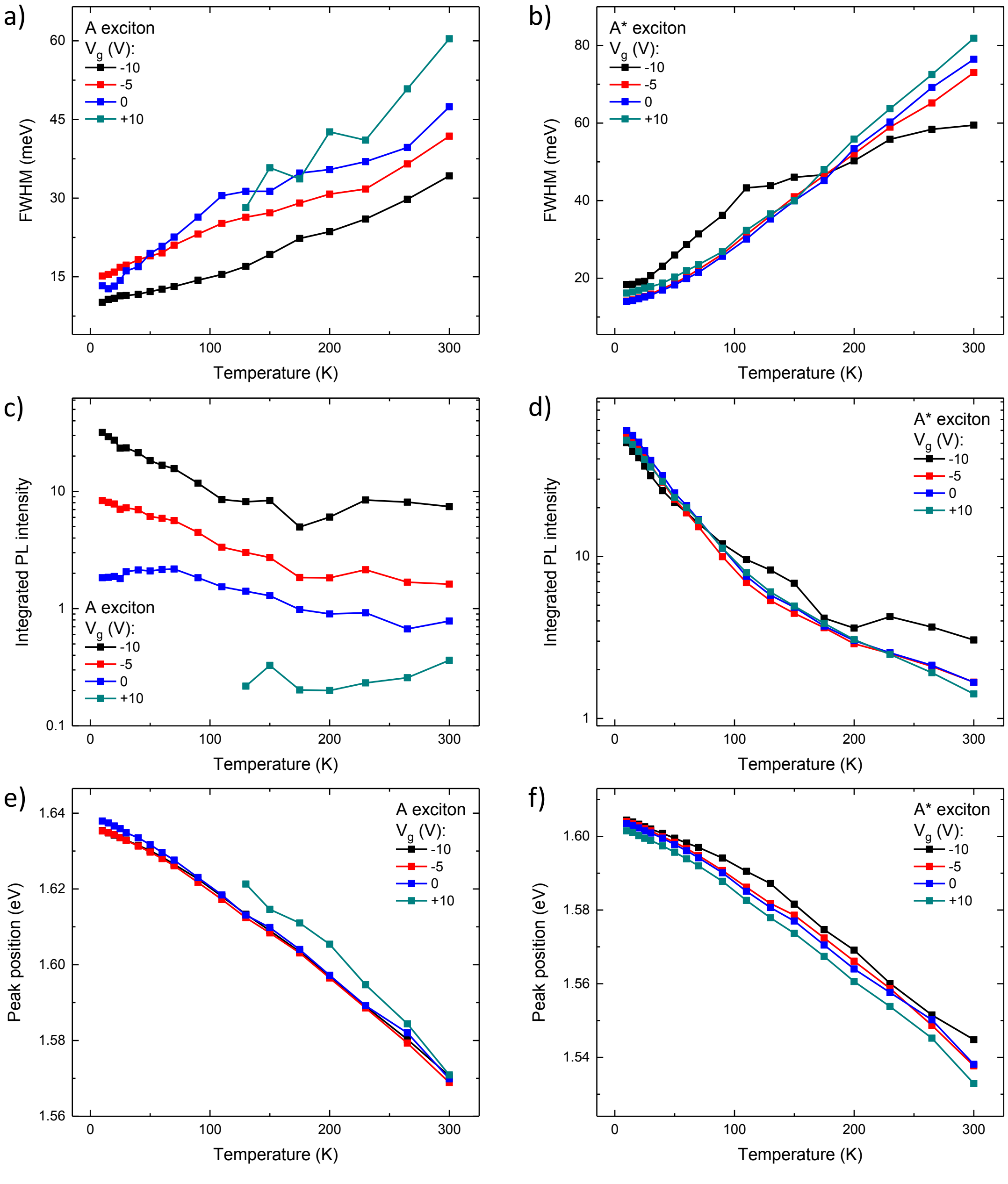

Fig. 4.8 Temperature-dependent spectral parameters of the *A* (left column) and A^* (right column) peaks in the monolayer $MoSe_2$ under 10 μW laser excitation at 2.33 eV. The data are compared at the gate voltages V_g of -10 V (black), -5 V (red), 0 V (blue) and +10 V (dark cyan). The spectral parameters are: (a)–(b) FWHM, (c)–(d) integrated PL intensities and (e)–(f) peak positions. The temperature range is 10–300 K.

$V_g = +10$ V value is negligible up to 130 K. Then for 130–300 K, it remains very weak and noisy which results in the strong noise in the presented data.

The linewidth broadening of both A and A^* peaks occurs with temperature growth (Fig. 4.8a–b) mainly owing to the temperature effects and influence of thermally excited excitonic states. Two types of the dependencies of the peak widths are observed: with (we denote as type ▲) and without (type △) a pronounced kink at 110 K. The type ▲ is activated when V_g goes to 0 V for A and -10 V for A^*. In this case, FWHM enlarges much faster than that for the type △ up to 110 K. Then at higher temperatures, the slope of linewidth growth is reduced. The type-△ FWHM broadening is happened for all other V_g values. Interestingly, the sublinear type-△ trend for the neutral exciton peak is parallel shifted with the varying gate voltage in opposite to that for the trion peak. The explanations of type-△ and type-▲ temperature dependencies will be viewed in subsection 4.4.2. The trend at $V_g = +10$ V for the A peak linewidth is straggling and difficult to analyse due to its weak peak signal.

On the whole excluding again the poor and noisy signal of the neutral exciton peak at +10 V, the integrated PL intensities of both A and A^* peaks quench with heating (Fig. 4.8c–d) as described in subsection 4.3.1. The other exception is a case at $V_g \to -10$ V and temperatures of 110–230 K when one temperature-related regime is transitioned to another one (subsection 4.3.3). At these system conditions, the increase in temperature causes some peak area fluctuations (especially for the A exciton peak). The influence of injected holes on our n-doped monolayer $MoSe_2$ flake significantly raises the integrated PL intensity of the neutral exciton peak and changes the shape of temperature-dependent curve of the charged exciton peak area values due to the recharging processes (subsection 4.4.1). Bigger electron injection into the system makes temperature dependence of the A^* peak integrated intensities more sublinear in a logarithmic scale and this curve slightly changes its slope at ~ 110 K because of the impact of the decreasing localization effect (subsection 4.4.2).

The peak positions of the neutral and charged exciton peaks show energy redshifts (Fig. 4.8e–f) as mentioned in subsection 4.3.1. Their temperature-dependent curves well correspond to the relations given by the Varshni [71] or O'Donnell *et al.* [72] formulae. Additionally, the peak positions are shifted under applied V_g as also taken into account in subsection 4.3.1. The shifts start to be significant at $V_g > -5$ V for the A peak while the charge exciton peak gradually changes its position on the whole range of the electrical doping. The difference in the trion peak positions at -10 V and +10 V rises up to 130 K and then declines owing to the recharging and temperature effects (section 4.4). Weak signals and big noise distort all peak position trends at high temperatures (230–300 K).

4.4 Discussion

The PL signal modifications in the monolayer $MoSe_2$ with gate voltage and temperature can be described by the presence of many-body interactions and disorder potential. This section will explain the influence of such interactions on the excitonic emission in detail.

4.4.1 Effects of localization, Coulomb scattering and trion recharging

As discussed in section 4.1, exciton localization significantly contributes to the spectral parameters of the PL signal in the 2D TMDCs, in particular in the monolayer $MoSe_2$. The 'mobility edge' effect separates the delocalized and localized states [53, 55, 61]. Since our monolayer $MoSe_2$ sample is initially n-doped, the neutral exciton quantity is small and the influence of localization effects on the A peak is pronounced at low temperatures. Because the temperature effects and phonon scattering are able to raise the energy of localized excitons above the mobility edge, we consider the importance of localization processes up to 110 K, when the thermal energy becomes comparable with a typical inhomogeneous excitonic peak widening ($\sim$ 10–15 meV). The free-carrier injection with the applied gate voltage increases the exciton-free-carrier scattering, screening of the Coulomb interaction [7, 34, 49, 50, 52] which damage localization. This is clear in Fig. 4.3a: the A peak linewidth broadening caused by exciton localization [53] disappears with the electrostatic gating approaching +10 V and -10 V. However in the low-temperature regime, the maximum of the FWHM for A is observed at the negative gate voltages (for example, it is about 16 meV at $V_g = -4.5$ V for 10 K). We suggest that the original n-type doping of the monolayer $MoSe_2$ flake provides this shift. Heating moves the FWHM maximum to 0 V because of the increasing temperature effects and therefore faster suppression of the sample doping.

By reason of primarily bigger trion concentration in the sample (thus, less percentage of the localized trion states relative to the total amount of charged exctions) and more difficult trapping of trions (three-particle complexes) with regard to excitons (two-particle complexes) by means of defects and impurities, the localization phenomena are not so much visible for the A^* peak at low temperatures except the cases of the high hole concentration at $V_g \to -10$ V.

When holes are injected into the system at low temperatures, more and more neutral excitons are formed. This is confirmed by the dramatic enhancement of the A peak area and corresponding decline of the A^* peak area at $V_g \to -10$ V (Fig. 4.3c–d). The high hole concentration at $V_g < \sim -7$ V launches the recharging processes when some part of neutral excitons begin to interact with extra free holes forming positive trions. An abrupt jump of the integrated PL intensity of the trion peak, its drastic peak position blueshift and pronounced FWHM increase due to the influence of localization (Fig. 4.3b,d,f) are convincing evidences of the recharging effect. Temperature growth activates all described processes at less hole injected densities.

When the electron concentration is big at low temperatures, the A^* peak widening is supposed to be caused by the impact of the charged-exciton-electron scattering (Fig. 4.3b). It is worth noting that the exciton-free-carrier collisions are known to be 8–10 times stronger than the exciton-exciton collisions in the GaAs single quantum wells [47, 48]. Also, the exciton-to-trion formation processes are insignificant owing to the small concentration of neutral excitons at $V_g \to +10$ V (Fig. 4.3c). Consequently at that system condition, we do not consider any important contribution of the trion-

trion and trion-exciton interactions to the above A^* peak linewidth broadening. Such electron injection lifts the Fermi level and the electrons released after the charged exciton recombination face with difficulty to find the unoccupied states in the band. This increases the average trion lifetime [63] and the A^* peak integrated intensity is quenched (Fig. 4.3d). However, temperature effects and phonon involvement destroy the above area dropping with heating.

At high temperatures (Fig. 4.5), both excitonic peaks are delocalized and hence broaden from -10 V to +10 V due to electron-exciton (trion) collisions [7, 9, 47, 48]. The recharging processes continue to exist as seen in Fig. 4.5c-d where the integrated intensities of the A and A^* peaks prominently rise at $V_g \to -10$ V.

4.4.2 Temperature-related effects and estimation of exciton-phonon interactions

The temperature-activated modifications of excitonic peaks are attributed to the phonon interactions. It was established in the monolayer TMDCs [60] and semiconductor quantum wells [64, 65, 73, 74] that the acoustic phonon scattering dominates at low temperatures. Additionally, localization has a sufficient impact on the spectral linewidth broadening at some charge carrier concentration as discussed in the previous subsection. Both the localized and delocalized excitonic states are influenced by acoustic phonons in the low-temperature regime [54]. Roughly above 110 K, optical phonons start to play an important role in all spectral changes [64, 67, 74]. They gradually destroy the localized states in the intermediate temperature range (110–200 K). Finally at higher temperatures, the localization effects are negligible.

Depending on the electrical doping, excitons (or trions) are for the most part localized or delocalized, resulting in the type ▲ or type △ of the temperature-dependent FWHM curves, respectively (subsection 4.3.4, Fig. 4.8a–b).

As mentioned in section 4.1, temperature dependence of the neutral exciton peak linewidth is well understood in both single-layer TMDCs [45, 46, 66, 67] and III–V quantum wells [64, 65] and can be given by

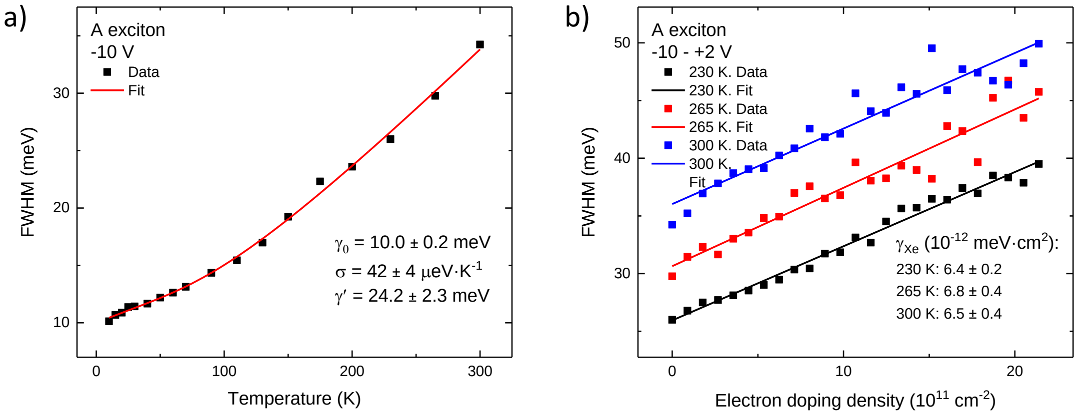

Fig. 4.9 Analysis of exciton-phonon and exciton-electron interactions. (a) The fitting of the temperature-dependent FWHM values of the neutral exciton peak at $V_g = -10$ V using the relation in Eq. (4.1). The extracted fitting parameters γ_0, σ and γ' are demonstrated. (b) The A peak linewidth values and their linear fits as functions of the gate-induced electron doping density described in the text. The data are taken at the gate voltages $-10\text{ V} \leq V_g \leq +2$ V and temperatures of 230 K (black), 265 K (red), 300 K (blue). The exciton-electron interaction parameter γ_{Xe} values obtained from the fitting are also presented.

$$\gamma(T) = \gamma_0 + \sigma T + \gamma' \frac{1}{e^{\hbar\omega/k_{\mathrm{B}}T} - 1}, \tag{4.1}$$

where γ_0 is the broadening at zero temperature (0 K), σ and γ' are respectively parameters of the linear term of the acoustic phonon contribution and the last term corresponded to thermal activation of optical phonons with an averaged energy $\hbar\omega$ taken to be equal to 30 meV in the monolayer MoSe$_2$ [46, 67, 75, 76]. The relation in Eq. (4.1) does not include the localization effects and thus is not expected to be accurate for the low-temperature range. Nevertheless at $V_g = -10$ V, localization is relatively unimportant (subsection 4.4.1) and Eq. (4.1) describes the linewidth broadening well as shown in Fig. 4.9a. The obtained parameters $\gamma_0 = 10.0 \pm 0.2$ meV, $\sigma = 42 \pm 4$ μeV·K^{-1} and $\gamma' = 24.2 \pm 2.3$ meV are in agreement with previous published results [46, 66, 67]. Hence, we can conclude that for delocalized neutral excitons in the single MoSe$_2$ layer, only the phonon-related contributions cause the increase in FWHM with temperature growth.

4.4.3 Estimation of exciton-electron interaction

Here, we also numerically evaluate the exciton-electron interaction. At high temperatures (230–300 K), almost the linear A peak widening is observed from -10 V to +2 V (Fig. 4.5a). In this case, neutral excitons are delocalized and do not participate in the trion formation, because the A^* peak area remains unchanged with the varied electron concentration (Fig. 4.5d) except at low negative V_g when the recharging processes occur (subsection 4.4.1). In addition, the number of excitons decreases with the electron injection into the measured system (Fig. 4.5c). Also, the non-radiative scattering including the phonon-assisted one should not vary too much at fixed temperatures. We can suggest that the exciton-exciton and exciton-trion interactions negligibly influence the A peak broadening in that range of gate voltages. Only the exciton-electron collisions lead to the spectral peak widening of the exciton transitions. At higher electron doping densities, the data in Fig. 4.5a are noisy and screening of the Coulomb interaction may induce some modifications in the scattering of excitons.

On the one hand, an inhomogeneity in the excitonic peak linewidth broadening is the consequence of the localization effects and presence of disorder potential [53, 60]. But on the other hand, thermalization delocalize excitons. Therefore, our experimental FWHM of the A peak is considered to be changed in the same way as the homogeneous linewidth with the electron doping (from -10 V to +2 V) at fixed high temperatures. Following a similar study of the homogeneous linewidth of the exciton peak in GaAs single quantum wells [48], the electron-doping-dependent A peak widening $\gamma(N_e)$ has a linear form

$$\gamma(N_e) = \gamma_0' + \gamma_{Xe} N_e, \tag{4.2}$$

where γ_0' is the initial broadening without doping, γ_{Xe} the exciton-electron interaction parameter. According to [52], the density of injected electrons N_e in our sample can be calculated as a function of the applied gate voltage V_g by

$$N_e = \frac{\varepsilon_0}{e(\frac{d_{\mathrm{hBN}}}{\varepsilon_{\mathrm{hBN}}} + \frac{d_{\mathrm{SiO_2}}}{\varepsilon_{\mathrm{SiO_2}}})}(V_g - V_g^0). \tag{4.3}$$

$V_g^0 = -10$ V, ε_0 is the vacuum permittivity, e the elementary charge, $\varepsilon_{\mathrm{hBN}} = 5.06$ [77] and $d_{\mathrm{hBN}} \approx 40$ nm ($\varepsilon_{\mathrm{SiO_2}} = 3.9$ and $d_{\mathrm{SiO_2}} = 90$ nm) respectively the relative dielectric constant and thickness of the hBN (SiO_2) layer. $\Delta V_g = V_g - V_g^0 = 1$ V corresponds to a doping density of 1.8×10^{11} cm^{-2}.

The results of the fitting are depicted in Fig. 4.9b. It is clearly visible that the parameter γ_{Xe}, which is the slope of the linear fits, almost does not change with temperature and fluctuates in a range of 6.4–6.8 $\times\, 10^{-12}$ meV·cm^2. The invariance of this parameter in the high-temperature regime confirms that only the scattering of excitons with electrons is estimated and no other interactions contribute to the exciton peak widening in that range of the electron doping. For other measured temperatures (10–200 K), the distinct non-linear dependence of $\gamma(N_e)$ is observed owing to the significant impact of the localized excitonic states.

A similar exciton–exciton interaction parameter γ_{XX} has been evaluated for WSe_2 monolayers and equal to $\sim 2.7 \times 10^{-12}$ meV·cm^2 [60]. It is about 2.5 times less than our γ_{Xe}. The appropriate parameter γ_{XX} for $MoSe_2$ atomic layer has not been found in research articles. Interestingly, the exciton-free-carrier interaction is 8–10 times more efficient than the exciton-exciton scattering in the conventional semiconductor quantum wells [47, 48]. Further investigations are needed to better understand the exciton-related interactions in the 2D TMDCs.

4.5 Conclusions

We investigate the PL of neutral and charged excitons of a monolayer $MoSe_2$ in a wide range of temperature and gate voltage influencing the carrier concentration. This is the first such detailed analysis of the spectral parameters of the excitonic peaks among the single-layer TMDCs covering such wide parameter space. The influence of localization and recharging processes is established and studied. We show that localization can be suppressed and controlled by the electrical charge doping and is not significant above 110 K. The contributions of acoustic and optical phonons to the exciton peak linewidth broadening are deduced. The estimation of the exciton-electron scattering is performed for the first time. Our results are compared with the similar previous investigations of the monolayer TMDCs and semiconductor quantum wells. The study of the peak parameters of excitons and trions, namely linewidth, integrated PL intensity and peak position, gives us more knowledge about many-body interactions in 2D semiconductors. Such knowledge could be very useful for novel device applications in optoelectronics.

References

[1] J. T. Ye, Y. J. Zhang, R. Akashi, M. S. Bahramy, R. Arita, Y. Iwasa. Superconducting dome in a gate-tuned band insulator. *Science* **338 (6111)**, 1193–1196 (2012).

[2] K. F. Mak, K. He, C. Lee, G. H. Lee, J. Hone, T. F. Heinz, J. Shan. Tightly bound trions in monolayer MoS_2. *Nat. Mater.* **12**, 207–211 (2013).

[3] A. M. Jones, H. Yu, N. J. Ghimire, S. Wu, G. Aivazian, J. S. Ross, B. Zhao, J. Yan, D. G. Mandrus, D. Xiao, W. Yao, X. Xu. Optical generation of excitonic valley coherence in monolayer WSe_2. *Nat. Nanotechnol.* **8**, 634–638 (2013).

[4] J. S. Ross, S. Wu, H. Yu, N. J. Ghimire, A. M. Jones, G. Aivazian, J. Yan, D. G. Mandrus, D. Xiao, W. Yao, X. Xu. Electrical control of neutral and charged excitons in a monolayer semiconductor. *Nat. Commun.* **4**, 1474 (2013).

[5] M. M. Ugeda, A. J. Bradley, S.-F. Shi, F. H. da Jornada, Y. Zhang, D. Y. Qiu, W. Ruan, S.-K. Mo, Z. Hussain, Z.-X. Shen, F. Wang, S. G. Louie, M. F. Crommie. Giant bandgap renormalization and excitonic effects in a monolayer transition metal dichalcogenide semiconductor. *Nat. Mater.* **13**, 1091–1095 (2014).

[6] B. Ganchev, N. Drummond, I. Aleiner, V. Fal'ko. Three-particle complexes in two-dimensional semiconductors. *Phys. Rev. Lett.* **114 (10)**, 107401 (2015).

[7] A. Chernikov, A. M. van der Zande, H. M. Hill, A. F. Rigosi, A. Velauthapillai, J. Hone, T. F. Heinz. Electrical tuning of exciton binding energies in monolayer WS_2. *Phys. Rev. Lett.* **115 (12)**, 126802 (2015).

[8] G. Plechinger, P. Nagler, J. Kraus, N. Paradiso, C. Strunk, C. Schüller, T. Korn. Identification of excitons, trions and biexcitons in single-layer WS_2. *Phys. Status Solidi Rapid Res. Lett.* **9 (8)**, 457–461 (2015).

[9] J. Shang, X. Shen, C. Cong, N. Peimyoo, B. Cao, M. Eginligil, T. Yu. Observation of excitonic fine structure in a 2D transition-metal dichalcogenide semiconductor. *ACS Nano* **9 (1)**, 647–655 (2015).

[10] A. M. Jones, H. Yu, J. R. Schaibley, J. Yan, D. G. Mandrus, T. Taniguchi, K. Watanabe, H. Dery, W. Yao, X. Xu. Excitonic luminescence upconversion in a two-dimensional semiconductor. *Nat. Phys.* **12**, 323–327 (2016).

[11] P. Cudazzo, I. V. Tokatly, A. Rubio. Dielectric screening in two-dimensional insulators: implications for excitonic and impurity states in graphane. *Phys. Rev. B* **84 (8)**, 085406 (2011).

[12] D. Y. Qiu, F. H. da Jornada, S. G. Louie. Optical spectrum of MoS_2: many-body effects and diversity of exciton states. *Phys. Rev. Lett.* **111 (21)**, 216805 (2013).

[13] K. He, N. Kumar, L. Zhao, Z. Wang, K. F. Mak, H. Zhao, J. Shan. Tightly bound excitons in monolayer WSe_2. *Phys. Rev. Lett.* **113 (2)**, 026803 (2014).

[14] A. Chernikov, T. C. Berkelbach, H. M. Hill, A. Rigosi, Y. Li, O. B. Aslan, D. R. Reichman, M. S. Hybertsen, T. F. Heinz. Exciton binding energy and nonhydrogenic Rydberg series in monolayer WS_2. *Phys. Rev. Lett.* **113 (7)**, 076802 (2014).

[15] Z. Ye, T. Cao, K. O'Brien, H. Zhu, X. Yin, Y. Wang, S. G. Louie, X. Zhang. Probing excitonic dark states in single-layer tungsten disulphide. *Nature* **513**, 214–218 (2014).

[16] B. Zhu, X. Chen, X. Cui. Exciton binding energy of monolayer WS_2. *Sci. Rep.* **5**, 9218 (2015).

[17] T. Stroucken, S. W. Koch. Optically bright *p*-excitons indicating strong Coulomb coupling in transition-metal dichalcogenides. *J. Phys. Condens. Matter* **27 (34)**, 345003 (2015).

[18] G. Wang, X. Marie, I. Gerber, T. Amand, D. Lagarde, L. Bouet, M. Vidal, A. Balocchi, B. Urbaszek. Giant enhancement of the optical second-harmonic emission of WSe_2 monolayers by laser excitation at exciton resonances. *Phys. Rev. Lett.* **114 (9)**, 097403 (2015).

[19] T. Cheiwchanchamnangij, W. R. L. Lambrecht. Quasiparticle band structure calculation of monolayer, bilayer, and bulk MoS_2. *Phys. Rev. B* **85 (20)**, 205302 (2012).

[20] A. Ramasubramaniam. Large excitonic effects in monolayers of molybdenum and tungsten dichalcogenides. *Phys. Rev. B* **86 (11)**, 115409 (2012).

[21] H. P. Komsa, A. V. Krasheninnikov. Effects of confinement and environment on the electronic structure and exciton binding energy of MoS_2 from first principles. *Phys. Rev. B* **86 (24)**, 241201(R) (2012).

[22] R. C. Miller, D. A. Kleinman, W. T. Tsang, A. C. Gossard. Observation of the excited level of excitons in GaAs quantum wells. *Phys. Rev. B* **24 (2)**, 1134(R) (1981).

[23] R. L. Greene, K. K. Bajaj, D. E. Phelps. Energy levels of Wannier excitons in GaAs-$Ga_{1-x}Al_xAs$ quantum-well structures. *Phys. Rev. B* **29 (4)**, 1807 (1984).

[24] N. T. Pelekanos, J. Ding, M. Hagerott, A. V. Nurmikko, H. Luo, N. Samarth, J. K. Furdyna. Quasi-two-dimensional excitons in (Zn,Cd)Se/ZnSe quantum wells: reduced exciton–LO-phonon coupling due to confinement effects. *Phys. Rev. B* **45 (11)**, 6037 (1992).

[25] M. Z. Maialle, E. A. de Andrada e Silva, L. J. Sham. Exciton spin dynamics in quantum wells. *Phys. Rev. B* **47 (23)**, 15776 (1993).

[26] A. Vinattieri, J. Shah, T. C. Damen, D. S. Kim, L. N. Pfeiffer, M. Z. Maialle, L. J. Sham. Exciton dynamics in GaAs quantum wells under resonant excitation. *Phys. Rev. B* **50 (15)**, 10868 (1994).

[27] C. Bradford, C. B. O'Donnell, B. Urbaszek, C. Morhain, A. Balocchi, K. A. Prior, B. C. Cavenett. Highly confined excitons in MgS/ZnSe quantum wells grown by molecular beam epitaxy. *Phys. Rev. B* **64 (19)**, 195309 (2001).

[28] S. M. Sze. *Semiconductor devices: physics and technology* (John Wiley & Sons, Inc., New York, USA, 2002), 2nd edn. ISBN: 9780471333722.

[29] H. Haug, S. W. Koch. *Quantum theory of the optical and electronic properties of semiconductors* (World Scientific Publishing Co. Pte. Ltd, Singapore, 2009), 5th edn. ISBN: 9789812838834.

[30] S. Z. Butler, S. M. Hollen, L. Cao, Y. Cui, J. A. Gupta, H. R. Gutiérrez, T. F. Heinz, S. S. Hong, J. Huang, A. F. Ismach, E. Johnston-Halperin, M. Kuno, V. V. Plashnitsa, R. D. Robinson, R. S. Ruoff, S. Salahuddin, J. Shan, L. Shi, M. G. Spencer, M. Terrones, W. Windl, J. E. Goldberger. Progress, challenges, and opportunities in two-dimensional materials beyond graphene. *ACS Nano* **7 (4)**, 2898–2926 (2013).

[31] K. F. Mak, C. Lee, J. Hone, J. Shan, T. F. Heinz. Atomically thin MoS_2: a new direct-gap semiconductor. *Phys. Rev. Lett.* **105 (13)**, 136805 (2010).

[32] S. Schmitt-Rink, C. Ell. Excitons and electron-hole plasma in quasi-two-dimensional systems. *J. Lumin.* **30 (1-4)**, 585–596 (1985).

[33] R. Sooryakumar, D. S. Chemla, A. Pinczuk, A. C. Gossard, W. Wiegmann, L. J. Sham. Valence band mixing in GaAs-(AlGa)As heterostructures. *Solid State Commun.* **54 (10)**, 859–862 (1985).

[34] S. Schmitt-Rink, C. Ell, H. Haug. Many-body effects in the absorption, gain, and luminescence spectra of semiconductor quantum-well structures. *Phys. Rev. B* **33 (2)**, 1183 (1986).

[35] H. Haug, S. Schmitt-Rink. Electron theory of the optical properties of laser-excited semiconductors. *Prog. Quant. Electr.* **9 (1)**, 3–100 (1984).

[36] A. Ayari, E. Cobas, O. Ogundadegbe, M. S. Fuhrer. Realization and electrical characterization of ultrathin crystals of layered transition-metal dichalcogenides. *J. Appl. Phys.* **101 (1)**, 014507 (2007).

[37] B. Radisavljevic, A. Radenovic, J. Brivio, V. Giacometti, A. Kis. Single-layer MoS_2 transistors. *Nat. Nanotechnol.* **6**, 147–150 (2011).

[38] M. Van der Donck, M. Zarenia, F. M. Peeters. Excitons and trions in monolayer transition metal dichalcogenides: a comparative study between the multiband model and the quadratic single-band model. *Phys. Rev. B* **96 (3)**, 035131 (2017).

[39] C. Mai, A. Barrette, Y. Yu, Y. G. Semenov, K. W. Kim, L. Cao, K. Gundogdu. Many-body effects in valleytronics: direct measurement of valley lifetimes in single-layer MoS_2. *Nano Lett.* **14 (1)**, 202–206 (2014).

[40] Y. You, X.-X. Zhang, T. C. Berkelbach, M. S. Hybertsen, D. R. Reichman, T. F. Heinz. Observation of biexcitons in monolayer WSe_2. *Nat. Phys.* **11**, 477–481 (2015).

[41] G.-B. Liu, W.-Y. Shan, Y. Yao, W. Yao, D. Xiao. Three-band tight-binding model for monolayers of group-VIB transition metal dichalcogenides. *Phys. Rev. B* **88 (8)**, 085433 (2013).

[42] M. M. Glazov, T. Amand, X. Marie, D. Lagarde, L. Bouet, B. Urbaszek. Exciton fine structure and spin decoherence in monolayers of transition metal dichalcogenides. *Phys. Rev. B* **89 (20)**, 201302(R) (2014).

[43] A. Kormányos, G. Burkard, M. Gmitra, J. Fabian, V. Zólyomi, N. D. Drummond, V. Fal'ko. **k·p** theory for two-dimensional transition metal dichalcogenide semiconductors. *2D Mater.* **2 (2)**, 022001 (2015).

[44] H. Dery, Y. Song. Polarization analysis of excitons in monolayer and bilayer transition-metal dichalcogenides. *Phys. Rev. B* **92 (12)**, 125431 (2015).

[45] A. Arora, M. Koperski, K. Nogajewski, J. Marcus, C. Faugeras, M. Potemski. Excitonic resonances in thin films of WSe_2: from monolayer to bulk material. *Nanoscale* **7 (23)**, 10421–10429 (2015).

[46] A. Arora, K. Nogajewski, M. Molas, M. Koperski, M. Potemski. Exciton band structure in layered $MoSe_2$: from a monolayer to the bulk limit. *Nanoscale* **7 (48)**, 20769–20775 (2015).

[47] L. Schultheis, J. Kuhl, A. Honold, C. W. Tu. Ultrafast phase relaxation of excitons via exciton-exciton and exciton-electron collisions. *Phys. Rev. Lett.* **57 (13)**, 1635 (1986).

[48] A. Honold, L. Schultheis, J. Kuhl, C. W. Tu. Collision broadening of two-dimensional excitons in a GaAs single quantum well. *Phys. Rev. B* **40 (9)**, 6442(R) (1989).

[49] P. Hawrylak. Optical properties of a two-dimensional electron gas: evolution of spectra from excitons to Fermi-edge singularities. *Phys. Rev. B* **44 (8)**, 3821 (1991).

[50] T. Ogawa. Quantum states and optical responses of low-dimensional electron–hole systems. *J. Phys. Condens. Matter* **16 (35)**, S3567 (2004).

[51] C. Zhang, H. Wang, W. Chan, C. Manolatou, F. Rana. Absorption of light by excitons and trions in monolayers of metal dichalcogenide MoS_2: experiments and theory. *Phys. Rev. B* **89 (20)**, 205436 (2014).

[52] B. Scharf, Z. Wang, D. V. Tuan, J. Shan, K. F. Mak, I. Zutic, H. Dery. Probing many-body interactions in monolayer transition-metal dichalcogenides. *Preprint at https://arxiv.org/abs/1606.07101* (2016).

[53] A. Singh, G. Moody, K. Tran, M. E. Scott, V. Overbeck, G. Berghäuser, J. Schaibley, E. J. Seifert, D. Pleskot, N. M. Gabor, J. Yan, D. G. Mandrus, M. Richter, E. Malic, X. Xu, X. Li. Trion formation dynamics in monolayer transition metal dichalcogenides. *Phys. Rev. B* **93 (4)**, 041401(R) (2016).

[54] T. Takagahara. Localization and homogeneous dephasing relaxation of quasi-two-dimensional excitons in quantum-well heterostructures. *Phys. Rev. B* **32 (10)**, 7013(R) (1985).

[55] J. Hegarty, M. D. Sturge. Studies of exciton localization in quantum-well structures by nonlinear-optical techniques. *J. Opt. Soc. Am. B* **2 (7)**, 1143–1154 (1985).

[56] A. J. Fischer, D. S. Kim, J. Hays, W. Shan, J. J. Song, D. B. Eason, J. Ren, J. F. Schetzina, H. Luo, J. K. Furdyna. Femtosecond four-wave-mixing studies of exciton localization and exciton-exciton interaction in ZnSe/$Zn_xCd_{1-x}Se$ quantum wells. *Phys. Rev. B* **50 (23)**, 17643 (1994).

[57] A. Srivastava, M. Sidler, A. V. Allain, D. S. Lembke, A. Kis, A. Imamoğlu. Optically active quantum dots in monolayer WSe_2. *Nat. Nanotechnol.* **10**, 491–496 (2015).

[58] Y.-M. He, G. Clark, J. R. Schaibley, Y. He, M.-C. Chen, Y.-J. Wei, X. Ding, Q. Zhang, W. Yao, X. Xu, C.-Y. Lu, J.-W. Pan. Single quantum emitters in monolayer semiconductors. *Nat. Nanotechnol.* **10**, 497–502 (2015).

[59] M. Koperski, K. Nogajewski, A. Arora, V. Cherkez, P. Mallet, J. Y. Veuillen, J. Marcus, P. Kossacki, M. Potemski. Single photon emitters in exfoliated WSe_2 structures. *Nat. Nanotechnol.* **10**, 503–506 (2015).

[60] G. Moody, C. K. Dass, K. Hao, C.-H. Chen, L.-J. Li, A. Singh, K. Tran, G. Clark, X. Xu, G. Berghäuser, E. Malic, A. Knorr, X. Li. Intrinsic homogeneous linewidth and broadening mechanisms of excitons in monolayer transition metal dichalcogenides. *Nat. Commun.* **6**, 8315 (2015).

[61] N. F. Mott, E. A. Davis. *Electronic processes in non-crystalline materials* (Oxford University Press, Oxford, UK, 1979), 2nd edn. ISBN: 9780199645336.

[62] M. Palummo, M. Bernardi, J. C. Grossman. Exciton radiative lifetimes in two-dimensional transition metal dichalcogenides. *Nano Lett.* **15 (5)**, 2794–2800 (2015).

[63] H. Wang, C. Zhang, W. Chan, C. Manolatou, S. Tiwari, F. Rana. Radiative lifetimes of excitons and trions in monolayers of the metal dichalcogenide MoS_2. *Phys. Rev. B* **93 (4)**, 045407 (2016).

[64] J. Lee, E. S. Koteles, M. O. Vassell. Luminescence linewidths of excitons in GaAs quantum wells below 150 K. *Phys. Rev. B* **33 (8)**, 5512 (1986).

[65] S. Rudin, T. L. Reinecke, B. Segall. Temperature-dependent exciton linewidths in semiconductors. *Phys. Rev. B* **42 (17)**, 11218 (1990).

[66] T. Jakubczyk, V. Delmonte, M. Koperski, K. Nogajewski, C. Faugeras, W. Langbein, M. Potemski, J. Kasprzak. Radiatively limited dephasing and exciton dynamics in $MoSe_2$ monolayers revealed with four-wave mixing microscopy. *Nano Lett.* **16 (9)**, 5333–5339 (2016).

[67] M. Selig, G. Berghäuser, A. Raja, P. Nagler, C. Schüller, T. F. Heinz, T. Korn, A. Chernikov, E. Malic, A. Knorr. Excitonic linewidth and coherence lifetime in monolayer transition metal dichalcogenides. *Nat. Commun.* **7**, 13279 (2016).

[68] K. Kheng, R. T. Cox, Y. Merle d'Aubigné, F. Bassani, K. Saminadayar, S. Tatarenko. Observation of negatively charged excitons X^- in semiconductor quantum wells. *Phys. Rev. Lett.* **71 (11)**, 1752 (1993).

[69] V. Huard, R. T. Cox, K. Saminadayar, A. Arnoult, S. Tatarenko. Bound states in optical absorption of semiconductor quantum wells containing a two-dimensional electron gas. *Phys. Rev. Lett.* **84 (1)**, 187 (2000).

[70] G. Finkelstein, H. Shtrikman, I. Bar-Joseph. Optical spectroscopy of a two-dimensional electron gas near the metal-insulator transition. *Phys. Rev. Lett.* **74 (6)**, 976 (1995).

[71] Y. P. Varshni. Temperature dependence of the energy gap in semiconductors. *Physica* **34 (1)**, 149–154 (1967).

[72] K. P. O'Donnell, X. Chen. Temperature dependence of semiconductor band gaps. *Appl. Phys. Lett.* **58 (25)**, 2924 (1991).

[73] J. Feldmann, G. Peter, E. O. Göbel, P. Dawson, K. Moore, C. Foxon, R. J. Elliott. Linewidth dependence of radiative exciton lifetimes in quantum wells. *Phys. Rev. Lett.* **59 (20)**, 2337 (1987).

[74] L. C. Andreani, F. Tassone, F. Bassani. Radiative lifetime of free excitons in quantum wells. *Solid State Commun.* **77 (9)**, 641–645 (1991).

[75] S. Tongay, J. Zhou, C. Ataca, K. Lo, T. S. Matthews, J. Li, J. C. Grossman, J. Wu. Thermally driven crossover from indirect toward direct bandgap in 2D semiconductors: $MoSe_2$ versus MoS_2. *Nano Lett.* **12 (11)**, 5576–5580 (2012).

[76] P. Tonndorf, R. Schmidt, P. Böttger, X. Zhang, J. Börner, A. Liebig, M. Albrecht, C. Kloc, O. Gordan, D. R. T. Zahn, S. Michaelis de Vasconcellos, R. Bratschitsch. Photoluminescence emission and Raman response of monolayer MoS_2, $MoSe_2$, and WSe_2. *Opt. Express* **21 (4)**, 4908–4916 (2013).

[77] R. Geick, C. H. Perry, G. Rupprecht. Normal modes in hexagonal boron nitride. *Phys. Rev.* **146 (2)**, 543 (1966).

Chapter 5

Photoluminescence of interlayer excitons in transition metal dichalcogenide heterostructures

5.1 Introduction

Semiconductor van der Waals heterostructures (HSs) consisting of two-dimensional (2D) materials open new possibilities for optoelectronic devices and exhibit intriguing phenomena [1]. Presenting unique properties defined by tightly bound excitons [2, 3] and optical selection rules with valley-contrasting physics [4, 5], the atom-thin transition-metal dichalcogenides (TMDCs) are good candidates for creating van der Waals heterobilayers in order to understand their physics.

The monolayer TMDC/monolayer TMDC HSs mostly form a staggered (type-II) heterojunction (Fig. 5.3a) in which the conduction band minimum (CBM) and the valence band maximum (VBM) are positioned in different layers [6–10]. The band offsets are completely dependent on the HS constituents. Since all components of such functional materials have small thicknesses, the impact of layer charging on the band structure is still unknown and not depicted in the diagrams of the mentioned heterojunctions. The first-principles calculations [9, 11] establish that the hybrid bilayers with common chalcogen atoms have an indirect band gap while the metal-common bilayers have a direct band gap (the MoS_2/WSe_2 is also direct-bandgap). However, this topic requires more study, because some other computing and experimental results reveal that the MoS_2/WS_2 and $MoSe_2/WSe_2$ heterobilayers show direct-bandgap structures [12–14]. It is expected that the interlayer interaction, specifically interlayer distance, significantly influences the conduction and valence band edges of many of the TMDC-based HSs and turn into direct-gap semiconductors from indirect-gap semiconductors when the interlayer space rises [15–17].

Due to the aforementioned band alignment of the 2D TMDC-based hybrid materials, photoexcited electrons and holes prefer to stay at the CBM and VBM positioned in different layers and form interlayer (or spatially indirect) excitons (IXs) as seen in Fig. 5.3a. This process can be divided by several steps. First, intralayer (or spatially direct) excitons (DXs) are generated within the TMDC monolayers. Then, charge carriers of intralayer excitons are rapidly transferred ($\sim$ 50 fs in the MoS_2/WS_2) through the heterojunction [10, 18–21]. In such a way, an ultrafast formation of the intermediate exciton states with the excess energy (known as interlayer hot excitons [21]) occurs [22]. Finally, the relaxation of hot excitons (about 0.8 ps in the MoS_2/WS_2 [22]) and their localization around charged defects at the van der Waals interface of the HSs cause a creation of strongly donor-bound IX complexes [23].

The orientation of the TMDC layers relative to each other during the vertical stacking process is crucial. Heo *et al.* [12] demonstrated from the band structure calculation of the MoS_2/WS_2 bilayer that relative crystal lattice rotation of the stacked flakes is reflected in the alignment of the Brillouin zones of each monolayer. When the stacking is coherent, namely hexagonal momentum unit cell of one layer coincides with hexagonal unit cell of other layer without incommensurate twist angles, the band gap is direct and occurs at the K point. Random stacking provides a shift and transformation of the band edges of each monolayer included in the HS. Therefore, the indirect band gap characterizes the heterobilayer in this case. It is theoretically and experimentally confirmed that the strong IX photoluminescence can be observed only in the aligned TMDC-based HSs, that is, at twist angles of 0 °

and 60 ° [20, 24]. We also highlight the importance of the crystal lattice alignment in subsection 5.3.1.

Among the experimental studies of the interlayer coupling in the TMDC-based hybrid bilayers, measurements using photoluminescence (PL) spectroscopy play a significant role. Quenching of the DX emission within the HS [10, 18–22] indicates the IX formation after the interlayer ultrafast charge transfer. The IX signal is clearly detected in PL spectra [12, 16, 18, 20, 25]. The presence of the IX emission is also proved by a large (≥ 100 meV) Stokes-like shift between the PL and absorbance DX peaks [12, 18]. From the polarization-resolved PL experiments [26], it is established that the circularly polarized PL which retains the helicity of the incident laser is emitted by indirect excitons. Such behaviour is possible since the spin-valley polarization is conserved during the charge transfer across the staggered TMDC-based heterojunction [27]. But in the epitaxially grown commensurate HSs, the helicity of the circularly polarized IX emission is changed to opposite to the initial optical excitation because of the quantum interference determined by well-defined stacking [28]. Eventually, the time-resolved PL measurements unveil the IX recombination dynamics. Unlike picosecond-lived intralayer excitons [29, 30], interlayer excitons possess $\sim$ 10–100 ns lifetime [31, 32] whereas their valley polarization lifetime is as high as tens of nanosecond [26]. The recent study [33] revealed microsecond interlayer dark exciton timescale.

In this work, we consider two types of HSs: $MoSe_2/WSe_2$ and $MoSe_2/WS_2$. Interestingly, the $MoSe_2$ and WS_2 monolayers have a specific band alignment between each other. According to the first-principles [6] and density functional theory [7] calculations, the conduction band offset in the $MoSe_2/WS_2$ heterobilayer is small and equal to 20–60 meV. Consequently, if the hybridization of electronic states in the constituent layers is negligible and the type-II heterojunction exists, the spectral position of IX optical transition has to be slightly redshifted with regard to the DX PL signal of the single-layer $MoSe_2$ (Fig. 5.11a). Only few research groups [34–36] observed and investigated the shifted emission in the aforesaid HSs and nevertheless, the origin of this signal is still complicated without clear evidence for its interlayer or intralayer nature. It is confirmed the existence of the WS_2 trion peak [34] formed due to the charge transfer [35] from the $MoSe_2$ and the Förster-type (dipole-dipole) interlayer energy transfer [36].

Having the above favourable properties, long-lived indirect excitons of the TMDC-based layered materials may provide an interesting system for a realisation for high-temperature bosonic degenerate exciton gases which are necessary to study fundamental physics phenomena including superfluidity [37] and Bose–Einstein condensation [38]. Also, the IX extended lifetimes can help to transport excitons to longer distances essential for excitonic devices [39, 40]. Usage of the TMDC-based van der Waals heterointerfaces as ultrathin photovoltaic devices [18, 41–43] may open new possibilities in optoelectronics.

In spite of a big variety of the discovered IX properties, many questions are not clearly answered in this research area yet. For instance, a spectral peak structure of the IX PL signal and influence of the protecting encapsulation. We investigate these topics in our experiments described below. In addition, we attempt to clarify the nature of the PL in the $MoSe_2/WS_2$ HS. The measured emission parameters are presented as functions of laser excitation power, temperature and gate voltage.

5.2 Samples and experimental methods

We measure the emission and its polarization properties in the 2D $MoSe_2/WSe_2$ and $MoSe_2/WS_2$ HSs using PL and photoluminescence excitation (PLE) spectroscopies. The basic concepts on these study techniques are viewed in section 2.2.

Most of the heterobilayers are produced on either the 90 nm or 290 nm SiO_2/ Si substrates by mechanical transfer/stacking based on the combined polymethyl methacrylate (PMMA) dry- and wet-transfer method. Additionally, only the PMMA dry-peel transfer is used for the production of some HSs. For example, the type-A polarization measurements (subsection 5.3.1) are performed with the $MoSe_2/WSe_2$ structures made by this technique. The detailed description of all sample fabrication methods is presented in subsection 2.1.3. In the majority of studied HSs, the mono-

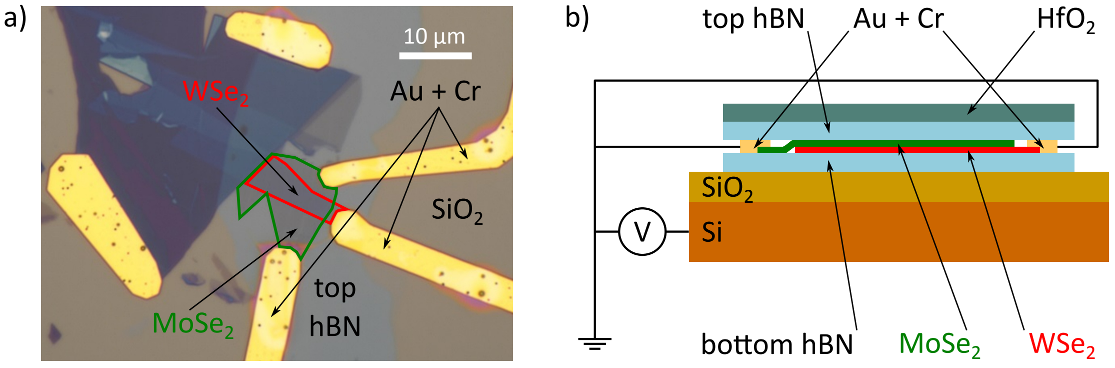

Fig. 5.1 The HfO$_2$/hBN encapsulated gated MoSe$_2$/WSe$_2$ HS and its structure. All materials are labelled with their chemical names. The 20 nm HfO$_2$ completely covers the samples and therefore, is not marked on the microscope image. The hBN consists of the top and bottom films which are on top and underneath the heterobilayer, respectively. (a) The optical microscope image of one of the samples without the bottom hBN layer. The monolayer MoSe$_2$ (WSe$_2$) flake is bordered with green (red) lines. (b) The sample's diagram. Only one electric contact to each TMDC sheet of the HS is shown for simplicity.

layer MoSe$_2$ is placed on top of either WSe$_2$ or WS$_2$.

Since the SiO$_2$ surface is rather rough and at best only small TMDC monolayers (about few micron in width) can be exfoliated on it, the hexagonal boron nitride (hBN) crystals of several tens of nm thickness are first cleaved onto the substrate using the water soluble tape (Nitto tape). A flatter surface of the hBN without terraces or contamination provides stronger adhesion of the TMDC atomic layers and thus, much larger flakes with dimensions up to a few tens of μm could be produced. Hence, our HSs are often placed onto the hBN crystals.

In our experiments, we investigate the impact of the HfO$_2$/hBN encapsulation of the MoSe$_2$/WSe$_2$ heterobilayers on the indirect exciton properties (subsections 5.3.1 and 5.4.1). For this aim, an appropriate exfoliated hBN layer with thickness of a few tens of nm is wet transferred onto a HS and then, 20 nm of an electron-beam evaporated HfO$_2$ caps all flakes and whole substrate surface. One of the samples fabricated in this way as well as the schematic drawing of the general structure of our encapsulated gated samples are depicted in Fig. 5.1. We establish that such HfO$_2$/hBN capping significantly improves the sample stability: the PL taken from the capped flakes and HSs shows minimal changes in its intensity and spectral shape after several thermal cycles.

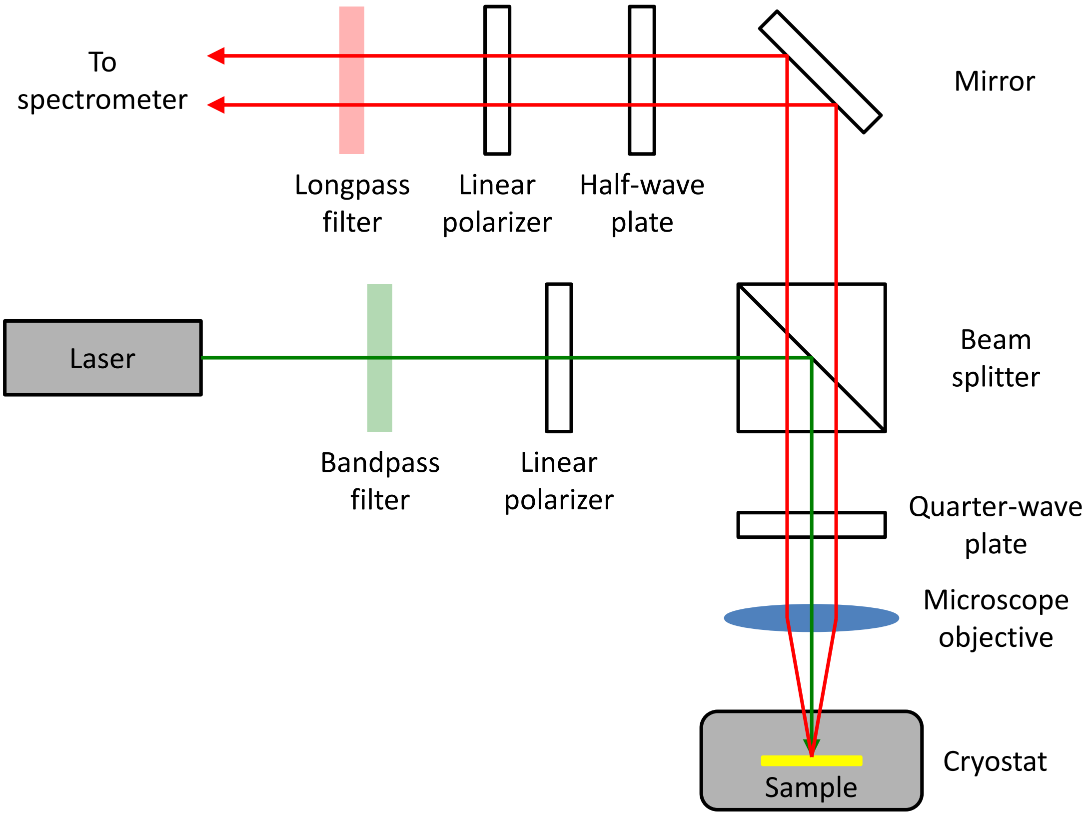

Fig. 5.2 The sketch of the μPL set-up used in the polarization measurements. Green and red broken arrows indicate the pathways of the laser beam up to the sample and the emission going to the spectrometer, respectively.

Before the mentioned encapsulation (or encapsulation only with the hBN flake as in the case of the $MoSe_2/WS_2$ HS), Cr/Au electrodes are patterned on some samples using standard electron-beam lithography described in subsection 2.1.4 (Fig. 5.1). For better and more reliable connection, each individual TMDC atomic sheet is bonded to a cryostat sample holder which is in turn connected to a voltage source (Keithley 2400 or 2450). So, the gate voltage V_g can be applied through the fabricated contacts in these gated samples. As discussed in [44] and subsection 4.4.3, the density of free carriers injected into the layered structure inversely depends on the thicknesses of dielectric layers between the capacitor electrodes (TMDC monolayers and doped Si in our case). Consequently, the thinner SiO_2 in the substrates, the lower the working V_g range safely used in practice. In this study, V_g is extended from -90 V to +90 V for the samples containing the 290 nm SiO_2/Si and from -20 V to +20 V for those with the 90 nm silicon dioxide substrate surfaces.

Optical characterization of the $MoSe_2/WSe_2$ and $MoSe_2/WS_2$ HSs is carried out using the low-temperature micro-photoluminescence (μPL) set-up. More information on this set-up and corresponding technique is presented in subsubsection 2.2.1.3.

For the polarization-resolved experiments, additional optical elements are inserted into the set-up (Fig. 5.2). A first polarizer near the laser diode creates the linear polarization of the laser light. A quarter-wave ($\lambda/4$) plate before the microscope objective and sample either converts the laser beam polarization into circular or keeps its linearity by means of an automatic rotary mount system (Standa 8MR151-1). The emitted signal coming through the $\lambda/4$ plate consists of linearly polarized components. The combination of a half-wave ($\lambda/2$) plate and second linear polarizer in the collection path provides the detection of the polarized emission which can be co- or cross-oriented relative to the incident laser light (behind the $\lambda/4$ plate and before falling to the sample). As in the case of the quarter-wave plate, the above detection control is performed via the automatic rotary mount system (Standa 8MR151-1) connected to the $\lambda/2$ plate.

5.3 Results

5.3.1 Interlayer excitons: formation and photoluminescence

As discussed in section 5.1, interlayer excitons arise at the staggered (type-II) 2D TMDC-based heterojunction (Fig. 5.3a) and give us an opportunity to create the tunable direct band gaps [6, 9]. The low-temperature PL spectra in Fig. 5.3b represent these band offsets in the $MoSe_2/WSe_2$ and $MoSe_2/WS_2$ HSs. While the DX spectral peaks and bands, namely A, A^* and localized states (LSs), are visible and located in a range of $\sim$ 1.49–1.75 eV, the main IX features have the energy range of about 1.3–1.4 eV in the $MoSe_2/WSe_2$ HS. The energy difference between the charged IX^* and WSe_2 A^* exciton peaks equals 326 meV (310 meV in [20]) and corresponds to a lower bound on the conduction band offset. Similarly, a lower bound on the

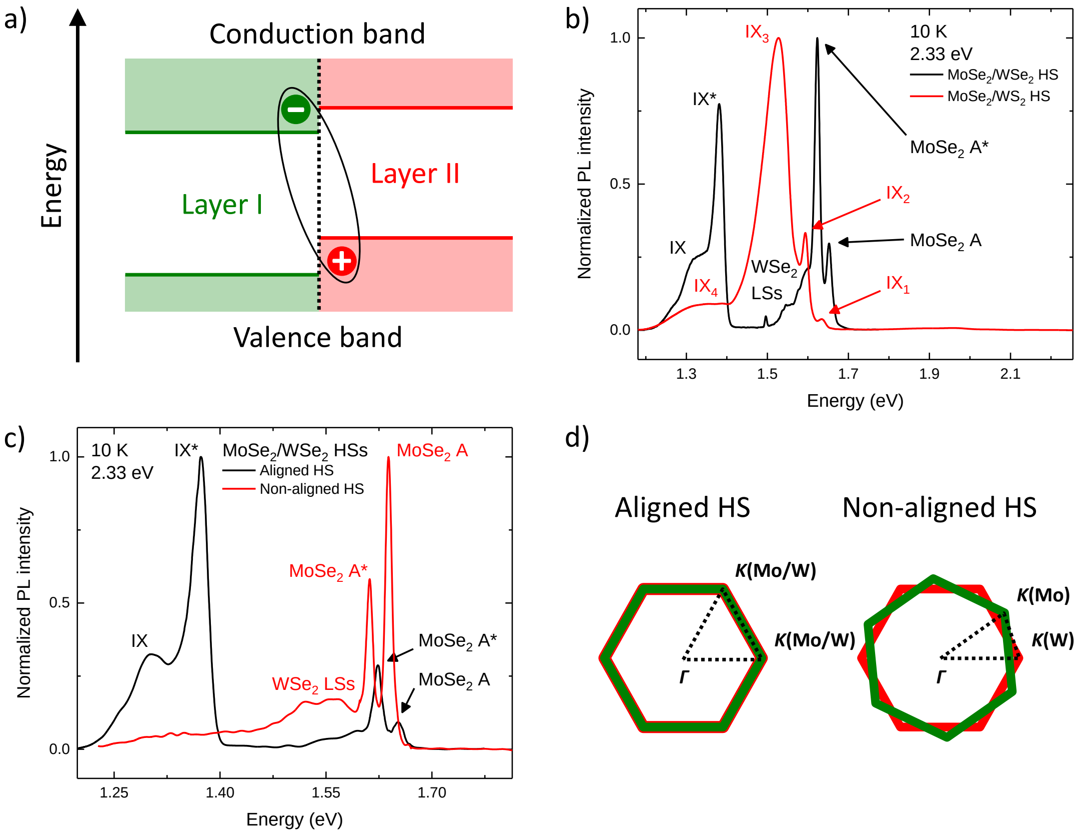

Fig. 5.3 Interlayer excitons and their PL spectra. (a) The schematic representation of type-II semiconductor band alignment for the 2D TMDC-based heterojunction where interlayer excitons are formed. The heterostructure consists of two monolayers marked as *Layer I* and *Layer II*. Energy axis is vertically positioned. (b) The normalized PL spectra which are taken from the MoSe$_2$/WSe$_2$ (black) and MoSe$_2$/WS$_2$ (red) HSs and demonstrate the influence of the band offsets. The applied laser excitation: 2.33 eV, 20 μW. Temperature: 10 K. (c) The impact of the crystal lattice alignment on the observation of IX spectral peaks. Both normalized PL spectra of the aligned (black) and non-aligned (red) MoSe$_2$/WSe$_2$ HSs are obtained under 1 μW laser excitation at 2.33 eV and temperature of 10 K. All visible inter- and intralayer excitonic peaks and bands are labelled in (b), (c). (d) The diagram showing the aligned (left) and non-aligned (right) 2D hexagonal lattices of the single-layer MoSe$_2$ (green) and WSe$_2$ (red) in momentum space. K and Γ points of the Brillouin zone are indicated.

valence band offset is equal to 240 meV and set as the energy difference between IX^* and MoSe$_2$ A^* (it is 230 meV from earlier results [20]). Subsection 5.3.2 contains more information about localized IX complexes in such structures. The MoSe$_2$/WS$_2$ HS area does not present any prominent DX spectral peaks (Fig. 5.3b). Its PL is strongly redshifted from the intralayer excitonic signal of the individual monolayers but partly still shows the optical properties of the MoSe$_2$ excitonic peaks. We suggest that this signal of the HS region can be derived from excitons with the hybridized electronic states in the MoSe$_2$ and WS$_2$ single layers which contain energetically almost the same levels of the conduction band minima [6, 10]. A detailed description of the PL spectral peaks of the MoSe$_2$/WS$_2$ HS will be given in subsection 5.3.3.

The crystal lattice alignment plays an important role in the IX formation [12], which is illustrated in Fig. 5.3c–d using the low-temperature PL spectra of the the MoSe$_2$/WSe$_2$ HSs. When the TMDC monolayers are randomly stacked during the sample fabrication, no IX PL signal is detected from the HS. On the other hand, the coherently stacked heterobilayers demonstrate strong IX spectral peaks which are even stronger in intensity than DX peaks at low laser excitation powers (1–12 μW). The dependence on the twist angle confirms that the IX emission is not defect-related. Our work has only focused on the investigations of the aligned HSs.

5.3.2 Interlayer excitons in MoSe$_2$/WSe$_2$ heterostructures

One of the most typical TMDC-based heterobilayers produced for the study of the optoelectronic properties of the interlayer exciton complexes is MoSe$_2$/WSe$_2$. This subsection represents our experimental results concerned with such HSs. The information about the experimental techniques, set-up and sample production is viewed in detail in section 5.2 and chapter 2.

5.3.2.1 Polarization-resolved photoluminescence

Here, we describe the polarization-resolved PL measurements in the MoSe$_2$/WSe$_2$ HSs.

Before the description of the polarization measurements, it is worth mentioning

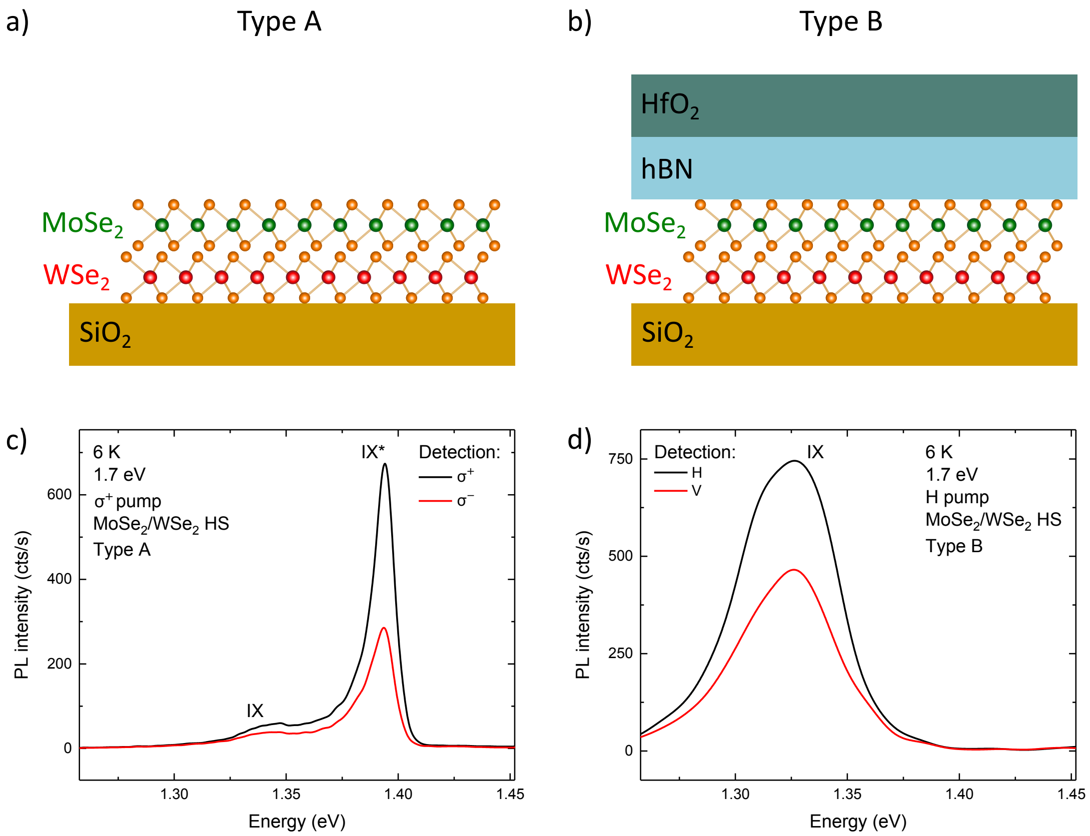

Fig. 5.4 The influence of the HfO_2/hBN encapsulation on the spectral shape of the IX PL signal and its polarization in the $MoSe_2$/WSe_2 HSs. The schematic drawings of the (a) non-encapsulated (type-A) and (b) encapsulated (type-B) samples. All stacked layers are named. The polarization-resolved IX PL spectra under the (c) right circularly (σ^+) and (d) linearly (H) polarized laser excitations for the type-A and type-B HSs, respectively. Data with the same (‘opposite’) emission detection are coloured in black (red). The ‘opposite’ emission means the σ^- left circularly and V linearly (perpendicularly to H) polarized signal. IX (IX^*) denotes the spectral peak of localized neutral (charged) interlayer complexes. Parameters of the applied laser excitation: 1.7 eV, 20 μW. Temperature: 6 K.

about the spectral shape of the IX PL signal. All performed experiments demonstrate that the emission of non-encapsulated samples mostly consist of two peaks (Fig. 5.4a,c). According to [23], they are identified as peaks of interlayer excitons (IX) and trions (IX^*), both of which are bound to donor impurities in the $MoSe_2$ layer. Their peak maxima are positioned at $\sim$ 1.32–1.34 eV and 1.38–1.40 eV, respectively (in contrast to the intralayer excitonic states, these trion complexes have higher transition energy relative to that for the indirect excitons owing to the localization effects). The HfO_2/hBN encapsulation of the HS during the sample fabrication

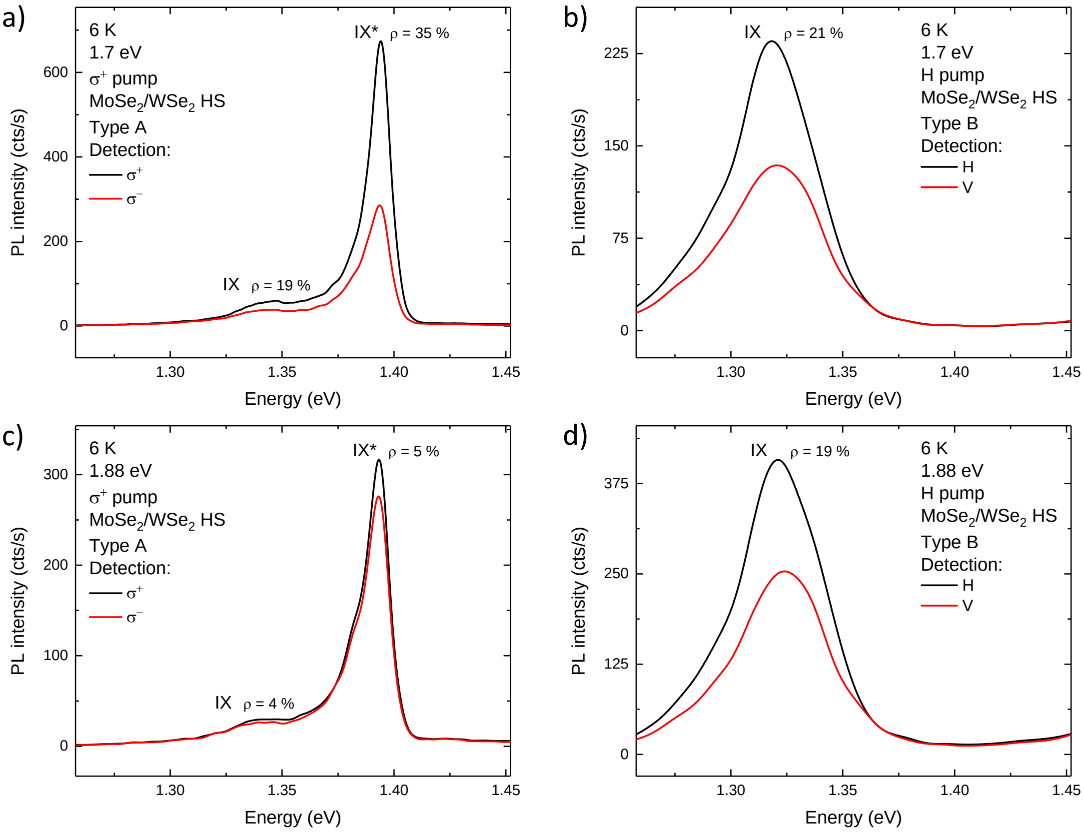

Fig. 5.5 The role of the laser excitation energy in the polarization of the IX emission of the $MoSe_2/WSe_2$ HSs. The polarization-resolved IX PL spectra under the (a), (c) right circularly (σ^+) and (b), (d) linearly (H) polarized laser excitations for the type-A and type-B HSs, respectively. Black-coloured (red-coloured) data correspond to the same ('opposite') emission detection. The 'opposite' emission means the σ^- left circularly and V linearly (perpendicularly to H) polarized signal. ρ indicates the degree of polarization (in percent). The neutral (IX) and charged (IX^*) interlayer exciton spectral peaks are denoted. The applied laser excitations are set at power of 20 μW and energies of (a)–(b) 1.7 eV and (c)–(d) 1.88 eV. Temperature: 6 K. All PL data are gathered from one measurement point on the type-A and type-B samples.

process results in the observation of only one IX spectral peak (Fig. 5.4b,d). This peak is much broader than that from the non-encapsulated HS but without any significant position energy shifts. We call samples without the HfO_2/hBN capping as type A and with the capping as type B for clarity.

The above-mentioned encapsulation of the $MoSe_2/WSe_2$ HS makes changes not only in the spectral shape of the IX PL signal but in its polarization properties. The type-A IX emission presents strong circular (several tens of %, Fig. 5.4c) and small linear (up to 7 %) polarization. Simultaneously, the HfO_2/hBN capped HS

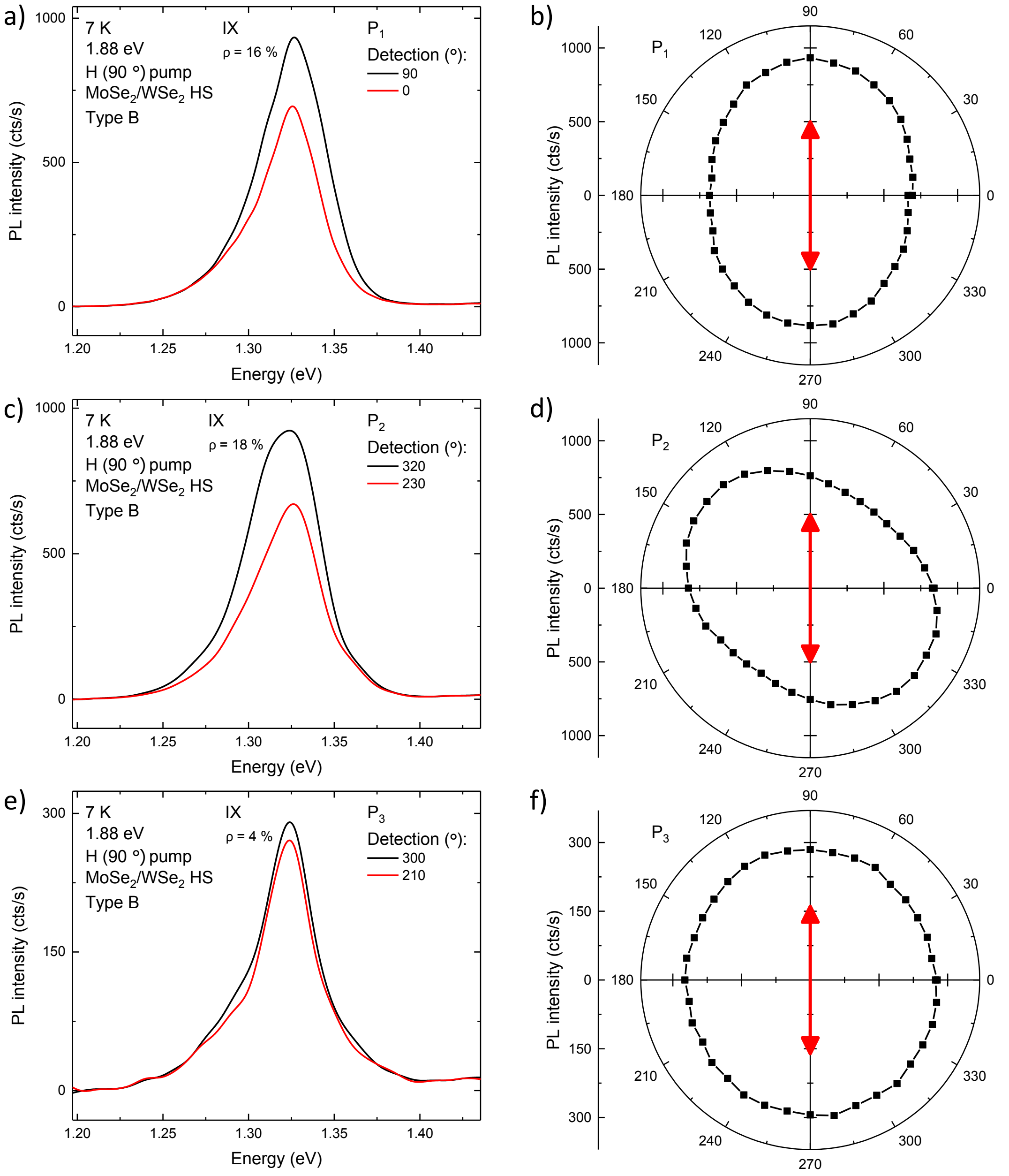

Fig. 5.6 The linear polarization of the IX emission in the type-B $MoSe_2/WSe_2$ HS. The applied laser excitation: 1.88 eV, 20 μW. Temperature: 7 K. Data are taken from three points (P_1, P_2 and P_3) on the HS. (b), (d), (f) The IX peak intensity as a function of detection angle (in degrees) for the given incident laser polarization (H (90 °)) marked by red arrow in polar coordinate system. (a), (c), (e) The PL spectra with the maximal (black) and minimal (red) IX peak intensities. Their detection angles are specified in the legends of the plots. The degree of polarization (in percent) are denoted by ρ.

is characterized with the linearly polarized IX PL (up to 25 %, Fig. 5.4d). Some measurement points contain a IX peak position shift between the signals which are linearly co- and cross-polarized relative to the incident laser polarization. The type-B IX PL degree of circular polarization fluctuates from -8 % to 2 % which is negligibly small. The reasons for such effects will be considered in subsection 5.4.1. Also for the type-A samples, the IX PL circular polarization degree dramatically increases when the laser excitation has an energy which is close to the DX peak positions (Fig. 5.5a,c). Interestingly, the type-B linearly polarized signal almost does not show the above tendency (Fig. 5.5b,d). All our suggestions about this will be described in detail in subsection 5.4.1.

In order to better investigate the origin of the linear polarization of the IX PL signal in the encapsulated HS, the experimental results shown in Fig. 5.6 are performed with the set-up without the quarter-wave plate to remove a systematic error caused by this plate. A PL spectrum is collected by turning the half-wave plate with steps of 10 °. As a consequence, we are able to detect the polarization axis in different spots across the HS under the fixed incident laser linear polarization. It is established that the IX peak emission of the type-B samples demonstrate a variety of directions of the polarization axis (as examples in Fig. 5.6a–d) and even an absence of any significant linear polarization (Fig. 5.6e–f). The analysis of this effect is included in the discussion of the polarization measurements of the $MoSe_2/WSe_2$ HSs in subsection 5.4.1.

5.3.2.2 Power dependence of photoluminescence

Both the type-A IX and DX PL collected from the same measurement point on the $MoSe_2/WSe_2$ HS is studied as a function of the green laser (2.33 eV) excitation power (1–50 μW) at low temperature (5 K). The most important results are depicted in Fig. 5.7. All PL data are recorded with the laser power step of 1 μW.

In accordance with [23], the PL signal of interlayer excitons consists of two main peaks, IX and IX^*, which are defined above in subsubsection 5.3.2.1 and their phonon-assisted replicas. All of them could be described with Gaussian lineshapes.

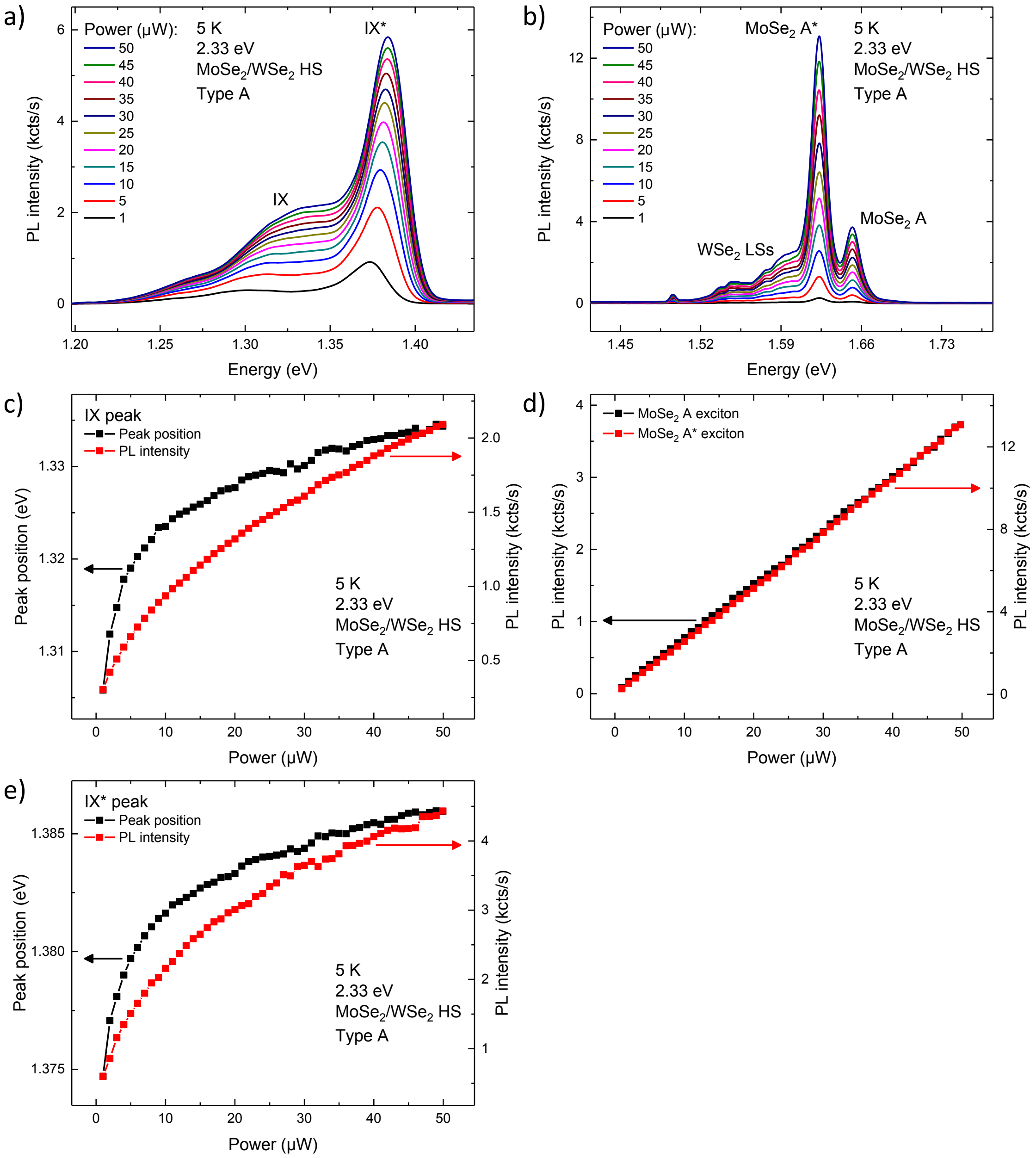

Fig. 5.7 Power dependence of the IX (left column) and DX (right column) emission in the type-A MoSe$_2$/WSe$_2$ HS. Temperature: 5 K. (a)–(b) The PL spectra under 1–50 μW laser excitation at 2.33 eV. All distinct inter- and intralayer excitonic peaks and bands are marked. The power-dependent (c) IX and (e) IX^* peak parameters, namely the peak positions (black, left vertical scale) and their intensities (red, right vertical scale), obtained from the fitting as described in the text. (d) The PL intensities of the MoSe$_2$ A and A^* exciton peak maxima as functions of excitation power.

Using this approach, we apply fitting to the power-dependent IX PL spectra to extract spectral parameters of IX and IX^*, such as the PL peak positions and their intensities (Fig. 5.7c,e). The intralayer exciton emission contains contributions from both $MoSe_2$ and WSe_2 excitonic peaks and localized state band (Fig. 5.7b). The origin of most of these peaks is unclear except for $MoSe_2$ A and A^*. Therefore, the DX PL signal is not fitted and the peak parameters are taken from the peak maxima. The PL of the intralayer $MoSe_2$ neutral and charged excitons is only analysed in the DX spectral range. No energy shifts of these peaks with excitation power are observed. Their PL intensities are presented in Fig. 5.7d.

In contrast to [20] which reports the power dependence of the total IX emission, we separately examine the data of the peaks of the interlayer excitons and trions in Fig. 5.7c,e. Both IX and IX^* demonstrate nonlinear power response and energy blueshift as shown in [20]. The low power saturation indicates that the indirect neutral and charged excitons have much longer lifetime in comparison with the intralayer excitons [20] and occupy limited number of states in accordance with the Pauli blocking principle. Localization by the potential traps provided by the impurities in the heterobilayers [23] and extended lifetimes increase the repulsive interactions between the IX complexes [20]. These interactions cause the emission blueshift with pumping. From our experiments, the interlayer exciton peak position shift is bigger than that for the interlayer trion peak in the power range of 1–50 μW: 28.5 meV against 11.2 meV. It could be interpreted that the trapping process by the donor ions is energetically more likely for indirect excitons (two-particle complexes) than for indirect trions (three-particle complexes). Additionally, the IX peak is much broader than IX^* (Fig. 5.7a). Such broadening could be a signature of stronger repulsive interaction effect.

Intralayer excitons have much shorter lifetime relative to indirect excitons and thus they do not show any power saturation and peak position shifts in our laser power range [20] (Fig. 5.7b,d). This is consistent with the published results about the excitonic peaks in the WSe_2 and $MoSe_2$ monolayers [45, 46].

5.3.2.3 Gate voltage dependence of photoluminescence

The influence of the carrier concentration with the gate voltage V_g on the low-temperature (6 K) type-B IX PL signal is described in this subsubsection. The schematic of the sample structure is given in Fig. 5.1b where no additional vertical electric field is possible to be applied. The electrostatic doping has been performed only via the monolayer $MoSe_2$. V_g has been varied from -90 V to +90 V with the step of 3 V. The electric gate current I has been monotonically changed from +1 nA to -3 nA. Maximal electron (hole) concentration has been penetrated into the HS at +90 V (-90 V). Calculated by means of the relation in Eq. (4.3), the density of injected electrons has been approximately equalled to 6.6×10^{10} cm^{-2} at each voltage increase of 1 V. Fig. 5.8 demonstrates the normalized PL spectra and gate-voltage-dependent IX peak positions and intensities taken from peak maxima.

A giant sublinear IX peak position blueshift of 96 meV is observed on the whole range of the electron doping (Fig. 5.8b). Simultaneously, the PL intensity is almost linearly quenched by more than 10.5 times. Also, a weak signal of the interlayer trions appears at $V_g \to +90$ V. According to the results in chapter 4, the above-mentioned behaviour of indirect excitons is similar to the low-temperature gate voltage dependence of the spectral parameters of the monolayer $MoSe_2$ neutral exciton peak. This may be probable because the IX complexes are formed from intralayer excitons through the ultrafast charge transfer [10, 18–21]. The energy blueshift of the A peak position with the electron doping is originated from the Pauli exclusion principle and screening of the Coulomb interaction in the single-layer TMDCs [44, 47]. The big shift values for the IX peak are supposed to be a result of the strong repulsive interactions between long-lived indirect excitons [20]. Therefore, this effect may significantly decrease the intensity of the interlayer exciton peak.

The large IX emission tuning could be caused the presence of other phenomena. The comparable energy shift by about 60 meV has been found by Rivera *et al.* [20] in the $MoSe_2/WSe_2$ heterobilayer with top gate and occurred because of a combination of the carrier injection and vertical electric field effects. Further investigations are still required to elucidate the physics of the presented processes.

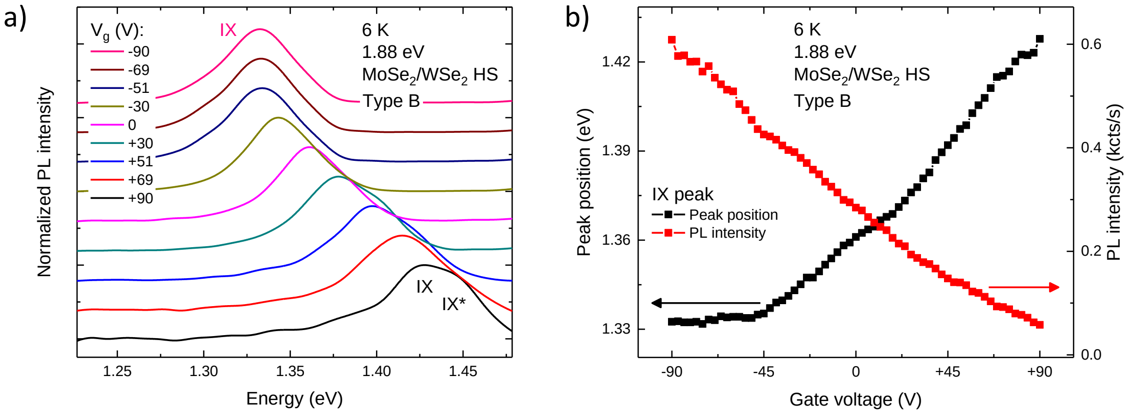

Fig. 5.8 The electrical control of the IX emission in the type-B $MoSe_2/WSe_2$ HS. (a) The vertically stacked gate-voltage-dependent normalized PL spectra under 20 μW laser excitation at 1.88 eV and temperature of 6 K. The applied gate voltage: -90 V $\leq V_g \leq +90$ V. The electron concentration is increased when going to +90 V. IX and IX^* indicates peak positions for indirect neutral and charged exciton complexes, respectively. (b) The IX peak parameters, namely the peak positions (black, left vertical scale) and its intensities (red, right vertical scale), as functions of V_g.

5.3.2.4 Temperature dependence of photoluminescence

This subsubsection discusses the impact of temperature on PL of both type-B IX and DX signals. Fig. 5.9 contains the main data including PL spectra and their parameters (peak positions and intensities).

At low temperatures, the PL of the intralayer excitons is dominated by the A^* trion peak in $MoSe_2$ (Fig. 5.9c). No visible DX emission from the WSe_2 monolayer in the HS is collected. As considered in subsubsection 5.3.2.1, the interlayer excitonic signal mainly consists of the IX peak. With increased temperature, the whole signal is redshifted and quenched (Fig. 5.9a–b). A similar effect has been observed in some individual TMDC monolayers [48–51] and is related to temperature-activated non-radiative recombination processes. Thermalization changes the ratio between the peak areas of intralayer excitons and trions: $MoSe_2$ A^* is only identified up to 40 K while $MoSe_2$ A is recognized from 50 K. The IX peak survives up to 90 K. Its energy redshift equals 21 meV. The PL intensities of all IX and DX peaks are almost unchanged for 5.6–25 K and demonstrate rather linear decrease in a logarithmic scale at higher temperatures (Fig. 5.9b).

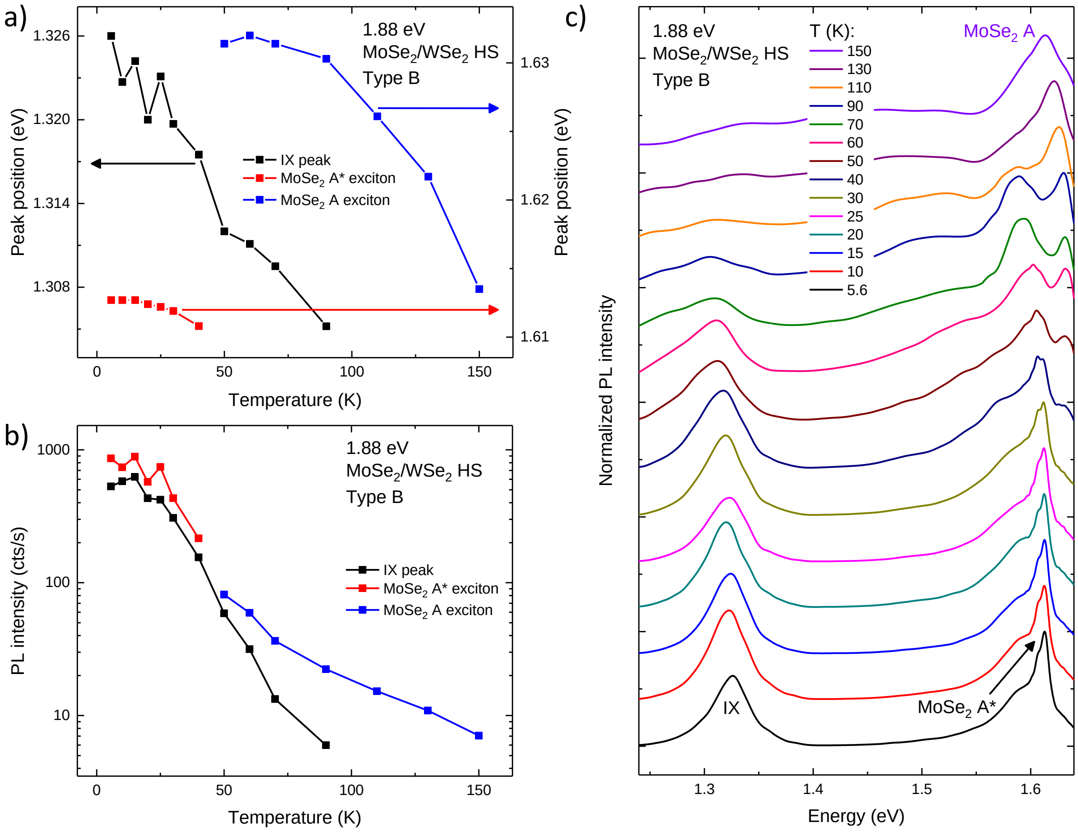

Fig. 5.9 Temperature dependence of the IX and DX emission in the type-B MoSe$_2$/WSe$_2$ HS. (c) The vertically stacked temperature-dependent normalized PL spectra under ~ 20 μW laser excitation at 1.88 eV. Temperature is increased from 5.6 K to 150 K. IX, $MoSe_2\ A$ and $MoSe_2\ A^*$ denotes peak positions for corresponding excitonic states. (a) Peak positions and (b) their intensities obtained from peak maxima as functions of temperature. Spectral parameters for IX (black), MoSe$_2$ A^* (red) and MoSe$_2$ A (blue) are shown.

5.3.2.5 Photoluminescence excitation measurements

The low-temperature (5 K) measurements of the IX PL signal in the non-encapsulated MoSe$_2$/WSe$_2$ heterobilayer are carried out using PLE spectroscopy. All important results of these experiments are depicted in Fig. 5.10 and presented below.

The PLE intensity plot is measured within the HS (Fig. 5.10a). The continuous-wave laser light with energies covering a range of the DX PL (from 1.518 eV to 1.762 eV) excites the signal of the interlayer excitons. The excitation energies which are equal to the PL peak positions of the intralayer excitons are marked on the intensity plot. Some spectra from this intensity map are separately plotted in Fig. 5.10b as examples. The IX and IX^* peaks, mentioned in previous subsubsections, sig-

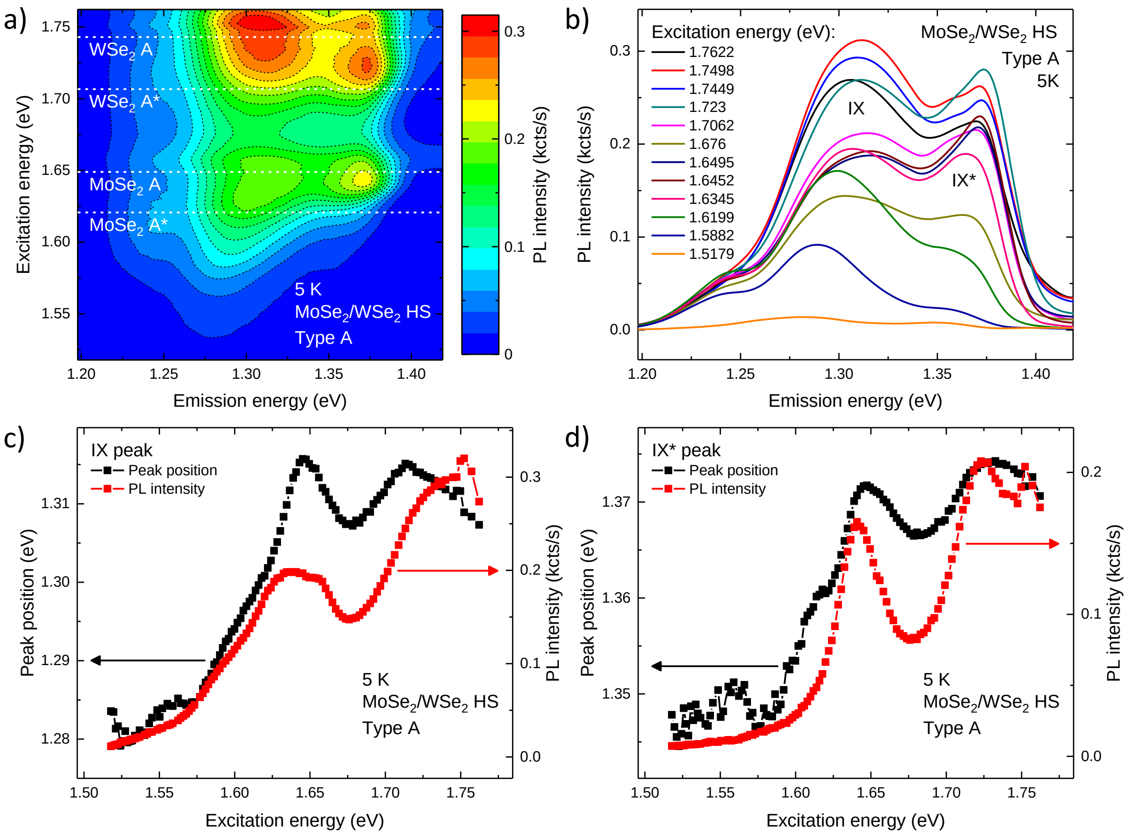

Fig. 5.10 PLE spectroscopy of interlayer excitons in the type-A $MoSe_2/WSe_2$ HS. Temperature: 5 K. (a) The PLE intensity map of the IX emission under 20 μW laser excitation in energy range of the DX emission (1.518–1.762 eV). Excitation energies corresponding to the PL peak positions of $MoSe_2$ and WSe_2 intralayer excitons and trions obtained from the individual monolayers on the same sample are denoted by white dashed lines. (b) Some selective spectra from the PLE measurements. The values of laser energy are specified in the legends of the plots. IX and IX^* indicates peak positions for indirect neutral and charged excitons, respectively. (c)–(d) Spectral fitting parameters, namely the peak positions (black) and PL intensities (red) for IX (left) and IX^* (right) as functions of laser excitation energy.

nificantly change their spectral shapes with the variable laser excitation. We fit the IX emission with Gaussian functions [23] to get peak positions and intensities (Fig. 5.10c–d).

Similarly to [20], the enhancement of the IX emission occurs when the laser excitation energies are close to the DX PL peak positions (Fig. 5.10). In this case, both the neutral and charged interlayer exciton peaks rise, but it is difficult to deduce what intralayer exciton state (A or A^*) causes bigger increment of the IX signal. Such increase of the IX and IX^* peaks confirms the existence of the ultrafast interlayer charge hopping [10, 18–21] through the 2D $MoSe_2/WSe_2$ heterojunction. Additionally, the laser light resonant with the single-layer WSe_2 DX PL generates stronger emission of indirect excitons than that resonant with A and A^* in the monolayer $MoSe_2$. We assume that the high-energy excitation of about 1.71–1.74 eV which includes the DX peak positions of the WSe_2 atomic layer forms intralayer excitons in both $MoSe_2$ and WSe_2 monolayers of the HS. Then, these excitons transform into localized IX complexes. However, it is impossible to excite intralayer excitons in the WSe_2 single layer with the light which is in resonance with the monolayer $MoSe_2$ DX PL signal ($\sim$ 1.62–1.65 eV). This explains the above effect.

Another feature which we observe with the mentioned intensity enhancement of the IX peaks is their energy blueshifts by a few meV (Fig. 5.10c–d). At excitation energies resonant with intralayer exciton states, the charge carrier transfer is enlarged in the heterobilayer. As a result of this and extended lifetimes of indirect excitons [20], the quasi Fermi levels of electrons and holes are increased owing to Pauli blocking and therefore, the IX emission is blueshifted. Any shifts at laser energies less than 1.57 eV are suggested to be artificial because of the weak signal of interlayer excitons.

5.3.3 Photoluminescence of $MoSe_2/WS_2$ heterostructure

The $MoSe_2/WS_2$ HS possesses a specific band structure which reflects on the excitonic properties. Some important results received from our PL measurements of this HS are outlined here. As in the previous subsection 5.3.2, the details on the experimental methods, sample and set-up descriptions are written in section 5.2 and chapter 2.

5.3.3.1 Photoluminescence spectral peaks and polarization

As described in 5.1, due to the very small (20–60 meV [6, 7]) calculated conduction band offset in the $MoSe_2/WS_2$ heterobilayer, the IX PL signal is predicted to be extremely close to the DX emission in the monolayer $MoSe_2$ [34–36] (Fig. 5.11a). In Fig. 5.11b, we compare the low-temperature (6 K) PL obtained from the individual single-layer $MoSe_2$ and HS to identify the latter. It is clearly visible that difference between signals equals a few tens of meV which proves that the above signals are

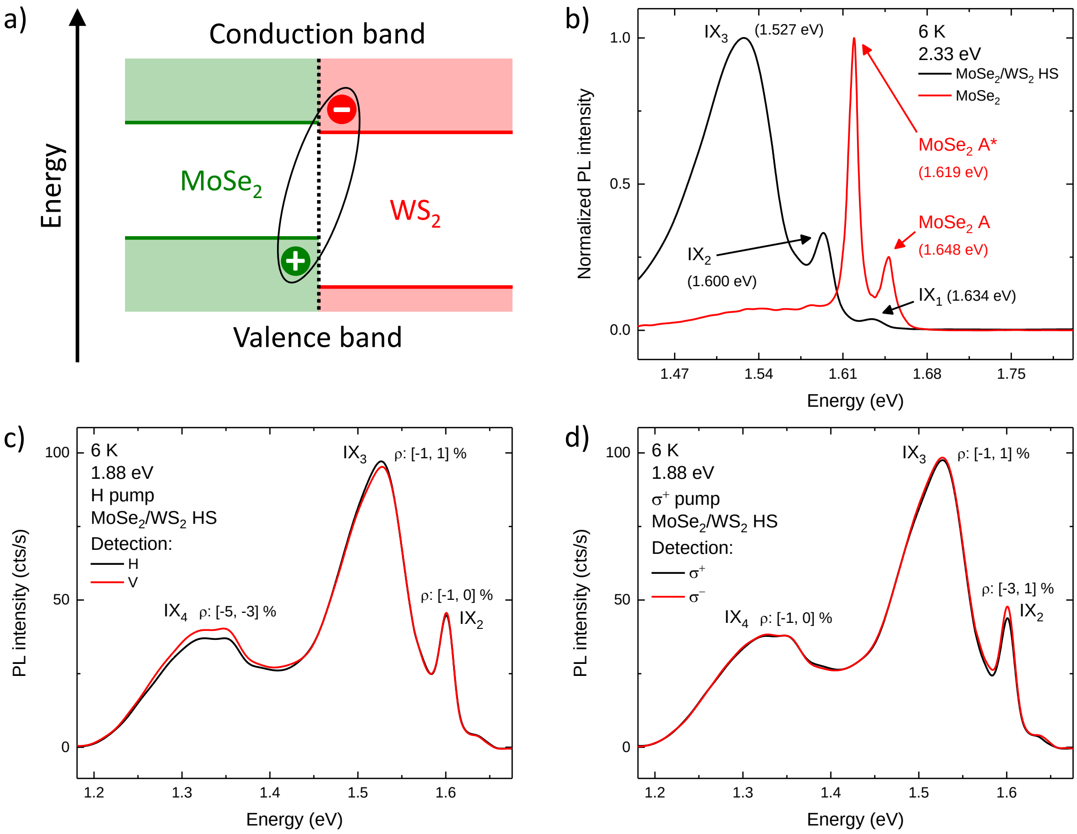

Fig. 5.11 The PL of the MoSe$_2$/WS$_2$ HS and its polarization. (a) The drawing of type-II band alignment in the MoSe$_2$/WS$_2$ HS. The energy levels of the MoSe$_2$ and WS$_2$ conduction bands are almost coincided and this predefines the specific behaviour of excitonic complexes. Energy axis has vertical direction. (b) The comparison of PL signals taken from the HS (black) and individual MoSe$_2$ monolayer (red) on the same sample. All visible peaks and their positions are marked. Parameters of the applied laser excitation: 2.33 eV, 20 μW. Temperature: 6 K. (c)–(d) The low-temperature (6 K) polarization-resolved PL spectra under the H linearly (left) and σ^+ right circularly (right) polarized laser excitations at power of 20 μW and energy of 1.88 eV. Data with the same ('opposite') emission detection are coloured in black (red). The 'opposite' emission means the σ^- left circularly and V linearly (perpendicularly to H) polarized signal. ρ denotes the degree of polarization (in percent). All distinct peaks and their average ranges of the corresponding polarization are indicated.

not the same. Additionally, any significant emission of monolayer $\mathrm{MoSe_2}$ and $\mathrm{WS_2}$ intralayer excitons is not observed in the HS at low temperatures.

Nevertheless, the nature of the PL taken from the $\mathrm{MoSe_2/WS_2}$ heterobilayer is still unclear. Instead of two peaks corresponding to interlayer excitons and trions, it consists of three peaks which we call as IX_1, IX_2 and IX_3 (Fig. 5.11b). The spectral band IX_4 at 1.25–1.40 eV (Fig. 5.11c–d) is probably related to localized states. All these peaks and bands will demonstrate the optical properties different from those presented in subsection 5.3.2 for the $\mathrm{MoSe_2/WSe_2}$ HSs.

Using polarization-resolved PL spectroscopy, it is established that the signal of the HS does not show any reasonable linear and circular polarization (Fig. 5.11c–d). The degree of polarization of each peak (except for IX_4) as defined in subsubsection 2.2.1.2 does not exceed several percent. We can conclude that the valley physics which works in the individual TMDC monolayers [30, 52, 53] is neglected in such stacked structures. The reason for this could be an encapsulation during the sample fabrication. The linear polarization of IX_4 by down to -5 % is supposed to be strain-induced under the capped hBN layer on top of the sample.

5.3.3.2 Power dependence of photoluminescence

Fig. 5.12 represents the PL power dependence measurements at low temperature of 6 K. The applied excitation has energy of 1.88 eV in a power range of about 1–100 μW with the approximate step of 5 μW.

Some PL spectra as examples are shown in Fig. 5.12a. We individually measure the IX_4 band (Fig. 5.12b) since it is positioned far enough from the rest of peaks. Because the structure of the main PL in the range of 1.40–1.65 eV is unknown, only distinct peaks, specifically IX_2 and IX_3, are analysed using values of their positions and intensities taken from peak maxima (Fig. 5.12c). Also, the same power-dependent spectral parameters are obtained for IX_4 (Fig. 5.12d). The IX_2 and IX_3 peak positions are not plotted as they fluctuate by only a few meV without any clear tendency.

The PL intensities of IX_2 and IX_3 are characterized with linear and slightly sub-

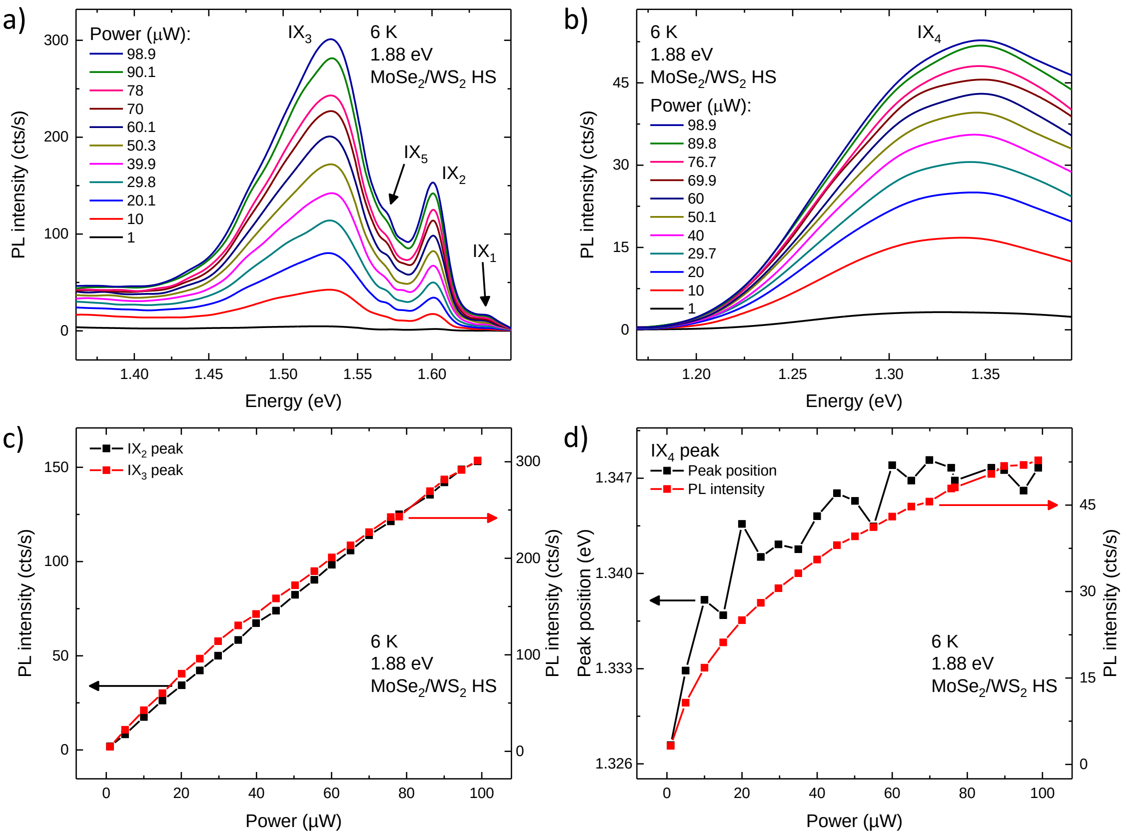

Fig. 5.12 Power dependence of the PL signal in the MoSe$_2$/WS$_2$ HS. Temperature: 6 K. The applied laser excitation: 1.88 eV, ∼ 1–100 μW. (a) Some power-dependent PL spectra. All visible peaks including IX_5 which will be discussed in subsubsection 5.3.3.3 are indicated. The emission of the IX_4 band is separately measured and presented in (b). (c) The PL intensities from peak maxima for IX_2 (black, left vertical scale) and IX_3 (red, right vertical scale) as functions of laser power. (d) Power dependence of the peak position (black, left vertical scale) and intensity (red, right vertical scale) of the IX_4 band.

linear dependence on laser power, respectively, in Fig. 5.12c. For the latter dependence, such strong power saturation as for interlayer excitons in the MoSe$_2$/WSe$_2$ HS is not observed. The IX_2 and IX_3 excitonic states behave more as neutral and charged excitons in the individual TMDC monolayers with almost linear low power dependence of their PL peaks [45, 46, 50, 54, 55].

The IX_4 band markedly saturates with excitation power (Fig. 5.12d). In addition to this, the signal is blueshifted by ∼ 21 meV in the whole power range. Consequently, the power-dependent behaviour of IX_4 is similar to those for the peaks of the IX complexes in the MoSe$_2$/WSe$_2$ HS (Fig. 5.7c,e). However, this spectral band is located far from the excitonic peaks in the individual single-layer MoSe$_2$ and hence likely emitted by localized states (not IXs).

5.3.3.3 Gate voltage dependence of photoluminescence

The electrical control of the PL signal in the $MoSe_2/WS_2$ heterobilayer with the gate voltage V_g is also studied at low temperature (6 K). The sketch of the sample structure is similar to Fig. 5.1b but without HfO_2 capping. It is clearly seen that no additional vertical electric field is possible to be applied because there is no top gate contact on the HS. The electrostatic doping has been performed only via the monolayer $MoSe_2$. V_g has been changed from -20 V to +20 V (with the step of 2 V) while the electric gate current has been decreased from nearly +1 nA to -2 nA, respectively. The injected electron charge has been maximal at +20 V whereas each voltage increase of 1 V has been equivalent to a doping density of $\sim 1.6 \times 10^{11}$ cm^{-2} calculated by the relation in Eq. (4.3). Fig. 5.13 demonstrates our experimental results on this topic.

As in previous subsubsection 5.3.3.2, the IX_4 band and rest of peaks are separately measured (Fig. 5.13a–b). The electron injection into the originally n-doped HS leads to a complete quenching of almost all peaks. Only the unknown IX_5 peak at about 1.57 eV arises under high positive V_g. Interestingly, it is also observed as a 'shoulder' in the power-dependent spectra in Fig. 5.12a.

The positions and intensities of the most distinct IX_2, IX_3 peaks and IX_4 band are extracted from the data using the peak maxima (Fig. 5.13c–e). No clear gate-voltage-dependent trend for IX_4 band maximum shifts is recorded other than fluctuations around 1.335 eV by several meV. Therefore, these positions are not depicted in Fig. 5.13d. Additionally, the IX_2 and IX_3 peak parameters are only plotted up to +10 V and IX_4 up to -2 V due to the weak emission and noisy spectral shape for higher electron concentration.

Except for the gradual decrease of the IX_4 PL intensity, no significant changes in spectral parameters of other peaks occur at gate voltages from -20 V to $\sim$ +6 V (Fig. 5.13c–e). Under V_g applied in another direction (from +20 V to -20 V), the above range of rather 'frozen' parameters is much less and IX_4 is varied in a smaller

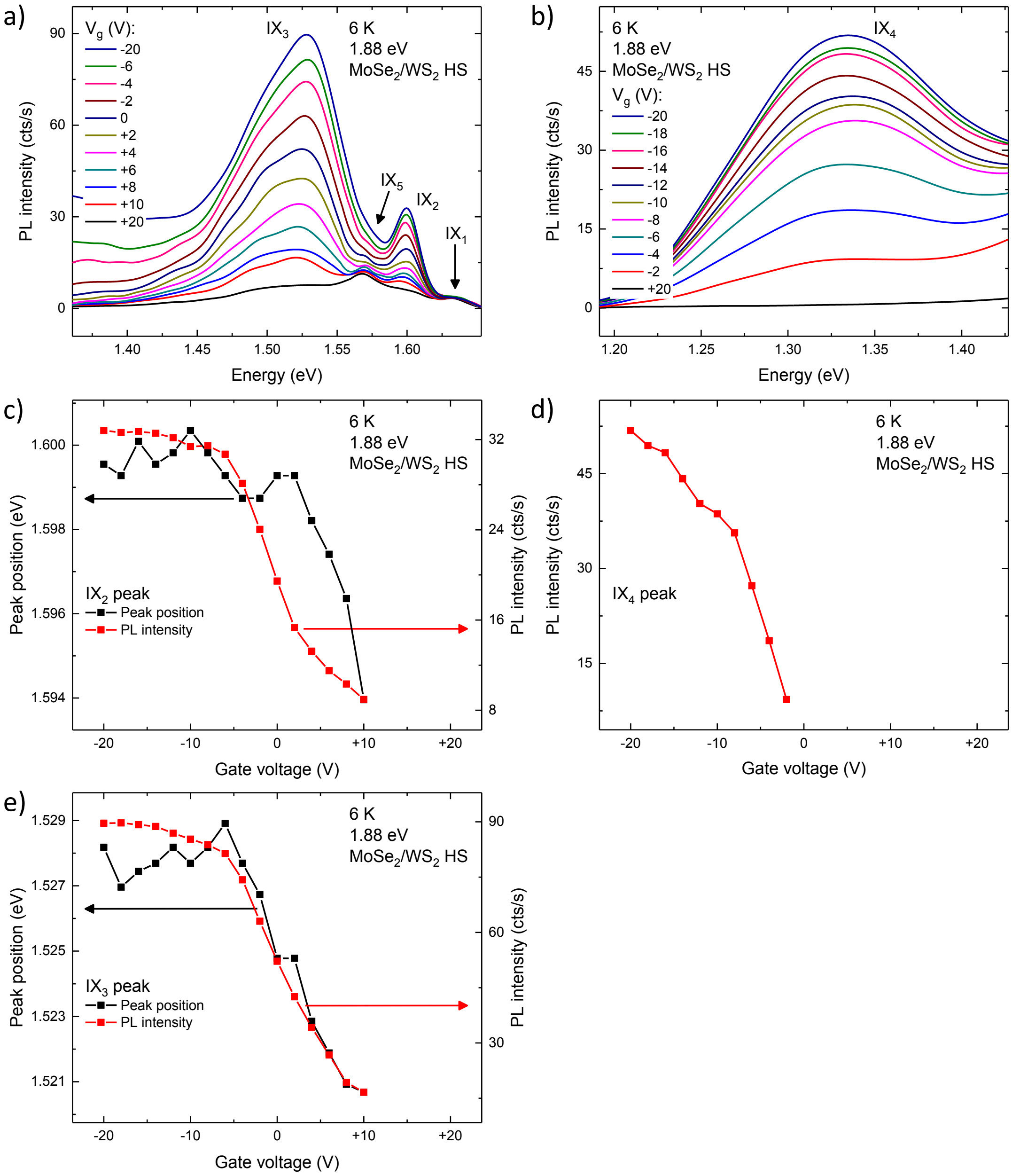

Fig. 5.13 The electrical doping in the $MoSe_2/WS_2$ HS. Temperature: 6 K. The applied laser excitation: 1.88 eV, 20 μW. The applied gate voltage: $-20\text{ V} \leq V_g \leq +20\text{ V}$. The electron concentration is increased when going to +20 V. (a) Some gate-voltage-dependent PL spectra. All visible peaks are marked. The signal of IX_4 is individually measured and presented in (b). The (c) IX_2 and (e) IX_3 peak parameters, namely the peak positions (black, left vertical scale) and their intensities (red, right vertical scale), as functions of V_g. (d) Dependence of the IX_4 band PL intensities on gate voltage.

range. Thus, we could suggest that this effect is concerned with a hysteresis. Since $V_g = +6$ V at higher electron concentration, the IX_2 and IX_3 peak maxima are dramatically dropped and slightly redshifted by 5–8 meV. Further investigations should be performed in future to understand the gate-voltage-dependent peak variations in the $MoSe_2/WS_2$ HS.

5.3.3.4 Temperature dependence of photoluminescence

The evolution of the PL of the vertically stacked 2D $MoSe_2/WS_2$ structure with temperature growth from 5.4 K to 300 K is viewed in Fig. 5.14.

Similarly to the behaviour of the IX PL peaks in the $MoSe_2/WSe_2$ HS (subsubsection 5.3.2.4) as well as the PL signal in the individual TMDC monolayers [48–51], the emission in the $MoSe_2/WS_2$ heterobilayer is redshifted and reduced with temperature. The IX_2 peak is detected even at room temperature while other spectral features disappear up to 90 K. The signal of intralayer excitonic states of the WS_2 atomic layer becomes visible at high temperatures (Fig. 5.14c).

The temperature-related modifications of intensities of the main PL (IX_1, IX_2, IX_3 and IX_4) can be divided by several temperature ranges (Fig. 5.14b). At low temperatures of 5.4–25 K, the whole signal does not change too much (the IX_4 spectral band is even slightly enlarged). Then at 25–90 K, almost all peaks (except for IX_2) are drastically decreased and finally vanished. However, the PL intensity of IX_2 is practically the same at temperatures from 60 K to 90 K. At elevated temperatures of 90–300 K, rather linear dropping in a logarithmic scale of the IX_2 peak intensity is recorded.

As in the case of the PL signal in the individual single-layer TMDCs [48–50], the temperature-dependent trends of the IX_1, IX_2 and IX_3 peak positions in Fig. 5.14a can be fitted using the O'Donnell *et al.* [56] formula describing the temperature dependence of semiconductor band gaps. In addition, data for IX_2 are consistent with the Varshni relation [57]. The fitting analysis will be presented in subsection 5.4.2. The curve corresponding to the positions of the IX_4 band (Fig. 5.14a) is formed with straggling points and so not fitted.

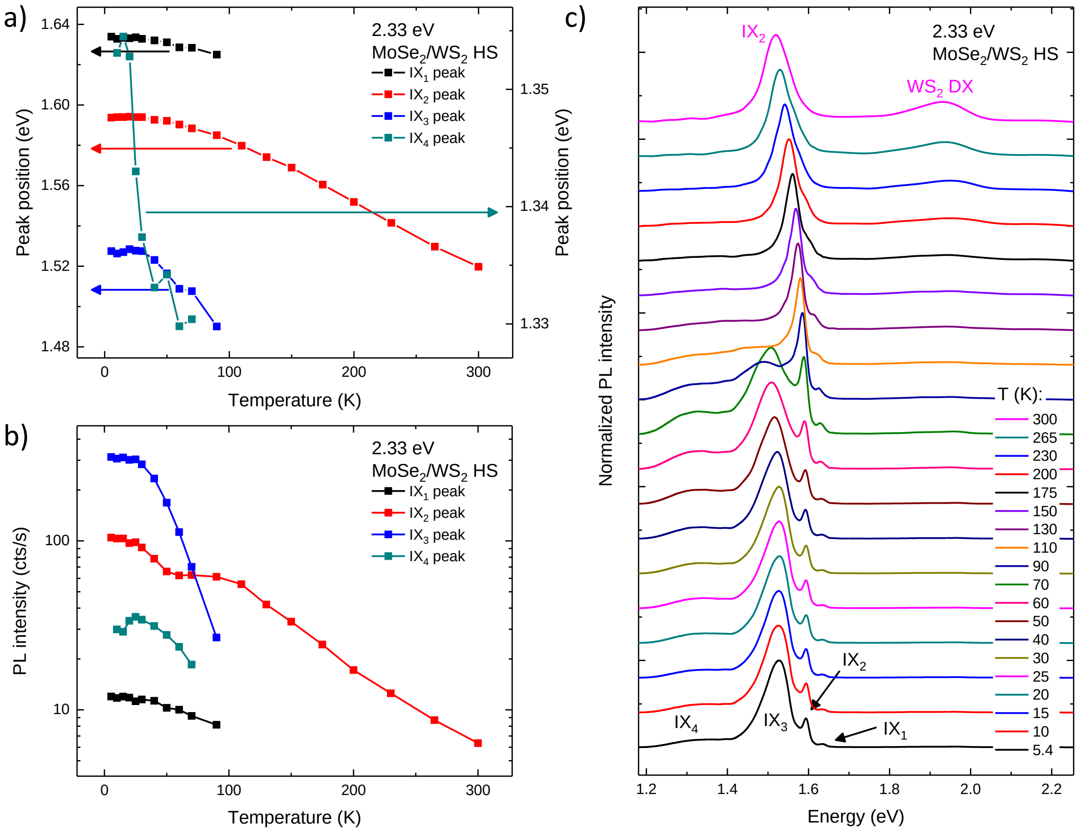

Fig. 5.14 Temperature dependence of the emission in the MoSe$_2$/WS$_2$ HS. (c) The vertically stacked temperature-dependent normalized PL spectra under 20 μW laser excitation at 2.33 eV. Temperature is increased from 5.4 K to 300 K. All visible peaks are denoted. (a) Peak positions and (b) their intensities taken from peak maxima as functions of temperature. Spectral parameters for IX_1 (black), IX_2 (red), IX_3 (blue) and IX_4 (dark cyan) are shown.

5.4 Discussion

5.4.1 Effects of valley polarization and encapsulation on interlayer excitons in MoSe$_2$/WSe$_2$ heterostructures

Analysing our experimental outcome obtained for the non-encapsulated MoSe$_2$/WSe$_2$ HS, we can confirm that the valley-related polarization of the emission is inherent to the indirect excitons. This is in agreement with earlier results [27] which show that the spin-valley physics of the constituent monolayers is retained during the interlayer charge transfer through the heterointerface. The initially created photoexcited valley intralayer excitons of the individual TMDC monolayers preserve the circular helicity of the incident laser excitation [30, 52]. Also at higher and more detuned laser energy from the DX band-gap energies, less DX PL circular polarization is generated because of phonon-assisted intervalley scattering [30, 58]. Therefore, the distinct circular polarization of the IX emission as well as the above excitation-energy-dependent effect are observed in the type-A samples (subsubsection 5.3.2.1). Additionally, no significant IX PL linear polarization is detected under the linearly polarized laser light. In the single-layer WSe_2, such linear polarization of the signal is a signature of excitonic valley coherence [52]. We suggest that our aligned HSs consisting of the exfoliated monolayers are on the whole incommensurate with slight interlayer twist and/or lattice mismatch [28]. This may produce the absence of the valley coherence. Nevertheless, the fundamental mechanisms of the IX valley polarization still need to be examined to achieve better understanding.

The HfO_2/hBN encapsulation completely changes the polarization properties of the IX PL in the type-B $MoSe_2/WSe_2$ HS. From the polarization-resolved PL measurements, the pronounced linearly and negligible circularly polarized IX signals are usually emitted under the corresponding type of the optical excitation (subsubsection 5.3.2.1). We assume that these polarization features are caused with a mechanical capping-induced strain and deformations of crystal lattices in the HS. Several arguments confirm our suggestion. First in contrast to the type-A IX and IX^* spectral peaks which mainly demonstrates the same helicity to the incident laser light, the emission of the interlayer excitons in the capped heterobilayer can exhibit both positive and negative values of the degree of linear or circular polarizations. There are almost unpolarized signals in some measurement points (Fig. 5.6e–f). Second, the IX peak linear polarization is weakly dependent on the photo-excitation energy (Fig. 5.5b,d). Third, direction of its polarization axis is varied from point to point without any clear tendency (Fig. 5.6). Finally as mentioned in subsubsection 5.3.2.1, there are random energy shifts between IX peak maxima taken at different detection angles from the same measurement points under the incident fixed linearly polarized laser beam. All the above facts maintain our opinion that indirect excitons do not possess the valley optical selection rules and the mechanical strain modifies the IX spectral shape after the HfO_2/hBN capping process.

The peak structure of the IX PL of the encapsulated samples is also distinguished from that for the type-A hybrid bilayer. Instead of two peaks, IX and IX^*, related to localized interlayer neutral and charge exciton complexes [23], one broad spectral band with maximum at the IX peak energy position is generally presented in the PL spectra (subsubsection 5.3.2.1). Hence, the encapsulation process possibly alters an intrinsic charge carrier concentration in the HS so that the interlayer trion formation becomes to be imperceptible. However, capping could also play another role according to available other interpretations of the origin of IX signal components. In accordance with [32], the IX spectral doublet shape of our non-encapsulated $MoSe_2$/WSe_2 heterobilayers is derived from the existence of both direct- and indirect-bandgap transitions for interlayer excitons in reciprocal space. The low-energy peak is concerned with phonon-involved momentum-indirect recombination whereas the high-energy peak with momentum-quasi-direct recombination. On the other hand, this double IX emission could come from the spin-orbit split transitions which are indirect in momentum space [59]. In addition, the suggested interlayer hybridization of electron states makes those transitions partially direct in real space. Nevertheless, we can conclude from our observations that the strain and crystal lattice deformations induced by the capped HfO_2/hBN may transform the band structure of the type-B HS and only one distinct optically bright transition is dominant. More experimental results and theoretical calculations are required to explore this topic in detail.

5.4.2 Temperature evolution of emission in $MoSe_2$/WS_2 heterostructure

The temperature-activated redshifts of excitonic spectral peak positions are typical to a large variety of semiconductors and originated from phonon scattering. A classical relation describing this effect is the semi-empirical Varshni equation in which the energy gap E_g is varied with temperature T [57]:

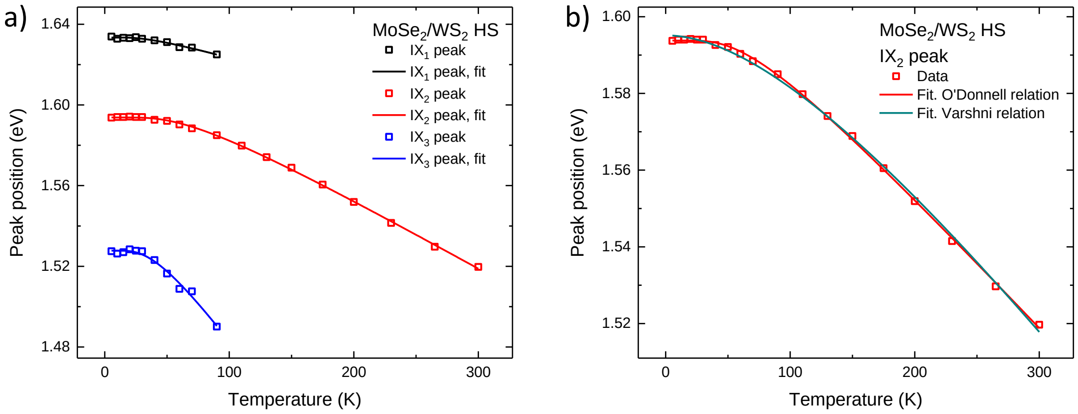

Fig. 5.15 The fitting of the temperature-dependent peak positions in the MoSe$_2$/WS$_2$ HS. (a) The IX_1 (black), IX_2 (red) and IX_3 (blue) peak positions (unfilled dots) along with the corresponding fits (solid lines) as functions of temperature. The fitting is performed using Eq. (5.2). (b) The comparison of the fits (solid lines) under the Varshni (dark cyan) and O'Donnell (red) relations for the temperature-dependent IX_2 peak positions (red unfilled dots).

$$E_g(T) = E_0 - \frac{\alpha T^2}{T + \beta}, \tag{5.1}$$

where E_0 is the band gap at zero temperature (0 K), α and β are material constants (fitting parameters) which characterize the temperature-related dilatation of the lattice and Debye temperature. The expression proposed by O'Donnell *et al.* [56] represents the same relationship but with numerically better fitting:

$$E_g(T) = E_0 - S\langle\hbar\omega\rangle \left[\coth\left(\frac{\langle\hbar\omega\rangle}{2kT}\right) - 1\right]. \tag{5.2}$$

$\langle\hbar\omega\rangle$ is the average phonon energy, k and S are the Boltzmann and dimensionless coupling constants, respectively.

Our data of the temperature-dependent IX_1, IX_2 and IX_3 peak positions in the MoSe$_2$/WS$_2$ heterobilayer are well fitted with the O'Donnell relation given by Eq. (5.2). Fig. 5.15a demonstrates the appearance of the fits. All fitting parameter values are gathered in Table 5.1. From our applied calculations, the Varshni formula is only suitable for IX_2 emission energies. Comparing the results, we note that both considered fits for the IX_2 peak positions are acceptable (Fig. 5.15b). The best fitting based on the Varshni equation for the IX_2 transition energy values is achieved

Table 5.1 The fitting parameters for the temperature-dependent IX_1, IX_2 and IX_3 peak positions in the $MoSe_2/WS_2$ HS. All parameters are taken from the fitting based on the O'Donnell formula.

Parameter	IX_1 peak	IX_2 peak	IX_3 peak
E_0 (eV)	1.633 ± 0.001	1.594 ± 0.001	1.528 ± 0.001
$\langle\hbar\omega\rangle$ (meV)	9 ± 2	17 ± 1	11 ± 2
S	1.02 ± 0.17	2.03 ± 0.03	5.10 ± 0.72

with $E_0 = 1.595 \pm 0.001$ eV, $\alpha = (4.7 \pm 0.3) \times 10^{-4}$ eV·K^{-1} and $\beta = 243 \pm 35$ K.

Except for the values of the zero-temperature band gap E_0, all obtained parameters are comparable to those from previous studies of excitonic peaks in the single-layer TMDCs [48–51, 54, 60–62]. Especially, the constants for IX_2 are in a good agreement with the constants for the exciton and trion spectral peaks in the monolayer $MoSe_2$ [49]. Also as discussed in subsubsection 5.3.3.2, the PL intensities of the IX_2 and IX_3 peaks show rather linear low-power-dependent trends without any strong power saturation and this is similar to the behaviour of neutral and charged exciton PL peaks in the TMDC atomic layers [45, 46, 50, 54, 55]. All these facts give us an opportunity to suggest that the observed peaks in the $MoSe_2/WS_2$ HS are the PL signals of excitonic states with hybridized electrons between the layers. There is no evidence to assume that such the hybrid bilayer forms the sharp staggered heterojunction with the IX complexes.

5.5 Conclusions

In summary, the excitonic properties of the vertically stacked TMDC-based hetero-bilayers, namely $MoSe_2/WSe_2$ and $MoSe_2/WS_2$, are investigated using PL and PLE spectroscopies. For the $MoSe_2/WSe_2$ HSs, the impact of the HfO_2/hBN encapsulation on the structure and polarization of the IX emission are first demonstrated. Our measurements of power and gate voltage dependences confirm the localized nature of interlayer excitons, their long lifetimes and strong repulsive interactions. In addition to the aforementioned properties of indirect excitons, the evidence of the IX formation via the charge carrier transfer is clearly presented in the PLE experiments. The influence of the thermalization effect on these hybrid bilayers is also included. More complicated structure of the PL signal consisting of the variety of spectral peaks is observed in the $MoSe_2/WS_2$ HS. The study of this PL through the power, gate voltage and temperature dependence measurements gives us more arguments to suggest that the states corresponding to these PL peaks are not purely indirect in real space and derived from the interlayer electron hybridization. The material systems engineered by van der Waals stacking of TMDC monolayers and other 2D films open up new possibilities in achieving rich functionality and extraordinary optoelectronic properties which are useful in making novel ultrathin photovoltaic devices.

References

[1] A. K. Geim, I. V. Grigorieva. Van der Waals heterostructures. *Nature* **499**, 419–425 (2013).

[2] A. Ramasubramaniam. Large excitonic effects in monolayers of molybdenum and tungsten dichalcogenides. *Phys. Rev. B* **86 (11)**, 115409 (2012).

[3] A. Chernikov, T. C. Berkelbach, H. M. Hill, A. Rigosi, Y. Li, O. B. Aslan, D. R. Reichman, M. S. Hybertsen, T. F. Heinz. Exciton binding energy and nonhydrogenic Rydberg series in monolayer WS_2. *Phys. Rev. Lett.* **113 (7)**, 076802 (2014).

[4] T. Cao, G. Wang, W. Han, H. Ye, C. Zhu, J. Shi, Q. Niu, P. Tan, E. Wang, B. Liu, J. Feng. Valley-selective circular dichroism of monolayer molybdenum disulphide. *Nat. Commun.* **3**, 887 (2012).

[5] X. Xu, W. Yao, D. Xiao, T. F. Heinz. Spin and pseudospins in layered transition metal dichalcogenides. *Nat. Phys.* **10**, 343–350 (2014).

[6] J. Kang, S. Tongay, J. Zhou, J. Li, J. Wu. Band offsets and heterostructures of two-dimensional semiconductors. *Appl. Phys. Lett.* **102 (1)**, 012111 (2013).

[7] C. Gong, H. Zhang, W. Wang, L. Colombo, R. M. Wallace, K. Cho. Band alignment of two-dimensional transition metal dichalcogenides: application in tunnel field effect transistors. *Appl. Phys. Lett.* **103 (5)**, 053513 (2013).

[8] K. Kośmider, J. Fernández-Rossier. Electronic properties of the $\mathrm{MoS_2}$-$\mathrm{WS_2}$ heterojunction. *Phys. Rev. B* **87 (7)**, 075451 (2013).

[9] H. Terrones, F. López-Urías, M. Terrones. Novel hetero-layered materials with tunable direct band gaps by sandwiching different metal disulfides and diselenides. *Sci. Rep.* **3**, 1549 (2013).

[10] X. Hong, J. Kim, S.-F. Shi, Yu Zhang, C. Jin, Y. Sun, S. Tongay, J. Wu, Y. Zhang, F. Wang. Ultrafast charge transfer in atomically thin $\mathrm{MoS_2/WS_2}$ heterostructures. *Nat. Nanotechnol.* **9**, 682–686 (2014).

[11] L. Debbichi, O. Eriksson, S. Lebègue. Electronic structure of two-dimensional transition metal dichalcogenide bilayers from *ab initio* theory. *Phys. Rev. B* **89 (20)**, 205311 (2014).

[12] H. Heo, J. H. Sung, S. Cha, B.-G. Jang, J.-Y. Kim, G. Jin, D. Lee, J.-H. Ahn, M.-J. Lee, J. H. Shim, H. Choi, M.-H. Jo. Interlayer orientation-dependent light absorption and emission in monolayer semiconductor stacks. *Nat. Commun.* **6**, 7372 (2015).

[13] H. M. Hill, A. F. Rigosi, K. T. Rim, G. W. Flynn, T. F. Heinz. Band alignment in $\mathrm{MoS_2/WS_2}$ transition metal dichalcogenide heterostructures probed by scanning tunneling microscopy and spectroscopy. *Nano Lett.* **16 (8)**, 4831–4837 (2016).

[14] N. R. Wilson, P. V. Nguyen, K. Seyler, P. Rivera, A. J. Marsden, Z. P. L. Laker, G. C. Constantinescu, V. Kandyba, A. Barinov, N. D. M. Hine, X. Xu, D. H. Cobden. Determination of band offsets, hybridization, and exciton binding in 2D semiconductor heterostructures. *Sci. Adv.* **3 (2)**, e1601832 (2017).

[15] H. P. Komsa, A. V. Krasheninnikov. Electronic structures and optical properties of realistic transition metal dichalcogenide heterostructures from first principles. *Phys. Rev. B* **88 (8)**, 085318 (2013).

[16] S. Tongay, W. Fan, J. Kang, J. Park, U. Koldemir, J. Suh, D. S. Narang, K. Liu, J. Ji, J. Li, R. Sinclair, J. Wu. Tuning interlayer coupling in large-area heterostructures with CVD-grown MoS_2 and WS_2 monolayers. *Nano Lett.* **14 (6)**, 3185–3190 (2014).

[17] F. Wang, J. Wang, S. Guo, J. Zhang, Z. Hu, J. Chu. Tuning coupling behavior of stacked heterostructures based on MoS_2, WS_2, and WSe_2. *Sci. Rep.* **7**, 44712 (2017).

[18] H. Fang, C. Battaglia, C. Carraro, S. Nemsak, B. Ozdol, J. S. Kang, H. A. Bechtel, S. B. Desai, F. Kronast, A. A. Unal, G. Conti, C. Conlon, G. K. Palsson, M. C. Martin, A. M. Minor, C. S. Fadley, E. Yablonovitch, R. Maboudian, A. Javey. Strong interlayer coupling in van der Waals heterostructures built from single-layer chalcogenides. *Proc. Natl. Acad. Sci. U.S.A.* **111 (17)**, 6198–6202 (2014).

[19] F. Ceballos, M. Z. Bellus, H.-Y. Chiu, H. Zhao. Ultrafast charge separation and indirect exciton formation in a MoS_2–$MoSe_2$ van der Waals heterostructure. *ACS Nano* **8 (12)**, 12717–12724 (2014).

[20] P. Rivera, J. R. Schaibley, A. M. Jones, J. S. Ross, S. Wu, G. Aivazian, P. Klement, K. Seyler, G. Clark, N. J. Ghimire, J. Yan, D. G. Mandrus, W. Yao, X. Xu. Observation of long-lived interlayer excitons in monolayer $MoSe_2$–WSe_2 heterostructures. *Nat. Commun.* **6**, 6242 (2015).

[21] X. Zhu, N. R. Monahan, Z. Gong, H. Zhu, K. W. Williams, C. A. Nelson. Charge transfer excitons at van der Waals interfaces. *J. Am. Chem. Soc.* **137 (26)**, 8313–8320 (2015).

[22] H. Chen, X. Wen, J. Zhang, T. Wu, Y. Gong, X. Zhang, J. Yuan, C. Yi, J. Lou, P. M. Ajayan, W. Zhuang, G. Zhang, J. Zheng. Ultrafast formation of interlayer

hot excitons in atomically thin MoS_2/WS_2 heterostructures. *Nat. Commun.* **7**, 12512 (2016).

[23] M. Danovich, D. A. Ruiz-Tijerina, R. J. Hunt, M. Szyniszewski, N. D. Drummond, V. I. Fal'ko. Localized interlayer complexes in heterobilayer transition metal dichalcogenides. *Preprint at https://arxiv.org/abs/1802.06005* (2018).

[24] H. Yu, Y. Wang, Q. Tong, X. Xu, W. Yao. Anomalous light cones and valley optical selection rules of interlayer excitons in twisted heterobilayers. *Phys. Rev. Lett.* **115 (18)**, 187002 (2015).

[25] Y. Gong, J. Lin, X. Wang, G. Shi, S. Lei, Z. Lin, X. Zou, G. Ye, R. Vajtai, B. I. Yakobson, H. Terrones, M. Terrones, B. K. Tay, J. Lou, S. T. Pantelides, Z. Liu, W. Zhou, P. M. Ajayan. Vertical and in-plane heterostructures from WS_2/MoS_2 monolayers. *Nat. Mater.* **13**, 1135–1142 (2014).

[26] P. Rivera, K. L. Seyler, H. Yu, J. R. Schaibley, J. Yan, D. G. Mandrus, W. Yao, X. Xu. Valley-polarized exciton dynamics in a 2D semiconductor heterostructure. *Science* **351 (6274)**, 688–691 (2016).

[27] J. R. Schaibley, P. Rivera, H. Yu, K. L. Seyler, J. Yan, D. G. Mandrus, T. Taniguchi, K. Watanabe, W. Yao, X. Xu. Directional interlayer spin-valley transfer in two-dimensional heterostructures. *Nat. Commun.* **7**, 13747 (2016).

[28] W.-T. Hsu, L.-S. Lu, P.-H. Wu, M.-H. Lee, P.-J. Chen, P.-Y. Wu, Y.-C. Chou, H.-T. Jeng, L.-J. Li, M.-W. Chu, W.-H. Chang. Negative circular polarization emissions from $WSe_2/MoSe_2$ commensurate heterobilayers. *Nat. Commun.* **9**, 1356 (2018).

[29] D. Lagarde, L. Bouet, X. Marie, C. R. Zhu, B. L. Liu, T. Amand, P. H. Tan, B. Urbaszek. Carrier and polarization dynamics in monolayer MoS_2. *Phys. Rev. Lett.* **112 (4)**, 047401 (2014).

[30] G. Wang, E. Palleau, T. Amand, S. Tongay, X. Marie, B. Urbaszek. Polarization and time-resolved photoluminescence spectroscopy of excitons in $MoSe_2$ monolayers. *Appl. Phys. Lett.* **106 (11)**, 112101 (2015).

[31] P. Nagler, G. Plechinger, M. V. Ballottin, A. Mitioglu, S. Meier, N. Paradiso, C. Strunk, A. Chernikov, P. C. M. Christianen, C. Schüller, T. Korn. Interlayer exciton dynamics in a dichalcogenide monolayer heterostructure. *2D Mater.* **4 (2)**, 025112 (2017).

[32] B. Miller, A. Steinhoff, B. Pano, J. Klein, F. Jahnke, A. Holleitner, U. Wurstbauer. Long-lived direct and indirect interlayer excitons in van der Waals heterostructures. *Nano Lett.* **17 (9)**, 5229–5237 (2017).

[33] C. Jiang, W. Xu, A. Rasmita, Z. Huang, K. Li, Q. Xiong, W.-bo Gao. Microsecond dark-exciton valley polarization memory in two-dimensional heterostructures. *Nat. Commun.* **9**, 753 (2018).

[34] M. Z. Bellus, F. Ceballos, H.-Y. Chiu, H. Zhao. Tightly bound trions in transition metal dichalcogenide heterostructures. *ACS Nano* **9 (6)**, 6459–6464 (2015).

[35] F. Ceballos, M. Z. Bellus, H.-Y. Chiu, H. Zhao. Probing charge transfer excitons in a $MoSe_2$–WS_2 van der Waals heterostructure. *Nanoscale* **7 (41)**, 17523–17528 (2015).

[36] D. Kozawa, A. Carvalho, I. Verzhbitskiy, F. Giustiniano, Y. Miyauchi, S. Mouri, A. H. Castro Neto, K. Matsuda, G. Eda. Evidence for fast interlayer energy transfer in $MoSe_2/WS_2$ heterostructures. *Nano Lett.* **16 (7)**, 4087–4093 (2016).

[37] M. M. Fogler, L. V. Butov, K. S. Novoselov. High-temperature superfluidity with indirect excitons in van der Waals heterostructures. *Nat. Commun.* **5**, 4555 (2014).

[38] L. V. Butov, C. W. Lai, A. L. Ivanov, A. C. Gossard, D. S. Chemla. Towards Bose–Einstein condensation of excitons in potential traps. *Nature* **417**, 47–52 (2002).

[39] A. A. High, E. E. Novitskaya, L. V. Butov, M. Hanson, A. C. Gossard. Control of exciton fluxes in an excitonic integrated circuit. *Science* **321 (5886)**, 229–231 (2008).

[40] G. Grosso, J. Graves, A. T. Hammack, A. A. High, L. V. Butov, M. Hanson, A. C. Gossard. Excitonic switches operating at around 100 K. *Nat. Photonics* **3**, 577–580 (2009).

[41] C.-H. Lee, G.-H. Lee, A. M. van der Zande, W. Chen, Y. Li, M. Han, X. Cui, G. Arefe, C. Nuckolls, T. F. Heinz, J. Guo, J. Hone, P. Kim. Atomically thin *p–n* junctions with van der Waals heterointerfaces. *Nat. Nanotechnol.* **9**, 676–681 (2014).

[42] M. M. Furchi, A. Pospischil, F. Libisch, J. Burgdörfer, T. Mueller. Photovoltaic effect in an electrically tunable van der Waals heterojunction. *Nano Lett.* **14 (8)**, 4785–4791 (2014).

[43] R. Cheng, D. Li, H. Zhou, C. Wang, A. Yin, S. Jiang, Y. Liu, Y. Chen, Y. Huang, X. Duan. Electroluminescence and photocurrent generation from atomically sharp WSe_2/MoS_2 heterojunction *p–n* diodes. *Nano Lett.* **14 (10)**, 5590–5597 (2014).

[44] B. Scharf, Z. Wang, D. V. Tuan, J. Shan, K. F. Mak, I. Zutic, H. Dery. Probing many-body interactions in monolayer transition-metal dichalcogenides. *Preprint at https://arxiv.org/abs/1606.07101* (2016).

[45] A. Srivastava, M. Sidler, A. V. Allain, D. S. Lembke, A. Kis, A. Imamoğlu. Optically active quantum dots in monolayer WSe_2. *Nat. Nanotechnol.* **10**, 491–496 (2015).

[46] C. Chakraborty, K. M. Goodfellow, A. N. Vamivakas. Localized emission from defects in $MoSe_2$ layers. *Opt. Mater. Express* **6 (6)**, 2081–2087 (2016).

[47] A. Chernikov, A. M. van der Zande, H. M. Hill, A. F. Rigosi, A. Velauthapillai, J. Hone, T. F. Heinz. Electrical tuning of exciton binding energies in monolayer WS_2. *Phys. Rev. Lett.* **115 (12)**, 126802 (2015).

[48] S. Tongay, J. Zhou, C. Ataca, K. Lo, T. S. Matthews, J. Li, J. C. Grossman, J. Wu. Thermally driven crossover from indirect toward direct bandgap in 2D semiconductors: $MoSe_2$ versus MoS_2. *Nano Lett.* **12 (11)**, 5576–5580 (2012).

[49] J. S. Ross, S. Wu, H. Yu, N. J. Ghimire, A. M. Jones, G. Aivazian, J. Yan, D. G. Mandrus, D. Xiao, W. Yao, X. Xu. Electrical control of neutral and charged excitons in a monolayer semiconductor. *Nat. Commun.* **4**, 1474 (2013).

[50] A. A. Mitioglu, P. Plochocka, J. N. Jadczak, W. Escoffier, G. L. J. A. Rikken, L. Kulyuk, D. K. Maude. Optical manipulation of the exciton charge state in single-layer tungsten disulfide. *Phys. Rev. B* **88 (24)**, 245403 (2013).

[51] A. Arora, K. Nogajewski, M. Molas, M. Koperski, M. Potemski. Exciton band structure in layered $MoSe_2$: from a monolayer to the bulk limit. *Nanoscale* **7 (48)**, 20769–20775 (2015).

[52] A. M. Jones, H. Yu, N. J. Ghimire, S. Wu, G. Aivazian, J. S. Ross, B. Zhao, J. Yan, D. G. Mandrus, D. Xiao, W. Yao, X. Xu. Optical generation of excitonic valley coherence in monolayer WSe_2. *Nat. Nanotechnol.* **8**, 634–638 (2013).

[53] B. Zhu, H. Zeng, J. Dai, Z. Gong, X. Cui. Anomalously robust valley polarization and valley coherence in bilayer WS_2. *Proc. Natl. Acad. Sci. U.S.A.* **111 (32)**, 11606–11611 (2014).

[54] G. Plechinger, P. Nagler, J. Kraus, N. Paradiso, C. Strunk, C. Schüller, T. Korn. Identification of excitons, trions and biexcitons in single-layer WS_2. *Phys. Status Solidi Rapid Res. Lett.* **9 (8)**, 457–461 (2015).

[55] J. Shang, X. Shen, C. Cong, N. Peimyoo, B. Cao, M. Eginligil, T. Yu. Observation of excitonic fine structure in a 2D transition-metal dichalcogenide semiconductor. *ACS Nano* **9 (1)**, 647–655 (2015).

[56] K. P. O'Donnell, X. Chen. Temperature dependence of semiconductor band gaps. *Appl. Phys. Lett.* **58 (25)**, 2924 (1991).

[57] Y. P. Varshni. Temperature dependence of the energy gap in semiconductors. *Physica* **34 (1)**, 149–154 (1967).

[58] G. Kioseoglou, A. T. Hanbicki, M. Currie, A. L. Friedman, D. Gunlycke, B. T. Jonker. Valley polarization and intervalley scattering in monolayer MoS_2. *Appl. Phys. Lett.* **101 (22)**, 221907 (2012).

[59] A. T. Hanbicki, H.-J. Chuang, M. R. Rosenberger, C. Stephen Hellberg, S. V. Sivaram, K. M. McCreary, I. I. Mazin, B. T. Jonker. Double indirect interlayer exciton in a $MoSe_2/WSe_2$ van der Waals heterostructure. *ACS Nano* **12 (5)**, 4719–4726 (2018).

[60] T. Korn, S. Heydrich, M. Hirmer, J. Schmutzler, C. Schüller. Low-temperature photocarrier dynamics in monolayer MoS_2. *Appl. Phys. Lett.* **99 (10)**, 102109 (2011).

[61] N. Peimyoo, J. Shang, C. Cong, X. Shen, X. Wu, E. K. L. Yeow, T. Yu. Nonblinking, intense two-dimensional light emitter: monolayer WS_2 triangles. *ACS Nano* **7 (12)**, 10985–10994 (2013).

[62] N. Lundt, A. Maryński, E. Cherotchenko, A. Pant, X. Fan, S. Tongay, G. Sęk, A. V. Kavokin, S. Höfling, C. Schneider. Monolayered $MoSe_2$: a candidate for room temperature polaritonics. *2D Mater.* **4 (1)**, 015006 (2017).

Chapter 6

Conclusions

In this thesis, the optical properties of the transition metal dichalcogenide (TMDC) monolayers, heterostructures (HSs) and alloys are investigated using mainly photoluminescence (PL) spectroscopy. Various excitonic effects are established which confirms that the ultrathin TMDCs and structures based on these materials appear to be promising candidates for optoelectronic devices. We can highlight the following key results for each topic:

1. In chapter 3, different parameters of the PL and reflectance contrast spectra of the mono-, bi- and trilayer $\mathrm{Mo}_x\mathrm{W}_{1-x}\mathrm{S}_2$ are characterized as functions of the molybdenum concentration at room temperature. The values of integrated intensities, linewidths, positions of the fitted spectral peaks for the bi- and trilayer semiconducting TMDC-based alloys are analysed for the first time. The peak positions show parabolic dependences on the concentration of the alloy constituents. The optical band-gap modifications as well as indirect-to-direct band-gap crossover are clearly observed with the number of layers. Better understanding of the electronic band structures of the ultrathin TMDC alloys gives more opportunities in a construction of high-quality devices. Moreover, a composition of the components in the alloys provides a precise control of the band gaps and therefore optical properties.

2. In chapter 4, we outline the study of the temperature- and gate-voltage-dependent parameters of fitted PL spectra in the single-layer $MoSe_2$. Such detailed measurements are first conducted. The main reasons of the detected changes in the linewidths, integrated intensities and positions of the exciton and trion peaks are suggested to be localization and recharging processes. Both exciton-electron scattering (due to the gate-induced carrier concentration) and thermalization destroy the localized states. The proposed models evaluate contributions of the exciton-phonon interactions with temperature growth and exciton-electron interaction with the electron injection into the system to the exciton peak linewidth broadening. All obtained results are compared with the similar previous calculations in the monolayer TMDCs and semiconductor quantum wells. Our estimates may help to find out more about fundamental many-body interactions in the two-dimensional materials.

3. In chapter 5, the low-temperature investigation of the $MoSe_2/WSe_2$ and $MoSe_2/WS_2$ vertical HSs is carried out by means of PL and photoluminescence excitation (PLE) spectroscopies. For the $MoSe_2/WSe_2$ heterobilayers, the influence of the HfO_2/hBN encapsulation on the structure and polarization of the interlayer exciton (IX) spectral peaks is studied for the first time. Power and gate voltage dependences of the PL demonstrate clear evidences of the localized nature of IXs, their long lifetimes and strong repulsive interactions. The peak positions of such excitonic complexes are redshifted with heating because of the phonon involvement. PLE data confirm the formation of indirect excitons via the ultrafast charge transfer. The emission of the $MoSe_2/WS_2$ hybrid bilayers contains a multitude of spectral peaks whose origin is still uncertain. After the analysis of our results from that HS and also owing to the specific band offsets, we claim that the extraordinary PL signal is not formed by pure IXs but concerned with the excitonic states with hybridized electrons between the layers. Making ultrathin artificial materials and hence band gap engineering reveal new prospects for unique optoelectronic applications.